Resolving the inner circumstellar disks of T Tauri and Herbig Ae/Be stars with infrared interferometry

Dissertation
zur
Erlangung des Doktorgrades (Dr. rer. nat.)
der
Mathematisch-Naturwissenschaftlichen Fakultät
der
Rheinischen Friedrich-Wilhelms-Universität Bonn

vorgelegt von
Jasmin Vural
aus
Kiel

Bonn 2014

Angefertigt mit Genehmigung der Mathematisch-Naturwissenschaftlichen
Fakultät der Rheinischen Friedrich-Wilhelms-Universität Bonn

Prof. Dr. Gerd Weigelt, Max-Planck-Institut für Radioastronomie, Bonn
Prof. Dr. Pavel Kroupa, Argelander-Institut für Astronomie, Bonn

Tag der Promotion: 22.12.2014
Erscheinungsjahr: 2015

Resolving the inner circumstellar disks of T Tauri and Herbig Ae/Be stars with infrared interferometry

Jasmin Vural

Abstract

Circumstellar disks around young stellar objects (YSO) are a fundamental element of star and planet formation. The inner disk regions of pre-main sequence stars are hot enough for dust sublimation and a rim between dust-free and dusty disk regions can form. This rim can influence the outer parts of the disk through shielding of stellar radiation and its radius can reveal hints to the structure of the very inner disk.

The nearest star-forming regions, which harbor YSO, are too far away to allow direct imaging of the inner disk regions. Only recently, it became possible to resolve astronomical objects on spatial scales needed for the investigation of the inner disk regions. The technique used for these high-angular resolution observations is infrared interferometry, which combines the light from several telescopes to create interferograms. The facility used in the projects of this thesis is the Very Large Telescope Interferometer with the interferometric instruments AMBER and MIDI, which operate in the near- and mid-infrared (approximately 1.5 μm – 2.4 μm and 8 μm – 13 μm), respectively. With these instruments, it is possible to determine the radius and shape of the disk region emitting in the these wavelength regimes.

The dust typically present in circumstellar disks evaporates at around 1500 K and hence, emits at near- and mid-infrared wavelengths, where it can be observed with AMBER and MIDI. To obtain the characteristic size of the observed emitting region, the interferometric data can be modeled with geometric ring models. The resulting disk radii are typically proportional to the stellar luminosity, but can deviate from this proportionality due to different physical effects determining the disk structure in addition to the stellar radiation. Taking into account as well the spectral energy distribution (SED) of the respective star-disk system, temperature-gradient models give an estimate of the disk properties like the inner radius of the dust disk, the radial temperature distribution, and the inclination of the disk.

The projects presented in this thesis employ the described methods for studies of the inner disk regions of three different pre-main sequence stars: the T Tauri star S CrA N, the Herbig Ae star V1026 Sco, and the Herbig B[e] star HD 85567.

S CrA N has a mass of 1.5 $M_\odot$ and a luminosity of ∼2.3 $L_\odot$. Its near-infrared ring-fit radius is ∼0.11 AU and thus, approximately two times larger than expected. This large radius can be explained by taking into account backwarming by the disk itself, which heats up the dust in addition to the stellar radiation and lets the dust evaporate further outward. The temperature-gradient modeling of SED, AMBER, and MIDI data indicates a two-component structure of the disk, where the inner hot, ring-like component could be the puffed-up inner rim proposed for Herbig Ae/Be stars.

V1026 Sco is a 1.8 $M_\odot$ star with a luminosity of ∼11 $L_\odot$ and is subject to the UX Ori variability. The ring radius derived from the AMBER data is ∼0.18 AU. Temperature-gradient modeling of the SED, AMBER, and MIDI data suggests a disk that consists of two components, which are separated by an approximately 1 AU-wide gap. The inner, thin ring-component might be the puffed-up inner rim that casts a shadow on the disk regions further outward, hence causing the gap between the components. The found disk inclination of ∼50° is consistent with models that assume the UX Ori-variability to arise from inner disk phenomena that obscure the line of sight in between star and observer temporally, for example orbiting dust clouds or centrifugally-driven disk winds.

HD 85567 has a mass of 12 $M_\odot$ and a luminosity of ∼15 000 $L_\odot$. Modeling the AMBER data reveals near-infrared ring-fit radii of 0.8 – 1.6 AU. The found radii are three to five times smaller than predicted by the standard model described above. Assuming that the gas disk interior to the dusty disk absorbs the stellar radiation partially can explain the results and agrees with measurements of stars with similar luminosity.

The near-infrared radii found for the circumstellar disks of the observed stars give a differentiated picture of the inner disk regions of pre-main sequence stars. The assumed proportionality between stellar luminosity and near-infrared radius reproduces the measurements generally only as an approximate value. The radii of T Tauri and high-mass stars are found to deviate significantly due to different effects influencing the dust sublimation, which are still not completely understood. In addition, the disk structures derived with temperature-gradient modeling contributed to understanding the complex inner disk structures of YSO.

Räumliche Auflösung der inneren zirkumstellaren Scheiben von T-Tauri- und Herbig-Ae/Be-Sternen mit Infrarot-Interferometrie

Jasmin Vural

Zusammenfassung

Die junge Sterne umgebenden zirkumstellaren Scheiben sind ein wesentliches Element der Stern- und Planetenentstehung. Bei Vorhauptreihensternen sind die inneren Bereiche dieser aus Staub und Gas bestehenden Scheiben so heiß, dass der Staub sublimiert. Es wird vermutet, dass sich hierdurch eine Kante zwischen dem staubfreien und dem staubhaltigen Bereich der Scheibe ausbildet. Diese Kante kann die äußeren Scheibenregionen beeinflussen, indem sie die vom Stern ausgehende Strahlung abschirmt. Der Kantenradius kann zudem Hinweise auf die Struktur des innersten Scheibenbereichs geben.

Direkte Aufnahmen der inneren Scheibenbereiche sind aufgrund der weiten Entfernung der nächstgelegenen Sternentstehungsregionen, in denen sich junge Sterne befinden, sehr schwierig. Daher wird seit Kurzem die Technik der Infrarot-Interferometrie eingesetzt, um astronomische Objekte auf Skalen auflösen zu können, die für die Untersuchung von den inneren Scheibenregionen benötigt werden. Hierbei wird das Licht von mehreren Teleskopen überlagert um Interferogramme zu erzeugen. In den Projekten dieser Dissertation wird das „Very Large Telescope Interferometer“ mit den interferometrischen Instrumenten AMBER und MIDI verwendet, welche im nahen und mittleren Infrarotbereich arbeiten (ungefähr 1,5 μm – 2,4 μm, bzw. 8 μm – 13 μm). Mit diesen Instrumenten ist es möglich den Radius und die Form der Regionen der Scheibe zu bestimmen, deren Strahlungsmaximum im jeweiligen Wellenlängenbereich liegt.

Der Staub, der typischerweise in zirkumstellaren Scheiben vorhanden ist, sublimiert bei circa 1500 K und strahlt daher vor allem bei Wellenlängen des nahen und mittleren Infrarotbereichs, wo er mit AMBER und MIDI detektiert werden kann. Um die charakteristische Größe der beobachteten Emissionsregion zu erhalten, werden die interferometrischen Daten mit geometrischen Ringmodellen verglichen. Die daraus abgeleiteten Ringradien sind typischerweise proportional zur Leuchtkraft des Sterns, können aber von dieser Proportionalität abweichen, da verschiedene physikalische Effekte zusätzlich zur stellaren Strahlung die Scheibenstruktur beeinflussen. Modelliert man simultan die spektrale Energieverteilung (SED) des jeweiligen Stern-Scheibe-Systems,

kann man mit Temperaturgradientenmodellen weitere Eigenschaften der Scheibe abschätzen, z.B. den inneren Radius der Staubscheibe, die radiale Temperaturverteilung und die relative Neigung der Scheibe.

Die in dieser Dissertation vorgestellten Projekte setzen die beschriebenen Methoden ein um die inneren Scheibenregionen dreier verschiedener Vorhauptreihensterne zu erforschen: des T-Tauri-Sterns S CrA N, des Herbig-Ae-Sterns V1026 Sco und des Herbig-B[e]-Sterns HD 85567.

S CrA N hat eine Masse von 1,5 $M_\odot$ und eine Leuchtkraft von ~2,3 $L_\odot$. Sein Ringradius im Nahinfraroten ist ~0,11 AU und damit circa zwei Mal größer als der erwartete Radius. Dieser große Radius kann erklärt werden, wenn man die Eigenstrahlung der Scheibe mit berücksichtigt, welche den Staub zusätzlich zur stellaren Strahlung erwärmt und den Staub weiter außen sublimieren lässt. Die Temperaturgradientenmodellierung der SED sowie der AMBER- und MIDI-Daten weist auf eine Zwei-Komponenten-Struktur der Scheibe hin. Hierbei könnte die innere heiße, ringartige Komponente die für Herbig-Ae/Be-Sterne vorgeschlagene Staubkante mit vergrößerter Skalenhöhe sein.

V1026 Sco ist ein 1,8 $M_\odot$-Stern mit einer Leuchtkraft von ~11 $L_\odot$ und gehört zur Klasse der UX-Ori-Veränderlichen. Der aus den AMBER-Daten bestimmte Ringradius ist ~0,18 AU und stimmt mit den Vorhersagen der Standardtheorie für Herbig-Ae/Be-Sterne überein. Temperaturgradientenmodellierung der SED sowie der AMBER- und MIDI-Daten legt nahe, dass die Scheibe aus zwei Komponenten besteht, die durch eine etwa 1 AU breite Lücke getrennt sind. Die innere, dünne Ringkomponente könnte eine hohe Staubkante beschreiben, die einen Schatten über die weiter außen liegenden Scheibenregionen wirft und so die Lücke zwischen den zwei Komponenten des Modells erzeugt. Die abgeleitete Scheibenneigung von ~50° ist konsistent mit Theorien, die annehmen, dass die UX-Ori-Veränderlichkeit durch Phänomene der inneren Scheibe verursacht wird. Dabei würde die Sichtlinie zwischen Stern und Beobachter kurzzeitig verdeckt, z.B. von umlaufenden Staubwolken oder von zentrifugal angetriebenen Scheibenwinden.

HD 85567 hat eine Masse von 12 $M_\odot$ und eine Leuchtkraft von ~15 000 $L_\odot$. Die Modellierung der AMBER-Daten ergibt Ringradien im Nahinfraroten von 0,8 – 1,6 AU. Die gefundenen Radien sind drei bis fünf mal kleiner als von den oben beschriebenen Standardmodellen vorhergesagt. Die Annahme, dass das Gas innerhalb der staubhaltigen Scheibe die Strahlung des Sterns teilweise absorbiert, könnte die Ergebnisse erklären und stimmt auch mit Messungen von Sternen ähnlicher Leuchtkraft überein.

Die Nahinfrarotradien, die für die zirkumstellaren Scheiben der beobachteten Sterne gefunden wurden, liefern ein differenziertes Bild der inneren Scheibenregionen von Vorhauptreihensternen. Die angenommene Proportionalität zwischen der Leuchtkraft des Sterns und dem Nahinfrarotradius reproduziert die Messungen im Allgemeinen nur näherungsweise. Der Radius von T-Tauri-Sternen und massereichen Sternen weicht signifikant von der Vorhersage ab, was verschiedenen Effekten zugeschrieben werden kann, welche die Staubsublimation beeinflussen und immer noch nicht vollständig verstanden sind. Zusätzlich lieferten die mit Temperaturgradientenmodellierung abgeleiteten Scheibenstrukturen einen Beitrag zum Verständnis der komplexen inneren Scheibenstruktur von jungen Sternen.

Contents

1 Introduction

1.1 Motivation

The formation of stars and planets plays a key role for the question about how our own solar system and the Earth itself have been created. During the star formation process, the infalling matter is believed to gather in a circumstellar disk before being accreted onto the forming star. In later evolutionary stages, the circumstellar disk becomes the cradle for planet formation. Nevertheless, the detailed processes governing the disk evolution are poorly understood. In addition, the question about the existence of circumstellar disks in all types of young stars cannot be answered consistently. It is however expected that most young stars are surrounded by circumstellar disks in one phase of their evolution.

In this work, I investigate the inner regions of circumstellar disks. These regions have sizes of a few AU* and less, which corresponds to scales of milli-arcseconds (mas) for the distance of nearby star-forming regions. These scales have only recently become observationally available: With near- and mid-infrared interferometry, it is possible to spatially resolve disk regions that give important insights into the inner and outer disk structure. In addition, characterizing the circumstellar dust (e.g., the grain size distribution or dust composition) helps to understand the evolution of circumstellar disks.

The inner disk regions are observationally associated with strong near-infrared emission that is attributed to dust with temperatures around the dust sublimation temperature (~1500 K). Interferometric observations of this emission allow us to deduce the size of the inner rim of the dusty disk. The obtained geometric and physical parameters can then be compared with theoretical predictions for different types of young stars.

In this thesis, the inner disk regions of three young stars of different types are studied. This small sample spans from a low-mass T Tauri star over a slightly higher-mass Herbig Ae star to a massive Herbig B[e] star.

In the following, I will give an introduction about star formation (Sec-

---

*For units and constants see Appendix A

tion 1.2) and circumstellar disks (Section 1.2.2), before explaining the theoretical and applied basics of the observational methods employed (Sections 1.3.1, 1.3.2). Finally, the facilities and instruments used will be described (Section 1.3.3). The main part consists of the publications containing the research on the T Tauri star S CrA N (Chapter 2), the Herbig Ae star V1026 Sco (Chapter 3) and the Herbig B[e] star HD 85567 (Chapter 4). Chapter 5 will give a summary of the thesis and an outlook.

1.2 Young stellar objects

1.2.1 Formation and classification

Figure 1.1: Star-forming region in the Carina Nebula. Young stellar systems can be recognized in the cloud pillars by their jets [Credit: NASA, ESA, M. Livio and the Hubble 20th Anniversary Team (STScI)]

Young stellar objects (YSO) are formed during the gravitational collapse of a molecular cloud (cf. Fig. 1.1). This collapse and thereby the formation of a star takes place in several phases. This is in accordance with the observational classification of the spectral energy distribution (SED) in the near- and mid-infrared (NIR, MIR) as $\nu F_\nu \propto \nu^\alpha$, where ν is the frequency. The spectral index α is used for constructing four classes that reflect the evolutionary sequence of YSO (Lada & Wilking 1984; Lada 1987; Andre et al. 1993; Greene et al. 1994; Andre et al. 2000, see Fig. 1.2):

Class 0 (α cannot be measured): After the molecular cloud collapsed and fragmented due to self-gravitation, the fragments eventually form protostars that perform no fusion yet and which are surrounded by dusty envelopes. The formation of a circumstellar disk is initiated.

Class I ($\alpha > 0.3$): The infalling matter (gas and dust) is gathered in a disk around the protostar, often accompanied by a bipolar outflow.

Class II ($-1.6 < \alpha < -0.3$): The spherical infall of matter eventually stops. A circumstellar disk has formed around the pre-main sequence (PMS) star.

Class III ($\alpha < -1.6$): The circumstellar disk dissipates mainly due to grain growth and settling into a planetary debris disk.

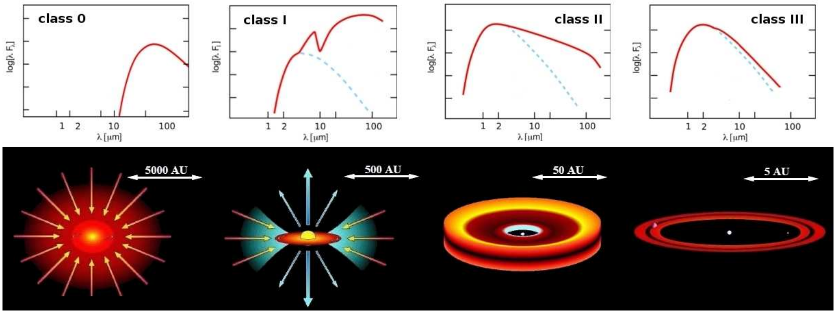

Figure 1.2: YSO classification scheme. The upper row shows the total SED of each class (solid red line) and the stellar spectrum (dashed grey line). The lower row depicts the corresponding assumed YSO morphology. [Adapted from McCaughrean 1997, A. Isella (PhD thesis)]

In addition, stars with a flat spectrum ($-0.3 < \alpha < 0.3$) can be considered as a distinct evolutionary state that describes solely the evolutionary stage when matter from the surrounding envelope falls onto the disk (Calvet et al. 1994). The classification system works well for objects that are observed face-on, but is unreliable for edge-on objects: YSO that are heavily obscured by their disks might be misinterpreted.

During the collapse of the protostellar cloud, a redistribution of angular momentum between protostar and surrounding matter is required due to the conservation law. Excess angular momentum has to be transported outward to make the formation of a protostar possible. This transport is partially provided by the circumstellar disk and outflows. However, stellar multiplicity might play a major role for angular momentum transport, especially for very high-mass star formation, where the presence of circumstellar disks is not generally confirmed (Larson 2010).

As already indicated, PMS stars of different masses evolve in a different way, which also affects the appearance of their circumstellar disks. The stars can be divided into different groups depending on their mass or spectral type. A short overview is given in the following:

T Tauri stars (TTS) are PMS stars with low mass ($<2\ M_\odot$) and with spectral types F and later (the group was introduced by Joy 1945). TTS are commonly surrounded by circumstellar disks. TTS with accretion signatures are called classical T Tauri stars (CTTS), TTS without accretion signatures are named weak-line T Tauri stars (WTTS). TTS without circumstellar disks are called naked or post-T Tauri stars.

Herbig Ae/Be (HAeBe) stars are PMS stars of spectral type A and B (the group is defined by and named after Herbig 1960). Typically, they have several solar masses ($2\ M_\odot$ – $8\ M_\odot$, sometimes the limit is set to $10\ M_\odot$). So called group I objects show strong IR excess, whereas group Ia contains objects with a defined silicate feature around 10 μm and Ib without. Group II objects have a weak infrared (IR) excess (Meeus et al. 2001). They are associated with self-shadowed disk, whereas group I can be described with flared disks (Dullemond & Dominik 2004). UX Ori objects (UXOrs) are supposedly HAeBe stars that are variable at optical wavelengths. This phenomenon has been attributed to a temporal obscuration by circumstellar material in the line of sight. It is proposed that the obscuring effects take place in the inner disk region or close to the dust sublimation zone (Grinin et al. 1994; Natta et al. 1997; Vinković & Jurkić 2007).

High-mass stars are PMS stars with masses higher than $8\ M_\odot$ or $10\ M_\odot$. Their spectral types are B or O. Some high-mass stars were found to have disks, (e.g., Kraus et al. 2010; Grellmann et al. 2011; Preibisch et al. 2011). However, the general formation of circumstellar disks around high-mass stars is still under debate due to their short PMS time and their radiation pressure. High-mass stars have an important influence on disk lifetimes of close-by PMS stars due to their influence on the ambient environment, e.g., by photoevaporation.

1.2.2 Circumstellar disks

A young star gains more than half of its mass during the class-0 and class-I phases (Evans et al. 2009). In the following phases, the surrounding envelope, as source for the spherical infall, has mostly dispersed and the main source for reaching the final mass is the circumstellar accretion disk (Williams & Cieza 2011). In the late stages of class II, the observational accretion luminosity itself becomes a negligible process and the disk is called a passive disk.

The general star formation scheme makes the existence of circumstellar disks in all PMS stars plausible, however, observations of diskless PMS stars were also made. This could be due to at least two effects: First, circumstellar disks have a lifetime of only several millions of years and are dissipated afterwards, dependent on the spectral type, multiplicity, and the environment (cf. Wyatt 2008; Cieza et al. 2009). Second, for very massive stars, the presence of circumstellar disks is not generally confirmed as high-mass star formation might proceed in a different pattern. In general, solar-mass stars can have a disk lifetime up to 10 Myr and more, whereas disks of objects with higher masses have a significantly shorter lifetime (Haisch et al. 2001; Williams & Cieza 2011).

The presence of circumstellar material around PMS stars was initially inferred by the observed IR excess in the SED (cf. Fig. 1.2, SED from class I on). On large-scales, disks itself have been observed directly, for example as dark lanes on a background of scattered light (O'Dell & Wen 1994; Padgett et al. 1999, Fig. 1.3) or by detection of rotating circumstellar material with sub-mm observations (Andrews et al. 2009, Fig. 1.4). The disks can have an extent of several 100 AU (e.g., McCaughrean et al. 1998; Vicente & Alves 2005). However, the inner regions (<10 AU), which are considered to be the site of planet formation, are difficult to resolve and are thus still subject of intensive research.

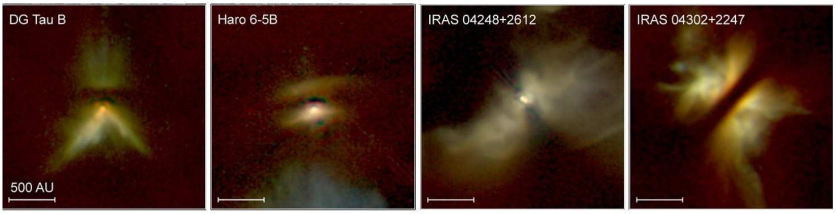

Figure 1.3: Young stellar objects in the infrared. When viewed rather edge-on, circumstellar disks are visible as dark lanes in front of light that is scattered by the disk. [Credits: HST/NICMOS, Padgett et al. 1999 (adapted)]

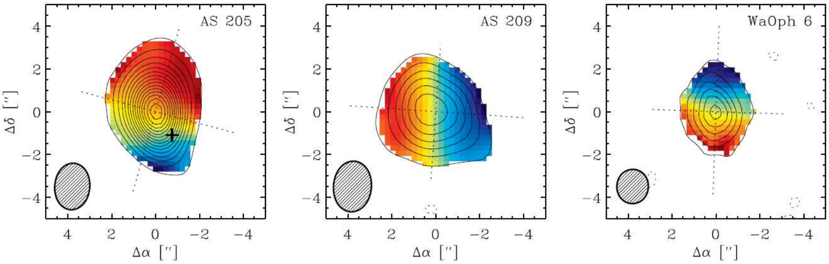

Figure 1.4: CO emission in circumstellar disks. The color gradient shows the intensity-weighted velocity distribution over the disk, which is a signature for rotation of an inclined disk. The contours mark the velocity-integrated intensity. [Credits: Andrews et al. 2009]

1.2.2.1 Disk evolution

Circumstellar disks consist of about 99% gas and only a little amount of dust, however, dust is the main source of opacity and its emission dominates the SED from IR to radio wavelengths. Typical dust species are silicates and polycyclic aromatic hydrocarbons (PAH; Henning & Meeus 2009). The observation of the gas is based mainly on high-resolution spectroscopy of molecular lines.

The gas disk undergoes – in a first approximation – a viscous evolution (e.g., Hartmann et al. 1998; Hueso & Guillot 2005; Armitage 2011). The outer disk is thereby the reservoir for the accretion of matter from the inner disk onto the star. Here, the circumstellar matter is channelled along magnetic field lines before falling onto the star. This paradigm of magnetospheric accretion is proposed for both T Tauri (Bouvier et al. 2007) and Herbig Ae/Be stars (Muzerolle et al. 2004). When the accretion rate drops to around 10^{-10} $M_{\odot}/yr$ or 10^{-9} $M_{\odot}/yr$, the outer disk cannot provide supply anymore and the inner disk disappears on the viscous timescale in $\lesssim 10^5$ yr. A hole of several AU forms in the inner disk regions and photoevaporation of the remaining disk becomes stronger as the extreme ultraviolet emission impinges directly onto the inner edge of the remaining disk (Clarke et al. 2001; Williams & Cieza 2011).

The evolution of the dust disk differs slightly from the evolution of the gas disk because normally only small dust grains are dragged with the gas. However, several small grains can merge to a larger grain compound, which has a smaller surface-to-mass ratio compared to the single grains. As a consequence, the motion of the grain compound is not necessarily determined by the gas anymore and eventually, the larger grains settle in the disk midplane. The larger density towards the disk midplane enables even more grain growth (Williams & Cieza 2011). The dust settling reduces the scaleheight and flaring angle of the disk (Dullemond & Dominik 2004). Although these are time-dependent processes, the evolutionary status of a circumstellar disk cannot be easily derived from the observed grain size distribution. This is due to several reasons: First, the grain growth already starts before the actual circumstellar disk forms. Furthermore, small dust grains are observable throughout all ages, which is due to a balance between grain coagulation and fragmentation (Dullemond & Dominik 2008). In addition, turbulence mixes up small and big grains (Dullemond & Dominik 2005).

1.2.2.2 The inner disk

A circumstellar disk can be described – as a first approximation – by a cylindrically symmetric object that has an radially increasing scale height $h(r) \propto r^k$, where $k \approx 1.3 - 1.5$ (Kenyon & Hartmann 1987; Chiang & Goldreich 1997). The disk surface is irradiated by the star and accounts for most of the IR excess in the SED via scattering, absorption, and reprocessing of the radiation. In addition, the accreting disk midplane can contribute to the IR radiation via viscous heating (Chiang & Goldreich 1997; Lachaume et al. 2003).

The inner disk regions ($\lesssim$ 1 AU) can have temperatures exceeding typical dust sublimation temperatures (e.g., 1500 K for silicates). Thus, the innermost disk part is assumed to be mostly free of dust and can be described as an optically thin gas disk that is surrounded by an optically thick dust and gas disk (Muzerolle et al. 2004; Dullemond & Monnier 2010, Fig. 1.5). In the transition zone between dusty and dust-free disk, the inner rim of the dust disk receives the stellar radiation under larger impact angles than the outer part of the disk. It is assumed that this leads to a comparatively large scale height of the inner rim. In this concept, the inner border of the dusty disk is called puffed-up inner rim (Natta et al. 2001; Dullemond et al. 2001). This description was introduced to explain the 3 μm bump in the SED of Herbig Ae/Be stars and the rather large NIR radii found with interferometric measurements. TTS are also expected to have puffed-up inner rims but the excess emission is harder to detect (Dullemond et al. 2001; Muzerolle et al. 2003).

The puffed-up rim can shield the stellar radiation for the disk parts behind the rim (Meeus et al. 2001; Dullemond & Dominik 2004). The proposed shadow itself does not need to follow strict geometric considerations; radial radiative diffusion and scattering of radiation over the rim edge can blur the shadow (van Boekel et al. 2005a). A temporally variable rim height might possibly explain the NIR variability of UXOrs as the timescale of variability points rather to the inner than the outer disk as source of the phenomenon (Juhász et al. 2007; Sitko et al. 2008).

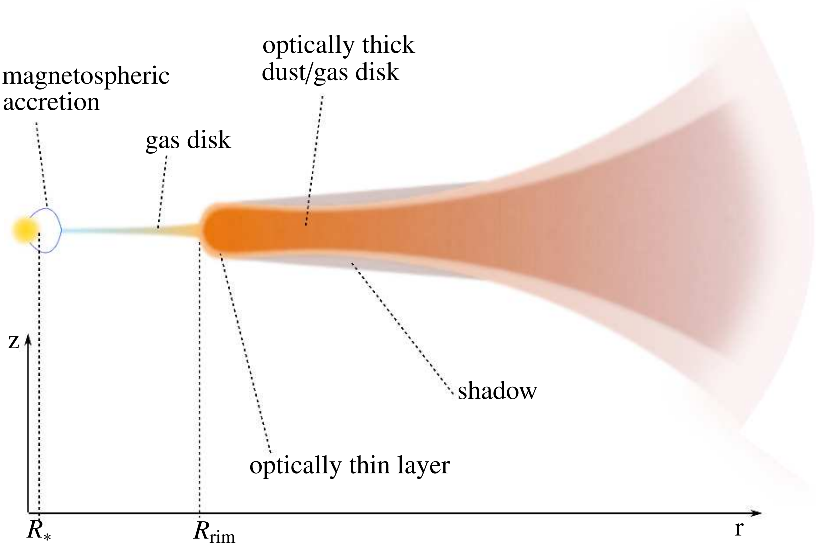

Figure 1.5: Suggested structure of a circumstellar disk. The innermost disk region consists of mostly gas, which is accreted onto the star via magnetospheric accretion. The outer disk contains gas and ∼1% dust. At the radius $R_{\rm rim}$, the dust reaches its sublimation temperature. The formed puffed-up inner rim can cast a shadow on the disk region further outward. In addition to the optically thick dust disk, an optically thin outer layer might exist.

The vertical shape of the rim is assumed to be rounded off by different physical effects like grain composition, grain size distribution, surface density, and vertical density gradients (Isella & Natta 2005; Monnier et al. 2006; Tannirkulam et al. 2007; Kama et al. 2009). In addition, the rim does not require a sharp boundary as has been proposed before, but can be fuzzy due to optically thin dust (Fig. 1.6, Kama et al. 2009; Dullemond & Monnier 2010). In addition, the region inside of the dust-sublimation radius can also contribute to the 3 μm bump. It can contain hot gas (Eisner et al. 2007a; Isella et al. 2008), optically thin dust (Vinković 2006; Kama et al. 2009) or refractory dust (Tannirkulam et al. 2008; Benisty et al. 2010). All these effects can "spread" the detected NIR emission over a range of radii compared to a sharp, vertical rim.

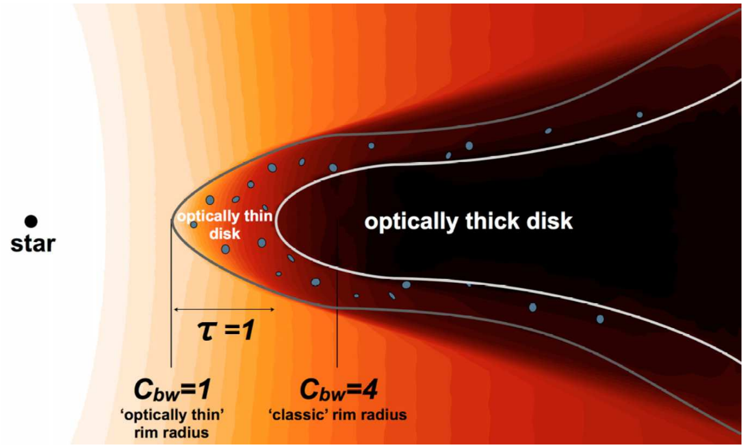

Figure 1.6: Optically thin and thick regions of the dust rim. The radius of the dust rim is controlled by the backwarming factor C_{bw}. [Credit: Kama et al. 2009]

The radius of the inner dust rim can observationally be determined in the NIR, where the assumed dust sublimation temperature of 1500 K has its emission maximum. This NIR radius is correlated with the luminosity of the central star via the so called size-luminosity relation (Monnier & Millan-Gabet 2002). In a first approximation, it is assumed that the radiation of the star (with luminosity L_*) impinges at the dust rim at R_{rim} after travelling without energy losses through only optically thin material (Tuthill et al. 2001), but with absorption by the dust in the rim (gray dust, Monnier & Millan-Gabet 2002; Dullemond & Monnier 2010). Following Dullemond & Monnier (2010), one can assume energy conservation, thus the irradiation of the rim F_{heat} is compensated by the rim emission F_{cool}:

$$
\begin{aligned}
F_{\mathrm{cool}} &= F_{\mathrm{heat}} && (1.1)\\
\Leftrightarrow \sigma T_{\mathrm{rim}}^4 &= \frac{Q}{2}\frac{L_*}{4\pi R_{\mathrm{rim}}^2} && (1.2)\\
\Leftrightarrow R_{\mathrm{rim}} &= \left(\frac{Q}{2}\frac{L_*}{4\pi\sigma T_{\mathrm{rim}}^4}\right)^{1/2}\ , && (1.3)
\end{aligned}
$$

where T_{rim} is the temperature at the radius R_{rim}. The ratio of the dust absorption efficiencies of the incident and emitted field is described by the factor $Q = Q_{\mathrm{abs}}(T_*)/Q_{\mathrm{abs}}(T_{\mathrm{rim}})$. Its value is often assumed to be around 1 but actually depends on the grain size (in addition to the stellar and dust temperatures). By inserting the stellar luminosity $L_* = 4\pi\sigma R_*^2 T_*^4$ into eq. (1.3), we obtain

$$
R_{\mathrm{rim}} = \sqrt{\frac{Q}{2}}\left(\frac{T_*}{T_{\mathrm{rim}}}\right)^2 R_*\ , \tag{1.4}
$$

or by converting into astronomical units:

$$
R_{\mathrm{rim}} \sim 1.1\,\sqrt{Q}\left(\frac{L_*}{1000L_\odot}\right)^{1/2}\left(\frac{T_{\mathrm{rim}}}{1500\mathrm{K}}\right)^{-2}\mathrm{AU}\ . \tag{1.5}
$$

Equation (1.5) shows a size-luminosity relation, which describes well the measurements of the K-band ring-fit radii of the circumstellar disks of Herbig Ae stars (Monnier & Millan-Gabet 2002). Small deviations from this relation can be explained with projection effects, when measuring an inclined disk not along the semi-major axis (Dullemond & Monnier 2010). Figure 1.7 shows the size-luminosity relation for different types of PMS stars and the dependence on the total luminosity including the stellar and the accretion luminosity.

T Tauri stars are often found to have larger R_{rim} than predicted by the size-luminosity relation (Eisner et al. 2007b). This can be explained with additional flux contributions by either accretion (Muzerolle et al. 2003; Akeson et al. 2005a) or backwarming (Millan-Gabet et al. 2007; Dullemond & Monnier 2010). These effects increase the temperature in the disk and let the dust evaporate at larger stellocentric radii. In addition, the measured radius of the NIR emitting region can be larger when the NIR emission is not confined to one thin ring-like region but distributed more widely by scattering by the outer disk regions (Pinte et al. 2008).

The disks of Herbig Be stars have often smaller radii than what can be explained with a dust sublimation rim around an optically thin disk cavity. It is assumed that their inner disks are optically thick and shield the stellar ultraviolet radiation. Thus, the dust can stay further inward before evaporating (Monnier & Millan-Gabet 2002; Eisner et al. 2004).

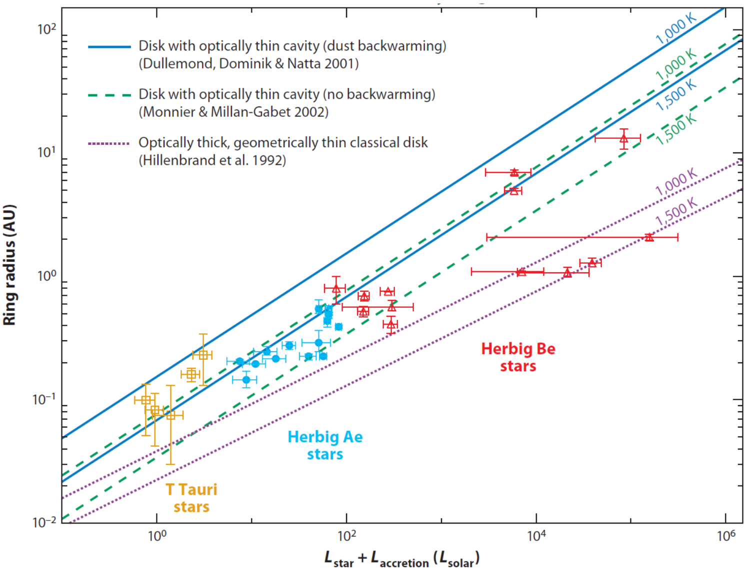

Figure 1.7: Size-luminosity diagram for T Tauri and HAeBe stars. The graph shows the dependence of the K-band ring-fit radius on the total luminosity (stellar and accretion). The models for disks with optically thin cavities are depicted with backwarming (solid blue lines) and without backwarming (dashed green lines). The relation for optically thick inner disks is also shown (dotted purple line). [Credit: Dullemond & Monnier 2010]

This section gave an introduction into the general properties of circumstellar disks of low-, intermediate- and high-mass pre-main sequence stars and especially the inner rim of the dust disk. The next chapter will deal with the observational methods used for resolving circumstellar disks on AU and sub-AU scales.

1.3 Astronomical interferometry

The observational methods used in this work take advantage of the principles of interferometry. In astronomical interferometry, the light of two or more telescopes with a projected distance (baseline) of B is combined to achieve a higher spatial resolution than with a single telescope with a diameter D. Compared to the resolution λ/D (λ is the wavelength of observation) of a single telescope, the resolution of an interferometer is defined by λ/B (e.g., Glindemann 2011). Thus, the available resolution can be much better and smaller structures can be resolved compared to a single telescope.

In the following sections, the basic physical concepts of optical interferometry will be rehearsed and an overview over the used astronomical interferometric facilities will be given.

1.3.1 The theoretical basics of interferometry

When observing a light source (e.g., a stellar system), we are interested in determining its intensity distribution I_0. For observations, we use certain optical systems (e.g., apertures, lenses) and combinations of those. The electromagnetic waves passing through these optical systems undergo changes, e.g., due to diffraction or attenuation, and therefore, the intensity I measured in the image plane is in general different to I_0.

The interferometric observables are the visibility (fringe contrast) and the fringe phase. The fringe phase is described by the location of the central fringe. The visibility V is defined as

$$V = \frac{I_{\mathrm{max}} - I_{\mathrm{min}}}{I_{\mathrm{max}} + I_{\mathrm{min}}} , \tag{1.6}$$

where I_{max} and I_{min} are the maximum and minimum intensity in the image plane, respectively. The visibility is a direct measure for the coherence of the light, as will be shown in the following.

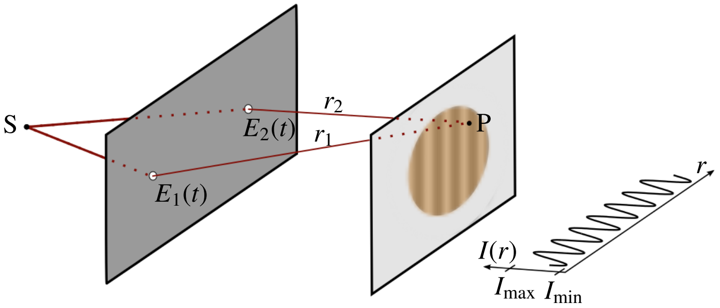

Figure 1.8: Illustration of the interference of two light beams (after Hecht & Zajac 1974).

1.3.1.1 Monochromatic point sources

An approximately monochromatic point source S is considered (after Born & Wolf 1999; Goodman 2000). Two beams with the stationary complex fields $E_1(t) = E(r_1, t)$ and $E_2(t) = E(r_2, t)$ are created via a screen with two pinholes. The fields interfere at a point P (cf. Fig. 1.8), where the total field strength $E(t)$ can be described by the superposition of the fields of both beams:

$$E(t) = K_1 E_1(t+\tau) + K_2 E_2(t) \;, \tag{1.7}$$

where K_1 and K_2 are imaginary coefficients that describe the phase shift and attenuation in the light path and τ is the relative time shift between the arrival of the beams in P. The observed intensity I is defined by

$$\begin{aligned} I &= \langle E(t)E^*(t)\rangle && (1.8)\\ &= |K_1|^2\langle E_1(t+\tau)\rangle^2 + |K_2|^2\langle E_2(t)\rangle^2 + \\ &\quad K_1K_2^*\langle E_1(t+\tau)E_2^*(t)\rangle + K_1^*K_2\langle E_1^*(t+\tau)E_2(t)\rangle \;, && (1.9)\end{aligned}$$

where the brackets indicate the temporal average. The intensity of each beam is $I_1 = |K_1|^2\langle E_1(t+\tau)\rangle^2$ and $I_2 = |K_2|^2\langle E_2(t)\rangle^2$, respectively. The total intensity can hence be simplified to

$$I = I_1 + I_2 + 2\,\mathrm{Re}\left(K_1K_2^*\langle E_1(t+\tau)E_2^*(t)\rangle\right) \;, \tag{1.10}$$

where the product $K_1 K_2^* = |K_1||K_2|$, due to the imaginary nature of the factors. By introducing the mutual coherence function

$$\Gamma_{12}(\tau) = \langle E_1(t+\tau) E_2^*(t) \rangle \tag{1.11}$$

and the self coherence functions

$$\Gamma_{11}(\tau) = \langle E_1(t+\tau) E_1^*(t) \rangle \tag{1.12}$$

$$\Gamma_{22}(\tau) = \langle E_2(t+\tau) E_2^*(t) \rangle \,, \tag{1.13}$$

the complex degree of coherence can be defined by

$$\gamma_{12}(\tau) = \frac{\Gamma_{12}(\tau)}{\sqrt{\Gamma_{11}(0)\Gamma_{22}(0)}} \,. \tag{1.14}$$

The general interfence law for partially coherent light is then obtained:

$$I = I_1 + I_2 + 2\sqrt{I_1 I_2}\, \mathrm{Re}(\gamma_{12}(\tau)) \,. \tag{1.15}$$

When the degree of coherence is expressed in its complex form as

$$\gamma_{12}(\tau) = |\gamma_{12}(\tau)| e^{i\varphi_{12}(\tau)} \,, \tag{1.16}$$

where $\varphi_{12} = \arg(\gamma_{12}(\tau))$, eq. (1.15) becomes

$$I = I_1 + I_2 + 2\sqrt{I_1 I_2}\, |\gamma_{12}(\tau)| \cos(\varphi_{12}(\tau)) \,. \tag{1.17}$$

The phase $\varphi_{12}(\tau)$ can be expressed by the optical path difference $\Delta r = r_2 - r_1$ of the two beams as

$$\varphi_{12}(\tau) = \alpha_{12}(\tau) - 2\pi/\bar{\lambda}\Delta r \,, \tag{1.18}$$

with $\alpha_{12}(\tau)$ being the phase difference:

$$\alpha_{12}(\tau) = \varphi_{12}(\tau) + 2\pi/\bar{\lambda}\Delta r = \varphi_{12}(\tau) + 2\pi\bar{\nu}\tau \,. \tag{1.19}$$

Here, $\bar{\lambda}$ and $\bar{\nu}$ are the mean wavelength and the mean frequency, respectively. When $\gamma_{12} = 1$, the interference pattern has the maximum contrast. The same is true, when the light is strictly monochromatic and $\alpha_{12}(\tau) = 2\pi\bar{\nu}\tau$. The light is then perfectly coherent. When $\gamma_{12} = 0$, there is no fringe contrast – the light beams are incoherent. In between these two values, the light is called partially coherent.

For deriving a relation between the degree of coherence and the visibility, the maximum and minimum intensity

$$I_{\max} = I_1 + I_2 + 2\sqrt{I_1 I_2}\,|\gamma_{12}(\tau)| \tag{1.20}$$

$$I_{\min} = I_1 + I_2 - 2\sqrt{I_1 I_2}\,|\gamma_{12}(\tau)| \tag{1.21}$$

are inserted into eq. (1.6). The visibility is then

$$V = \frac{2\sqrt{I_1}\sqrt{I_2}}{I_1 + I_2}|\gamma_{12}(\tau)| \ . \tag{1.22}$$

and for equal intensities $I_1 = I_2$:

$$V = |\gamma_{12}(\tau)| \ . \tag{1.23}$$

That shows that the visibility is a direct measure for the coherence of the light.

1.3.1.2 Quasi-monochromatic point sources and extended sources

Compared to interference with monochromatic light, quasi-monochromatic light is defined thus that the spectral range $\Delta\nu$ has to be small compared to the mean frequency $\bar{\nu}$ and the time delay is $\tau \ll 1/\Delta\nu$. The relation eq. (1.17) found before is then valid for $\tau \sim 0$ under the assumption that the optical path difference is much smaller than the coherence length:

$$|\Delta r| \ll \frac{c}{\Delta\nu} = \frac{\bar{\lambda}^2}{\Delta\lambda} \ . \tag{1.24}$$

In practice, the coherence will also be determined by the angular extent and shape of the light source. This dependence is described by the Van Cittert-Zernicke theorem (van Cittert 1934; Zernike 1938): It relates the complex degree of coherence γ to the intensity distribution $I_0(\alpha,\beta)$ (with the angular coordinates (α,β)) of an extended source via a Fourier transform and allows to deduce this intensity distribution from the measured interferograms.

$$I_0(\alpha,\beta) = \int\int v(u,v)e^{2\pi i(\alpha u+\beta v)}dudv \ , \tag{1.25}$$

where $v(u, v)$ is the complex visibility and $u = x/\lambda$ and $v = y/\lambda$ are the coordinates the aperture plane (Fig. 1.9), also called uv plane. The visibility (eq. (1.6)) is obtained after normalization and taking the absolute value of the reverse Fourier transform:

$$V(u, v) = \left|\frac{v(u, v)}{v(0, 0)}\right| = \left|\frac{\int\int I_0(\alpha, \beta) e^{-2\pi i(\alpha u+\beta v)} d\alpha d\beta}{\int\int I_0(\alpha, \beta) d\alpha d\beta}\right| . \tag{1.26}$$

The van Cittert-Zernicke theorem is valid under the assumption that the extent of the observed source is much smaller than the distance to the observer. With the help of this theorem, it is possible to derive the visibility for different source shapes and compare the model visibility with the observation (see Sect. 1.3.2.4).

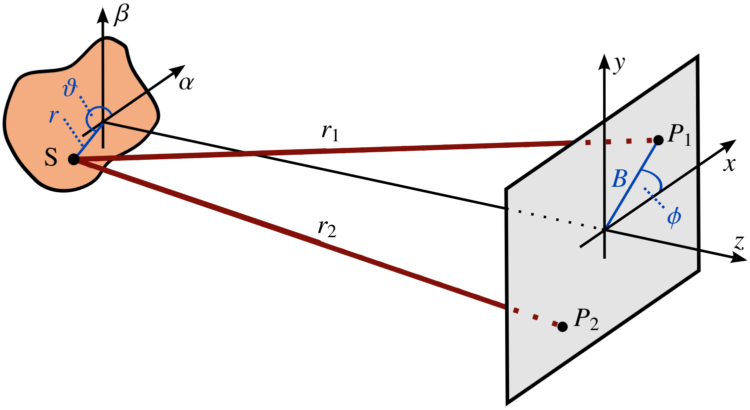

Figure 1.9: Coordinate systems for the van-Cittert-Zernike theorem. Polar coordinates are indicated in blue.

1.3.2 Interferometric observations

The theoretical background considered until here shows the feasibility of interferometric observations. Nevertheless, perfect conditions like in theory cannot be assumed when observing. In the following, the main issues one has to deal with in applied interferometry will be presented.

1.3.2.1 Atmospheric effects

Ground-based observations suffer in general from biases caused by the atmosphere. Wavefronts traveling through the atmosphere can be partially absorbed or distorted. In addition, the atmosphere itself is emitting, mainly in the infrared. This section follows partially Glindemann (2011).

The atmospheric absorption (by e.g., water, ozone, CO_2) only allows observation in certain wavelength ranges, where the transmittance is high. In the near-infrared, these ranges are the J, H, and K band; in the mid-infrared, the L, M, N, and Q band are available for observation (Fig. 1.10). To achieve the highest transmittance possible, telescopes used for observations in the near- and mid-infrared are placed on dry locations at high altitudes.

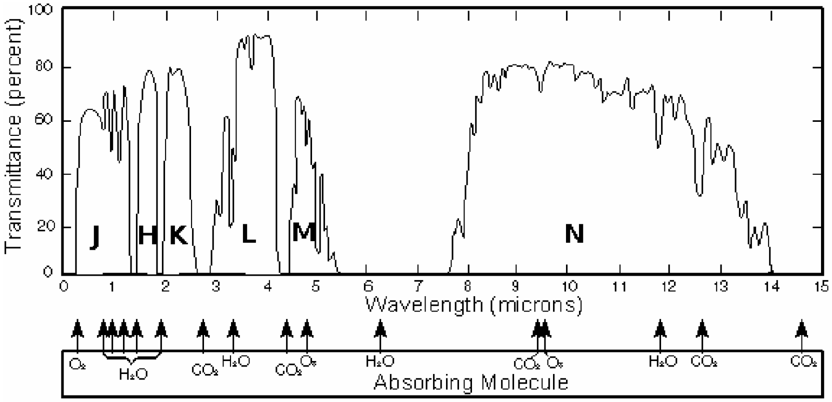

Figure 1.10: Wavelength-dependent atmospheric transmittance in the infrared. The different wavelength bands are marked (J to N band). The molecules responsible for the absorption features are indicated below. [Credit: US Navy – licensed under Public Domain via Wikimedia Commons, adapted]

In the atmosphere, temperature or pressure inhomogeneities lead to a temporally and spatially variable refractive index of the air and turbulent convection cells are created. Those cells cause interference between the wavefronts and lead to a speckle pattern in the telescope image.

Part of the atmospheric wavefront distortions can be compensated by using adaptive optics, which measure the distortions of the incoming wavefront and adapt a deformable mirror to compensate these wavefront deformations. A difficult issue that has to be handled in interferometers is the optical path difference (OPD) between light beams from different telescopes caused by not only atmospheric effects, but also by the orientation of the projected baseline of the telescopes. In order to obtain fringes with a high contrast, the OPD Δs has to be smaller than the coherence length $\lambda^2/\Delta\lambda$. Due to the rotation of the Earth, the OPD between the beams of the different telescopes of an interferometer changes permantly. This effect is compensated via optical delay lines, which keep the OPD approximately at zero. It is also possible to correct for the remaing atmospheric shifts of the OPD using fringe-trackers, which permit to increase the exposure time.

Uncorrected atmospheric OPD shifts can influence the visibility. A compensation during the data reduction might be necessary (cf. Sect. 1.3.3.1). Figure 1.11 depicts the sources of OPD shifts and the correction devices used in the VLTI.

1.3.2.2 The closure phase

The interferograms that are recorded during the observation contain information on the visibility amplitude and the phase of the object, but the object phases are disturbed by the turbulent atmosphere. To extract the undisturbed object phase information, one can apply the Phase Closure Method reported by Jennison (1958). Using three telescopes, the atmospheric phase shift ϕ_n $(n = 1, 2, 3)$ of each beam biases the object phase φ_{kl} $(k, l = 1, 2, 3)$ in the interferogram. The degree of coherence (cf. eq. (1.16)) of two beams with the atmospheric phase shifts ϕ_k and ϕ_l is then:

$$\gamma_{kl}^{\mathrm{at}} = |\gamma_{kl}| e^{i(\varphi_{kl}+\phi_k-\phi_l)} \ . \tag{1.27}$$

As indicated, it is not possible to measure the object phase φ_{kl}, but we can obtain another observable: the closure phase. It can be derived by multiplication of the degree of coherence of each of the three telescopes, the so called

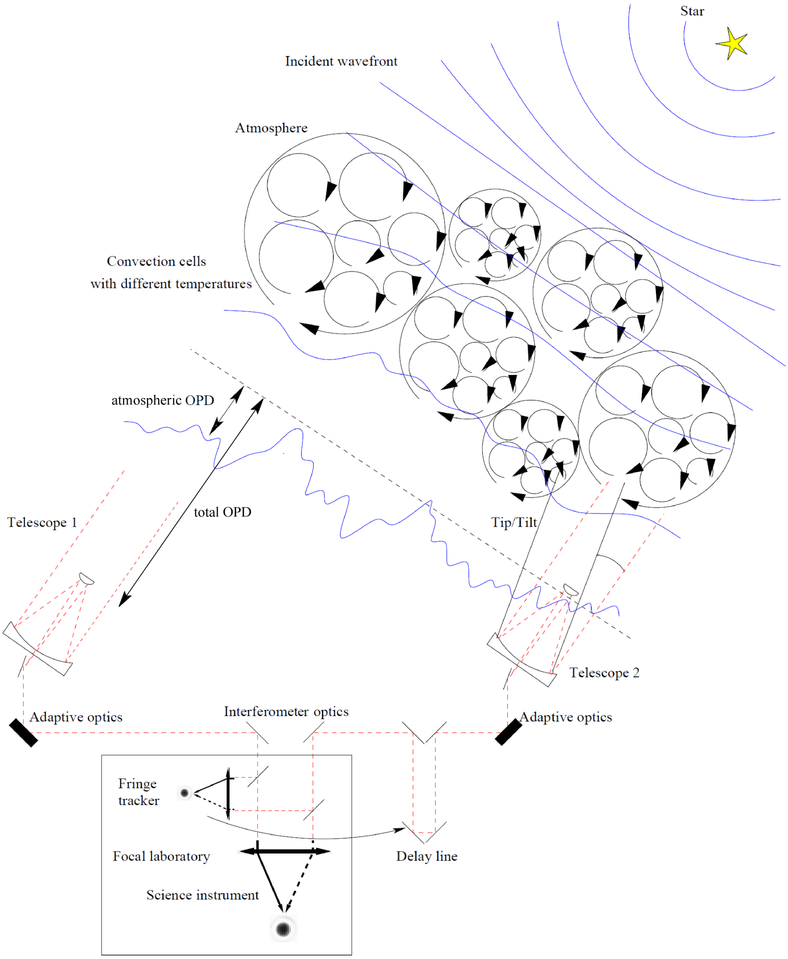

Figure 1.11: Schematic overview of sources of optical path differences and correction devices. Small-scale temperature fluctuations in the atmosphere cause a distortion of the incident wavefront. A fringe tracker can be used to overcome the atmospheric OPD and stabilize the fringes in the interferograms. The OPD between the telescopes is compensated by a delay line. [Credit: Millour 2008, adapted]

bispectrum

$$\gamma_{12}^{\mathrm{at}}\gamma_{23}^{\mathrm{at}}\gamma_{31}^{\mathrm{at}} = |\gamma_{12}||\gamma_{23}||\gamma_{31}|e^{i\Phi_{\mathrm{c}}} \ . \tag{1.28}$$

The closure phase Φ_{c} is then

$$\begin{aligned} \Phi_{\mathrm{c}} &= (\varphi_{12} + \phi_1 - \phi_2) + (\varphi_{23} + \phi_2 - \phi_3) + (\varphi_{31} + \phi_1 - \phi_3) \\ &= \varphi_{12} + \varphi_{23} + \varphi_{31} \ . \end{aligned} \tag{1.29}$$

The closure phase does not depend on the atmospheric error terms ϕ_1, ϕ_2, and ϕ_3 and can be used to reconstruct an image of the observed object – assuming appropriate telescope array configurations were chosen for observations.

1.3.2.3 Filling the *uv* plane

With the currently existing optical interferometers, it is often not easy to get a sampling in the *uv* plane (cf. eq. (1.26), Fig. 1.9) that is sufficient for image reconstruction. Often, one can only take few measurements at certain *uv* points (each defined by the projected baseline length B and the position angle ϕ; cf. Fig. 1.9) and thus obtain only a limited number of Fourier components of the object intensity distribution. The more telescopes (n_{t}) are involved in a single observation, the more baselines (n_{b}) are obtained, following $n_{\mathrm{b}} = n_{\mathrm{t}}(n_{\mathrm{t}} - 1)/2$. For each baseline, one visibility amplitude is obtained. For measuring the closure phase, at least three telescopes are needed, resulting in $n_{\mathrm{c}} = (n_{\mathrm{t}} - 1)(n_{\mathrm{t}} - 2)/2$ closure phases (Monnier 2003). In addition, it is possible to increase the sampling in the *uv* plane by making use of the rotation of the Earth – the so-called super synthesis (Fig. 1.12). Spectrally dispersed data can also help to improve the *uv* sampling, assuming the observed intensity distribution is approximately wavelength-independent.

1.3.2.4 Visibility models

A goal of interferometric observations is to fill the *uv* plane for one object as much as possible to reduce degeneracies when modeling the data of the object. If the *uv* plane can only be unsufficiently filled, it is necessary to optimize the *uv* point distribution of the observation beforehand and to make a first guess about the brightness distribution of the object for modeling. With the van Cittert-Zernicke theorem (eq. (1.26)), the expected visibilities can then be derived and fitted to the data. In the following, the commonly used basic brightness

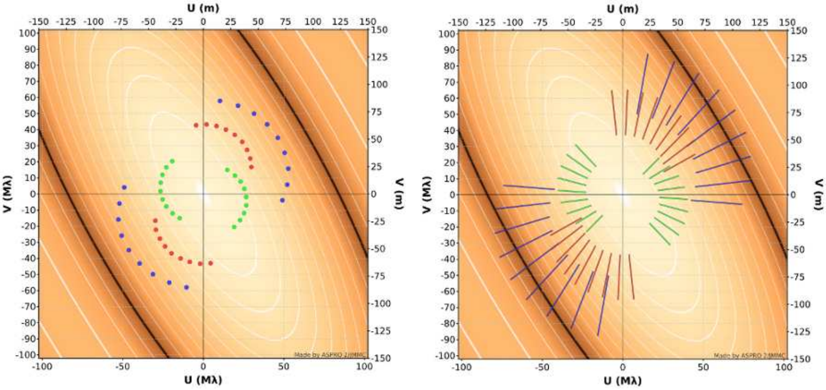

Figure 1.12: *Left:* The *uv* coverage of a night of measurements (here: nine measurements) with the VLTI configuration UT1-UT3-UT4. The nearly circular shape of the *uv*-point track of each baseline (blue, green, and red) results from the rotation of the Earth and the low declination ($\sim\!-60^\circ$) of the observed object. The visibility amplitude distribution of an elongated ring is underplotted. *Right:* The same as the left figure, but with spectrally dispersed measurements, which cover a larger part of the *uv* plane. [Credit: This figure was created with help of the Jean-Marie Mariotti Center `Aspro2` service [†].]

distributions and the associated visibilities, which are used for fitting the data, will be presented (following Berger & Segransan 2007).

The most simple geometric model is a **point source**, which can be used as a model for an unresolved star at the position (α_0, β_0):

$$\begin{aligned} I_0(\alpha,\beta) &= \delta(\alpha-\alpha_0,\beta-\beta_0) \quad (1.30) \\ \Rightarrow V(u,v) &= 1\,. \quad (1.31) \end{aligned}$$

A **uniform disk** with the diameter D might be a suited model, for example, for a resolved stellar surface:

[†] Available at `http://www.jmmc.fr/aspro` .

$$
\begin{aligned}
I_0(\alpha,\beta) &= \begin{cases} 4/\pi D^2 & \text{for } r \leq D/2 \\ 0 & \text{for } r > D/2 \end{cases} && (1.32)\\
\Rightarrow V(u,v) &= 2\frac{J_1(\pi DB)}{\pi DB}\ , && (1.33)
\end{aligned}
$$

where $B = \sqrt{u^2 + v^2}$ (Fig. 1.9) and J_1 is the Bessel function of first order.

For describing disks or halos, a **Gaussian** intensity distribution with a FWHM (full width at half maximum) of D can be used:

$$
\begin{aligned}
I_0(\alpha,\beta) &= \left(\frac{\pi D^2}{4\ln 2}\right)^{-1/2} e^{-4\ln 2 r^2/D^2} && (1.34)\\
\Rightarrow V(u,v) &= e^{-(\pi DB)^2/(4\ln 2)}\ , && (1.35)
\end{aligned}
$$

where $r^2 = \alpha^2 + \beta^2$.

A **thin ring** at the radius R is often used for modeling emission from a very confined disk region:

$$
\begin{aligned}
I_0(\alpha,\beta) &= \frac{\delta(r-R)}{2\pi R} && (1.36)\\
\Rightarrow V(u,v) &= J_0(2\pi RB)\ , && (1.37)
\end{aligned}
$$

where J_0 is the Bessel function of zeroth-order.

For more complex objects, several of those model distributions can be combined by adding up the single intensities I_j at each location (α_j,β_j):

$$
I_0(\alpha,\beta) = \sum_{j=1}^{n} I_j(\alpha,\beta)\,\delta(\alpha-\alpha_j,\beta-\beta_j)\ . \qquad (1.38)
$$

As the Fourier transform of a sum is the sum of the Fourier transforms of the summation elements, the normalized visibility after eq. (1.26) becomes

$$
V(u,v) = \frac{\sum_{j=1}^{n} F_j V_j(u,v) e^{2\pi i(u\alpha_j+v\beta_j)}}{\sum_{j=1}^{n} F_j}\ , \qquad (1.39)
$$

where F_j is the contribution of each component to the total brightness.

A circumstellar disk can be considered as a sum of many concentric thin rings with different temperatures and eq. (1.39) can be used for modeling the visibility and the SED of disks in a more sophisticated way. In a **temperature-gradient** model, each of those rings at a radius r is assumed to have a temperature determined by a power-law distribution:

$$T(r) = T_0 \left(\frac{r}{r_0} \right)^{-q} \ , \tag{1.40}$$

with T_0 being the temperature at r_0 and q the power-law index, which depends on the type of the disk (flat or flared). Each ring is assumed to emit a blackbody spectrum

$$S_{\mathrm{B}}(\lambda, T) = \frac{2hc^2}{\lambda^5} (e^{hc/\lambda k_{\mathrm{B}} T} - 1)^{-1} \ , \tag{1.41}$$

with the temperature $T = T(r)$ after eq. (1.40). The total flux $F(\lambda, i)$ of an optically thick disk spanning between r_{in} and r_{out} can then be derived by integrating the contributions of all rings:

$$F(\lambda, i) = \frac{2\pi}{d} \cos i \int_{r_{\mathrm{in}}}^{r_{\mathrm{out}}} r S_{\mathrm{B}}(\lambda, T(r)) dr \ , \tag{1.42}$$

where d is the distance to the object and i denotes the inclination angle.

The visibility of a circular symmetric object can be derived from eq. (1.26). By switching to polar coordinates (cf. Figs. 1.9, 1.13), the unnormalized visibility becomes:

$$v(B, \phi) = \int_0^{\infty} \int_0^{2\pi} I(r, \vartheta) e^{-2\pi i r B \cos(\vartheta - \phi)} d\vartheta dr \tag{1.43}$$

$$\Rightarrow v(B) = \int_0^{\infty} \int_0^{2\pi} I(r) e^{-2\pi i r B \cos(\vartheta)} d\vartheta dr \ , \tag{1.44}$$

because $I(r, \vartheta) = I(r)$ and $V(B, \phi) = V(B)$ in a circular symmetric object. The solution of the inner integral is the Bessel function of zeroth order:

$$v(B) = 2\pi \int_0^{\infty} I(r) J_0(2\pi r B) r dr \ . \tag{1.45}$$

The baseline B is the projected baseline $B = B_{\mathrm{proj}}$ with

$$B_{\mathrm{proj}} = \sqrt{B_{u,\vartheta}^2 + B_{v,\vartheta}^2 \cos^2 i} \ , \tag{1.46}$$

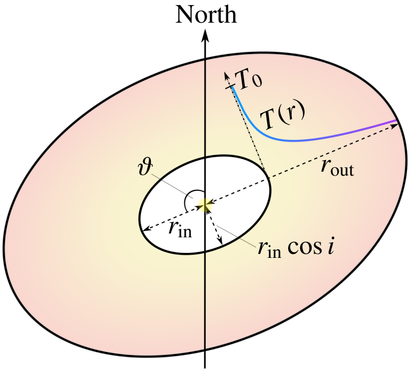

Figure 1.13: Coordinates of the temperature-gradient disk. The position angle ϑ of the semi-major axis is measured East of North. The temperature distribution $T(r)$ after eq. (1.40) is overplotted.

where the rotation by the position angle of the disk semi-major axis ϑ is taken into account by

$$B_{u,\vartheta} = B_u \sin\vartheta + B_v \cos\vartheta\ , \tag{1.47}$$

$$B_{v,\vartheta} = B_u \cos\vartheta - B_v \sin\vartheta \tag{1.48}$$

and the baseline B is projected according to its orientation ϕ (position angle of the measurement) with

$$B_u = B\sin\phi\ , \tag{1.49}$$

$$B_v = B\cos\phi\ . \tag{1.50}$$

With $I(r) = S_{\rm B}(\lambda, T(r))$ and $v(0,0) = d\,F(\lambda,0)$, the normalized visibility of a temperature-gradient disk extending from $r_{\rm in}$ to $r_{\rm out}$ results with eq. (1.26) and eq. (1.45) to

$$V(\lambda, i, \vartheta) = \frac{1}{F(\lambda,0)} \int_{r_{\rm in}}^{r_{\rm out}} S_{\rm B}(\lambda, T(r))\, J_0(2\pi r B_{\rm proj}) \frac{r}{d} dr\ . \tag{1.51}$$

The integrals of eq. (1.42) and eq. (1.51) can be solved numerically. It is possible to compute a large number of models, which are then compared to the measured visibility and SED by calculating the goodness of fit χ_{red} (Pearson 1900). With this method, the basic properties of a centrosymmetric optically thick disk can be determined.

1.3.2.5 Beam combination

The two main approaches for creating interferences in practice are the combination of the light beams in the image plane, after H. Fizeau, and the combination in the pupil plane, after A. Michelson. The following short description is based on Malbet et al. (1999) and Kraus (2007).

A Fizeau interferometer is based on the double slit experiment and combines the light beams in a multi-axial setting (Fig. 1.14, right). The different incoming beams have a geometrically induced OPD and are combined in the image plane. The spatial fringe pattern can hence be recorded with a detector in one exposure. This type of interferometer measures the spatial coherence if the spectral bandwidth of the observation is small.

In a Michelson interferometer, the incoming beams are aligned by being sent through a beam-splitter (Fig. 1.14, left). They are combined co-axially in the pupil plane. Several exposures have to be taken to record the temporal fringe pattern, which is created by modulating the OPD between the beams.

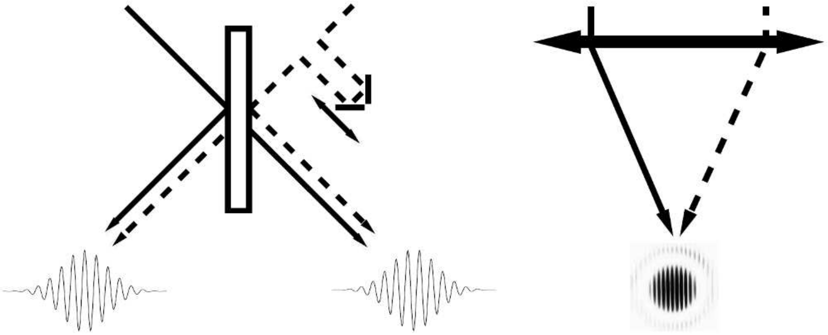

Figure 1.14: Scheme of co-axial (left) and multi-axial (right) beam combination. In the co-axial setting, the incoming beams (entering from top) pass through a beam-splitter and produce two temporal fringe patterns. The multi-axially combined beams enter typically through a double-aperture and produce a spatial fringe pattern. [Credit: Millour (2008)]

1.3.3 The Very Large Telescope Interferometer

The Very Large Telescope Interferometer (VLTI) is located at the Cerro Paranal site in Chile and hosted by the European Southern Observatory (ESO). It provides the possibility to perform interferometric observations in the near- and mid-infrared. Until recently, two interferometric instruments were available to the scientific public: MIDI, a two-beam combiner in the MIR, and AMBER, a three-beam combiner in the NIR. Both combiners can either be used with the Unit Telescopes (UTs) or with the Auxiliary Telescopes (ATs) (Figs. 1.15, 1.16). The four UTs have a diameter of 8.2 m and can provide baselines of 47 m to 130 m. The four ATs span 1.8 m in diameter and can provide baselines between 8 m and 200 m. The achieved spatial resolution λ/B is in the order of few to few tens of milli-arcseconds (e.g., $\lambda/B = 4.1$ mas with $\lambda = 2\ \mu$m and $B = 100$ m and $\lambda/B = 41$ mas with $\lambda = 10\ \mu$m and $B = 50$ m).

Figure 1.15: Photo of the Paranal platform with the four UTs and two of the ATs. The interferometric instruments are located in the VLTI laboratory in the building in the image center [Credit: ESO].

In infrared interferometry, the OPD compensation has to be very accurate. The VLTI delay lines (cf. Fig. 1.16, 1.17) have an accuracy of about 50 nm over a distance of 120 m to ensure this.

The content of this section is based on Leinert et al. (2003) (MIDI), Petrov et al. (2007) (AMBER) and the content of the ESO website[‡], herefrom especially the AMBER Instrument Description, the AMBER User Manual, the AMBER Data Reduction Software User Manual, the MIDI User Manual, and the MIDI data reduction cookbook.

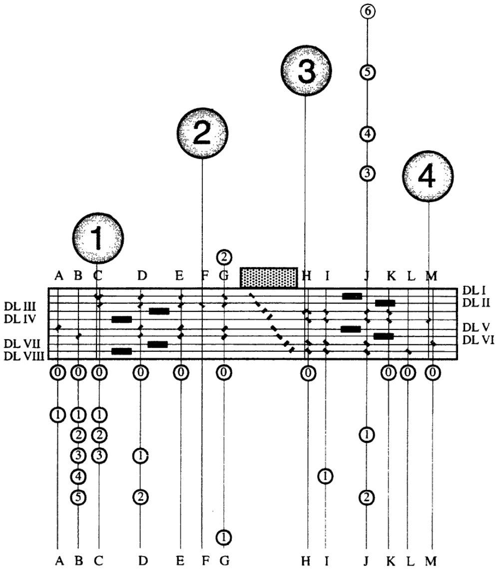

Figure 1.16: VLTI layout. All UT and AT stations are labelled. The delay lines (DL I – DL VI) lead the light beams into the VLTI laboratory (small grey box in image center). [Credit: Glindemann et al. 2004]

[‡] `http://www.eso.org/sci/facilities/paranal/telescopes/vlti.html`

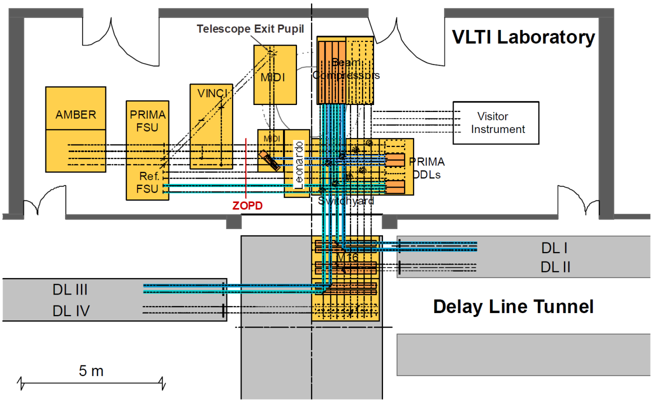

Figure 1.17: VLTI laboratory. The delay lines feed the light beams into the the according interferometric instrument in the VLTI laboratory. [Credit: Koehler (2001)]

1.3.3.1 AMBER

The Astronomical Multi-BEam Recombiner (AMBER) can combine three beams in the J, H, and K band (1.46 μm – 2.4 μm; see also Fig. 1.10) and provides a spectral resolution of approximately 35 (with a prism), 1500, or 12000 (both with a grating). The field of view of AMBER is 60 mas for the UTs and 250 mas for the ATs. The instrument delivers mainly four observables: absolute visibility $V(B, \lambda)$, wavelength-differential visibility $V(B, \lambda)/V(B, \lambda_0)$ (with λ_0 the wavelength in the stellar continuum), wavelength-differential phase $\Phi(B, \lambda) - \Phi(B, \lambda_0)$, and closure phase $\Phi_C(\lambda)$ (cf. Sects. 1.3.1, 1.3.2.2). The spectrum of the source is also measured but requires independent calibration with another instrument because only the inner parts of the light beams enter AMBER.

Observations are limited by rather high sensitivity constraints, depending on the telescopes and instruments used, the spectral resolution, and the weather conditions. Current offical limits demand a minimum correlated magnitude in the K band of 9 mag. Fainter objects have however been observed (Petrov et al. 2012).

The instrumental setup A scheme of the AMBER instrument is shown in Fig. 1.18. The beams of the three telescopes are spatially filtered through single mode optical fibers. The beams are collimated multi-axially and merged in a multi-axial beam combiner into an Airy disk, which is sampled in a one-pixel column in the direction of the baseline. A long-slit spectrograph disperses the fringes. The different spectral bands are separated before the spatial filtering and later merged again by dichroics.

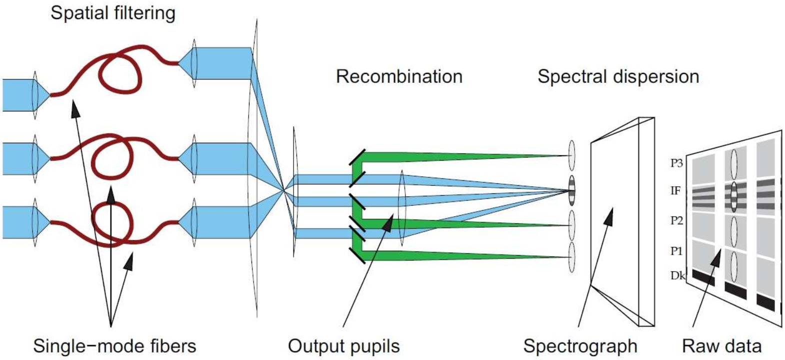

Figure 1.18: Scheme of the AMBER instrument. The incoming light beams (left) are spatially filtered, recombined to an Airy pattern and dispersed with a long-slit spectrograph. The fringes and the three photometric beams are projected onto the detector (right). [Credit: Petrov et al. 2007].

Raw data and data reduction The raw data contains the three spectrally dispersed images (photometric channels) of the three telescopes and an interferometric channel (Figs. 1.18, 1.19). The data can be reduced with the AMBER Data Reduction Software *amdlib* (Tatulli et al. 2007; Chelli et al. 2009). For calibrating the visibility of the science target, an unresolved calibrator star has to be observed. Its magnitude should be as similar as possible to the science target to obtain a similar signal-to-noise ratio (SNR) distribution and its angular distance to the science target should be small to have similar atmospheric disturbances in the light paths of both objects. In the ideal case, the transfer function V_{TF} of the whole night can be determined with the calibrator visibility

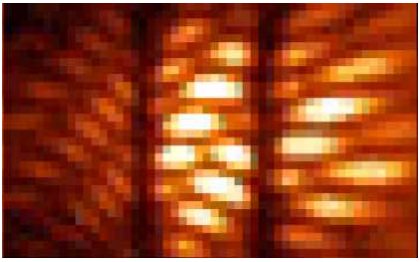

Figure 1.19: One interferometric frame from the observations of V1026 Sco (night 2009-04-17) with fringes in the J, H, and K band (from left to right), separated by the artificial band gaps.

$V_{\text{cal,measured}}$:

$$V_{\text{TF}} = \frac{V_{\text{cal,measured}}}{V_{\text{cal,expected}}} \ . \tag{1.52}$$

The calibrated visibility of the science target is then calculated via:

$$V_{\text{sci}} = \frac{V_{\text{sci,measured}}}{V_{\text{TF}}} \ . \tag{1.53}$$

The contrast in the interferogram is affected by atmospheric turbulence, which causes the fringe pattern to move over time. In addition, instrumental vibrations can reduce the fringe contrast. Following Kreplin et al. (2012), one can optimize the calibrated visibilities of low-resolution observations by comparing the OPD (piston) histograms of the frames of the science target and the associated calibrator. The contribution of frames with a certain OPD value is then adjusted to amount in the same number for science target and calibrator. Employing this method prevents the decrease of the visibility due to random OPD drifts, which is important for observations with a short coherence length.

1.3.3.2 MIDI

The MID-Infrared interferometric instrument (MIDI) is operated in the N band between 8 μm and 13 μm. The instrument combines two beams co-axially and provides a spectral resolution of $R = 30$ (with a prism) or $R = 230$ (with a grism). The photometric measurement can be performed separately from the interferometric measurement in HIGH-SENS mode or simultaneously in SCI-PHOT mode. The limiting correlating magnitude in the N band is 4 mag (prism, HIGH-SENS mode). The seeing is of less importance as MIDI images are almost diffraction-limited. The field of view of MIDI is 1" with the UTs and 5" with the ATs.

In the dispersed-Fourier mode, the OPD is varied in an intervall of several wavelengths while the fringes are scanned continuously. For measuring the OPD, the fringes are Fourier transformed and the position of the fringe peak is determined (group-delay tracking). With self-tracking, the offset information computed from the zero-OPD point is sent to the instrumental delay lines in real-time.

The instrumental setup In the instrument (Fig. 1.20), two incoming beams are compressed and modulated with the internal instrumental delay lines for determining the fringe amplitude. The beams are led into the cryostat (cold box). To reduce the influence of thermal background, part of the cold box is cooled to approximately 40 K, the detector to between 6 K and 12 K. In several steps, unwanted thermal emission is suppressed. After recollimation, the photometric beams can be extracted for the SCI-PHOT mode. The remaining beams are combined with the help of a 50:50 beam splitter. The interferograms are spectrally dispersed with a prism or grism before being imaged on the detector.

Observations in the MIR suffer from strong background emission of the sky and the instrumental thermal emission. To acount for that, the photometric flux of the observed source is determined by so-called chopping: high-frequency switching between the target and an empty sky region by moving the secondary mirror of the telescope. The background emission is removed by subtraction of the two signals.

The interferometric signal is obtained similarly by subtracting both interferometric channels from each other and thereby eliminating the uncorrelated background noise. In the instrument, the two beams with the intensities $I_{A,i}$ and $I_{B,i}$ for $i = 1, 2$ are combined to two beams with the intensities

$$I_1 = I_{A,1} + I_{B,1} + 2V\sqrt{I_{A,1} I_{B,1}}\,\sin(2\pi\Delta s/\lambda + \phi) \tag{1.54}$$

$$I_2 = I_{A,2} + I_{B,2} - 2V\sqrt{I_{A,2} I_{B,2}}\,\sin(2\pi\Delta s/\lambda + \phi)\ ; \tag{1.55}$$

with Δs being the OPD, V the visibility, and the ϕ the phase. Due to the opposite phase in the interferometric part of the two intensities, the noise-biased intensities cancel out and only the interferometric signal remains after substraction of both beams:

$$I_1 - I_2 = 2V(\sqrt{I_{A,1}I_{B,1}} + \sqrt{I_{A,2}I_{B,2}})\sin(2\pi\Delta s/\lambda + \phi(\lambda)) . \tag{1.56}$$

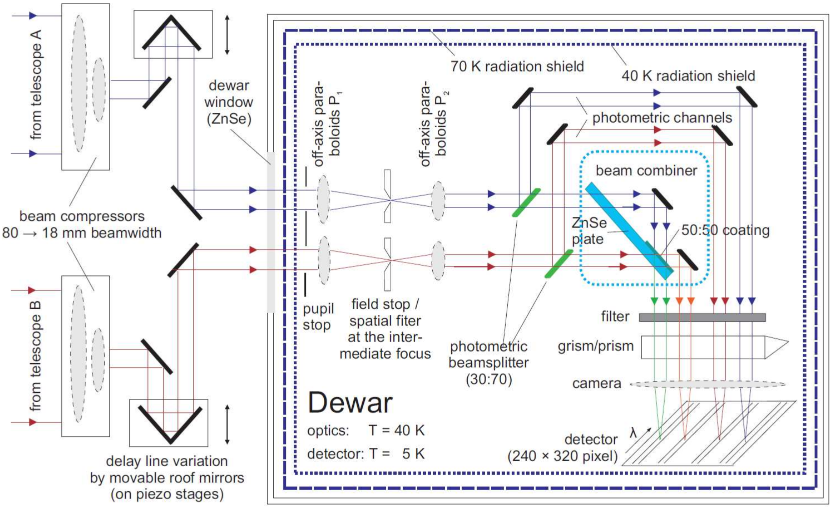

Figure 1.20: Scheme of the MIDI instrument. Two light beams enter the instrument (left). After passing the internal delay lines, they are collimated and led into the cryostat (blue). The photometric beams are split off (green) and the interference is created with a beam splitter (turquoise). The interferogram is spectrally dispersed and imaged onto the detector. [Credit: ESO, Tristram 2007]

Raw data and data reduction The recorded data contain the interferograms and the two photometry exposures of the science target and the calibrator. In addition, acquisition images are available. The calibration procedure is equivalent to the method described in the respective AMBER paragraph.

For the data reduction, there are two different methods, realized by different programs. Two of those programs are available in one software package (Köhler & Jaffe 2008): The Expert Work Station (EWS) provides coherent analysis, which improves the SNR of the visibility amplitude by aligning interferograms before addition. The MIDI Interactive Analysis (MIA) is an incoherent method, where the square visibility amplitude is integrated over time. This amplitude is the result of an integration of the power spectral density of many interferograms.

In this chapter, the basic theoretical background needed for understanding interferometric observation was explained. The drawbacks one has to deal with when performing actually observations were summarized and the interferometric instruments used in this work were described. The next three chapters will now connect the principles explained in this introduction to investigate the circumstellar disks of pre-main sequence stars.

2 Revealing the inner circumstellar disk of the T Tauri star S CrA N using the VLTI

This chapter is based on the publication Vural et al. (2012) and used observations made with ESO telescopes at the La Silla Paranal Observatory under program IDs 081.C-0272(A) and 083.C-0236(C).

2.1 Abstract

We investigate the structure of the circumstellar disk of the T Tauri star S CrA N and test whether the observations agree with the standard picture proposed for Herbig Ae stars.

Our observations were carried out with the VLTI/AMBER instrument in the *H* and *K* bands with the low spectral resolution mode. For the interpretation of our near-infrared AMBER and archival mid-infrared MIDI visibilities, we employed both geometric and temperature-gradient models.

To characterize the disk size, we first fitted geometric models consisting of a stellar point source, a ring-shaped disk, and a halo structure to the visibilities. In the *H* and *K* bands, we measured ring-fit radii of 0.73 ± 0.03 mas (corresponding to 0.095 ± 0.018 AU for a distance of 130 pc) and 0.85 ± 0.07 mas (0.111 ± 0.026 AU), respectively. This *K*-band radius is approximately two times larger than the dust sublimation radius of ≈0.05 AU expected for a dust sublimation temperature of 1500 K and gray dust opacities, but approximately agrees with the prediction of models including backwarming (namely a radius of ≈0.12 AU). The derived temperature-gradient models suggest that the disk is approximately face-on consisting of two disk components with a gap between star and disk. The inner disk component has a temperature close to the dust sublimation temperature and a quite narrow intensity distribution with a radial extension from 0.11 AU to 0.14 AU.

Both our geometric and temperature-gradient models suggest that the

T Tauri star S CrA N is surrounded by a circumstellar disk that is truncated at an inner radius of ≈0.11 AU. The narrow extension of the inner temperature-gradient disk component implies that there is a hot inner rim.

2.2 Introduction

Near- and mid-infrared interferometry is able to probe the inner regions of the circumstellar disks of young stellar objects (YSO) with unprecedented spatial resolution. However, the detailed structure of the inner gas and dust disks is not yet well-known. In particular, the disks of T Tauri stars (TTS) are difficult to study because of their lower apparent brightnesses and the difficulty in spatially resolving them (e.g. Akeson et al. 2005a,b). It is not yet known, for example, whether there is a puffed-up inner rim (PUIR) at the inner edge of TTS, as observed in several Herbig Ae/Be disks (Natta et al. 2001; Dullemond et al. 2001; Muzerolle et al. 2003; Monnier et al. 2005; Cieza et al. 2005). Furthermore, observations suggest that several TTS are surrounded by an additional extended halo of scattered starlight, which influences the precise determination of the disk size (Pinte et al. 2008). The positions of observed TTS in the size-luminosity relation (Eisner et al. 2007b) suggest, that TTS have slightly larger inner disk radii than expected. However, if one compares the TTS radii with predictions of models including backwarming (Millan-Gabet et al. 2007; Dullemond & Monnier 2010), the discrepancy disappears.

In this paper, we investigate the circumstellar disk of the TTS S CrA N, which is the more massive star in the binary S CrA. The binary separation is approximately 1.4″(≈150 AU) (Reipurth & Zinnecker 1993; Ghez et al. 1997) and its position angle (PA) is 157° (Ghez et al. 1997). The binary components are coeval and have an age of ≈3 Myr (Prato et al. 2003). The properties of both stars are listed in Table 2.1.

S CrA N is a classical TTS (McCabe et al. 2006). Its infrared excess suggests the presence of a dusty disk. The precise determination of its spectral type is difficult owing to a strong veiling of the absorption lines (Bonsack 1961). McCabe et al. (2006) inferred a spectral type of K3 and Carmona et al. (2007) obtained a spectral type of G5Ve. The veiling as well as the detection of a strong Brγ flux suggest the presence of an accretion disk (Prato et al. 2003; McCabe et al. 2006). Schegerer et al. (2009) resolved the disk of S CrA N in the mid-infrared with VLTI/MIDI and modeled the spectral energy distribution

Table 2.1: Properties of the S CrA binary components.

Parameter	S CrA N	S CrA S
spectral type	K3	M0
M_* [$M_\odot$]	1.5 ± 0.2	0.6 ± 0.2
T_* [K]	4800 ± 400	3800 ± 400
L_* [$L_\odot$]	2.30 ± 0.70	0.76 ± 0.24
Brγ [10^{-16} Wm^{-2}]	4.23 ± 1.10	1.59 ± 0.57
m_J [mag]	8.6	9.4
m_H [mag]	7.5	8.3
m_K [mag]	6.6	7.3
distance [pc]	130 ± 20	
A_v	2.8 ^{a}	
binary sep. [″]	1.30 ± 0.05 ^{b}/1.4 ^{c}	

Notes. If not mentioned otherwise, the values are taken from Prato et al. (2003). For the spectral type of the primary, Herbig & Bell (1988) found K6 and Carmona et al. (2007) G5Ve. Ortiz et al. (2010) found a distance of 138±16 pc, which is consistent with the table value and the one extensively discussed by Neuhäuser & Forbrich (2008) (130 pc).
Other references: $^{(a)}$ Patten (1998), $^{(b)}$ McCabe et al. (2006), $^{(c)}$ Ghez et al. (1997).

(SED) and visibilities with the Monte Carlo code MC3D to constrain several disk parameters.

The S CrA system is probably connected with Herbig-Haro objects: HH 82A and B are oriented towards a position angle of ≈95°, whereas HH 729A, B and C lie in the direction of ≈115° (Reipurth & Graham 1988). The different PA can, for example, be explained by either two independent outflows from each of the binary components of S CrA or by regarding the HH objects as the edges of an outflow cavity (Wang et al. 2004). The determination of the orientation of the circumstellar disk might clarify the exact relationship.

Walter & Miner (2005) found that the secondary, S CrA S, can be brighter in the optical than the primary for up to one third of the time and that S CrA has one of the most rapidly varying brightnesses of the TTS. This variability is discussed in Graham (1992), who proposes that it is caused by geometrical obscuration as well as accretion processes and emphasizes the probability of clumpy accretion.

Only very recently, Ortiz et al. (2010) observed light echoes in the reflection nebula around S CrA and suggested that the structure is similar to the Oort cloud in our solar system. With their method, they also determined the distance of S CrA (138±16 pc) confirming the previously derived distance of 130 pc (Prato et al. 2003; Neuhäuser & Forbrich 2008).

In this paper, we present VLTI/AMBER observations and the temperature-gradient modeling of the circumstellar disk of S CrA N. In Sect. 2.3, we describe the observations and data reduction. In Sect. 2.4, we describe our modeling, which is discussed in Sect. 2.5.

2.3 Observation and data reduction

Our observations (program IDs 081.C-0272(A) and 083.C-0236(C)) were carried out with the near-infrared interferometry instrument AMBER (Petrov et al. 2007) of the Very Large Telescope Interferometer (VLTI) in the low-spectral-resolution mode ($R = 30$). The observational parameters of our data sets are listed in Table 2.2 and the uv coverage is shown in Fig. 2.1. All data were recorded without using the FINITO fringe tracker. The observations were performed with projected baselines in the range from 16 m to 72 m.

For data reduction, we used *amdlib*-3.0 [*]. A fraction of the interferograms were of low quality. We therefore selected the 20% data with the highest fringe signal-to-noise-ratio of both the target and the calibrator interferograms to improve the visibility calibration (Tatulli et al. 2007). Furthermore, it was impossible to reduce the *H* band data of data set I. We applied an equalisation of the optical path difference histograms of calibrator and target to improve the visibility calibration (Kreplin et al. 2012).

The measured closure phase (Fig. 2.2) is approximately zero, which suggests that it is an approximately symmetric object. However, small closure phases are also expected because the object is only partially resolved. The derived visibilities are shown in Figs. 2.3 and 2.4.

---

[*] `http://www.jmmc.fr/data_processing_amber.htm`

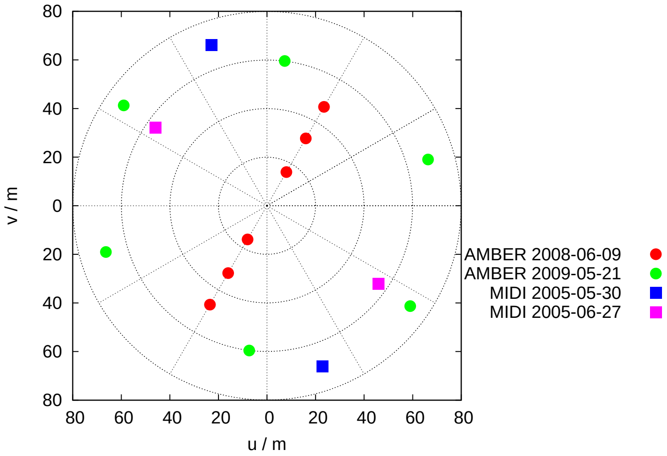

Figure 2.1: The uv coverage of the AMBER (red and green dots) and MIDI (blue and pink squares) observations used for modeling.

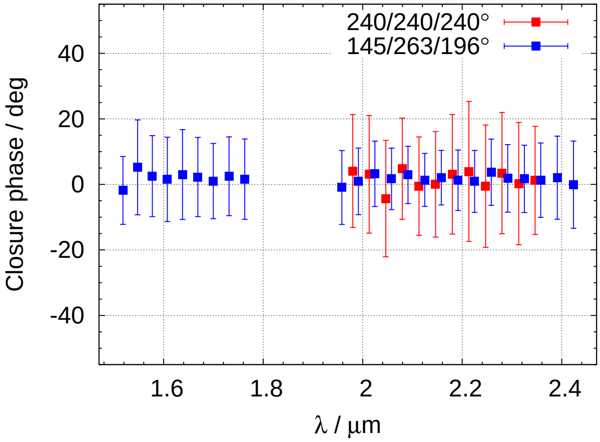

Figure 2.2: Closure phases measured with AMBER in the *H* and *K* bands.

Table 2.2: AMBER observations.

Data set	Night	B_{proj} [m]	PA [°]	Seeing [″]	Airmass	DIT [ms]	Calibrator	Calibrator diameter [mas]
I	2008-06-09	16/32/47	240/240/240	0.91	1.07	100	HD 183 925	1.44±0.02 [a]
II	2009-05-21	60/69/72	145/263/196	0.98	1.06	150	HD 170 773	0.38±0.026 [b]

Notes. The parameters of the MIDI observations used for the modeling in Sect. 2.4.2 are described in Schegerer et al. (2009) and the uv coverage is shown in Fig. 2.1. References: (a) Richichi et al. (2005), (b) Kharchenko & Roeser (2009).

Table 2.3: Overview of the parameter space scanned for the temperature-gradient models and parameters (with errors) of the best-fit models for one temperature-gradient disk (A, B) and two temperature-gradient disk components (C, D, E). For details about the individual models, we refer the reader to Sect. 2.4.2.

Parameter	Scan range	A	B	C	D	E
Constraints				$r_{\mathrm{out},1} = r_{\mathrm{in},2}$ $T_{\mathrm{out},1} = T_{\mathrm{in},2}$	$r_{\mathrm{out},1} = r_{\mathrm{in},2}$	
$r_{\mathrm{in},1}$ [AU]	0.01–0.3	...	...	$0.11^{+0.06}_{-0.04}$	$0.14^{+0.03}_{-0.07}$	$0.13^{+0.04}_{-0.05}$
$r_{\mathrm{out},1}$ [AU]	0.02–4	...	...	$0.14^{+0.05}_{-0.03}$	$0.17^{+0.09}_{-0.05}$	$0.17^{+0.09}_{-0.05}$
$r_{\mathrm{in},2}$ [AU]	0.01–0.6	0.05 ± 0.01	0.05 ± 0.03	$0.14^{+0.05}_{-0.03}$	$0.17^{+0.09}_{-0.05}$	$0.14^{+0.04}_{-0.05}$
$r_{\mathrm{out},2}$ [AU]	1–50	≥ 4	≥ 5	≥ 26	≥ 26	≥ 26
$T_{\mathrm{in},1}$ [T]	100–3000	...	...	1690^{+170}_{-410}	1530^{+330}_{-250}	1500^{+360}_{-220}
$T_{\mathrm{in},2}$ [T]	200–3000	1900^{+90}_{-150}	1890^{+20}_{-140}	660^{+90}_{-160}	633^{+130}_{-120}	660^{+90}_{-60}
q_1	0.35–0.85	...	...	0.2 ± 0.2	0.5 ± 0.4	0.5 ± 0.4
q_2	0.3–0.9	$0.75^{+0.1}_{-0.08}$	0.75 ± 0.1	0.5 ± 0.1	$0.5^{+0.12}_{-0.04}$	$0.5^{+0.12}_{-0.04}$
f_{halo}	0–1	...	0.2 ± 0.1	...	...	...
χ^2_{red}		16.9	11.5	3.2	3.0	3.0

2.4 Modeling

2.4.1 Geometric models

To measure the characteristic size of the circumstellar environment in the *H*- and *K*-bands, we fitted geometric models to the visibilities. Figure 2.3 shows the observed visibilities and the fitted models, which consist of a ring (the ring width being 20% of the inner radius; Eisner et al. 2003; Monnier et al. 2005), a stellar point source, and an extended fully resolved halo (in only the lower two panels). This extended halo is assumed to represent the stellar light scattered off a large-scale circumstellar structure (Akeson et al. 2005b). The motivation for a ring fit is that the model intensity distribution is expected to have a dominant PUIR brightness (Natta et al. 2001; Dullemond et al. 2001). Ring-fit radii are often used in the literature to characterize the disk size of YSO and to discuss their location in the size-luminosity relation (e.g. Monnier & Millan-Gabet 2002; Dullemond & Monnier 2010).

The flux contribution $f_{\rm star} + f_{\rm halo}$ from the star ($f_{\rm star}$) plus a halo of scattered starlight ($f_{\rm halo}$) was derived from the SED fit in Fig. 2.6 and amounts to 0.22 of the total flux (i.e. $f_{\rm star} + f_{\rm halo} + f_{\rm disk}$) in the *K* band (2.2 μm) and 0.40 in the *H* band (1.6 μm). The total visibility V can be described by

$$|V| = |(1 - f_{\rm star} - f_{\rm halo})V_{\rm disk} + f_{\rm star}V_{\rm star} + f_{\rm halo}V_{\rm halo}| \,, \tag{2.1}$$

where $V_{\rm star} = 1$ and $V_{\rm halo} = 0$.

In fitting the data, we averaged the visibility data in each of the two bands. The *H* band visibilities were averaged over the wavelength range of ≈1.55–1.75 μm and the *K* band visibilities over ≈1.95–2.40 μm.

For the inner fit radius $r_{\rm ring,in}$, we obtained 0.73 ± 0.03 mas in the *H* band and 0.85 ± 0.07 mas in the *K* band. The linear radii in AU for a distance of 130 pc (see Table 2.1) are listed in Table 2.4.

To test whether an elongation of the object can be measured, we also fitted an elliptic ring model. However, we were unable to detect any significant elongation. Because of the errors in the data, we can only derive a rough estimate of the elongation of $< 30\%$. Therefore, we assume in the following modeling that the disk is oriented approximately face-on.

Table 2.4: Ring-fit parameters in the *H* and *K* bands. The error in the distance measurement (130 ± 20 pc, see Table 2.1) is included in the errors in the radii.

Model	Band	$r_{\mathrm{ring,in}}$ [AU]	f_{halo}	f_*	f_{disk}
ring-star	*H*	0.120 ± 0.020	0	0.40 ± 0.09	0.60 ± 0.09
ring-star	*K*	0.134 ± 0.027	0	0.22 ± 0.05	0.78 ± 0.05
ring-star-halo	*H*	0.095 ± 0.018	0.08 ± 0.05	0.32 ± 0.14	0.60 ± 0.09
ring-star-halo	*K*	0.111 ± 0.026	0.06 ± 0.04	0.16 ± 0.09	0.78 ± 0.05

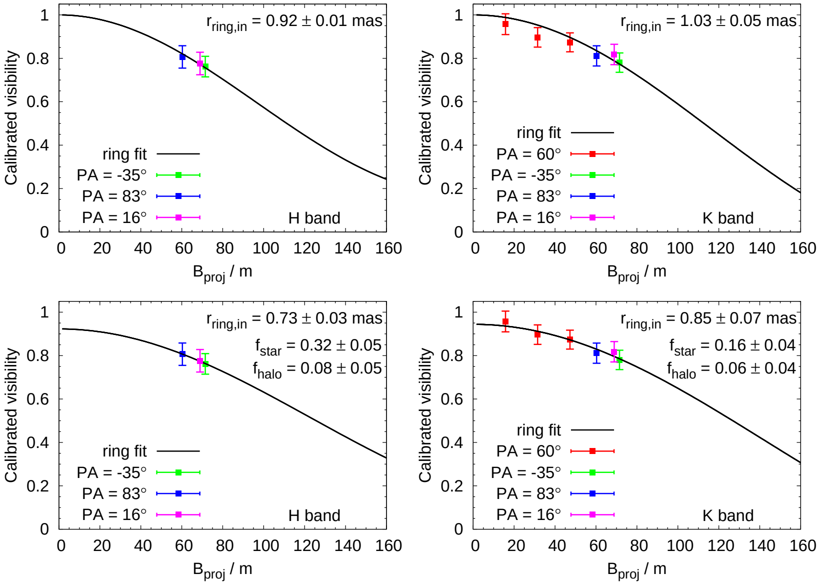

Figure 2.3: *Top:* *H*-band (left) and *K*-band (right) visibilities of S CrA N together with ring-fit models (described in Sect. 2.4.1) consisting of a circular symmetric ring (ring width = 20% of inner ring radius $r_{\mathrm{ring,in}}$) and an unresolved stellar source. *Bottom:* Models consisting of the same star+ring model as above, plus a fully resolved halo component.

2.4.2 Temperature-gradient disk model

In this section, we present temperature-gradient models to help us interpret our observations. Each temperature-gradient model is the sum of many rings that emit blackbody radiation with temperatures $T(r)$. For the temperature distribution, a power law is assumed (Hillenbrand et al. 1992), of $T(r) = T_0\,(r/r_0)^{-q}$. Here, T_0 is the effective temperature at a reference radius r_0. The parameter q depends on the disk morphology and is predicted to be 0.50 for flared irradiated disks and either 0.75 for standard viscous disks or flat irradiated disks (Chiang & Goldreich 1997). Wavelength-dependent visibilities and fluxes of these model disks depend on the disk inclination, the inner radius $r_{\rm in}$, the outer radius $r_{\rm out}$, the temperature $T_{\rm in}$ at $r_{\rm in}$, and the temperature power-law index q. As explained in Sect. 2.4.1, we assumed that the disk is viewed face-on.

To determine the best temperature-gradient model, we calculated the model disks (one- and two-component structures) for all combinations of the parameters with scan ranges described in Table 2.3 ($\approx$400 000 models). The total $\chi^2_{\rm red}$ is a sum over the $\chi^2_{\rm red}$ of all visibility points for all six AMBER baselines and two MIDI baselines (see Schegerer et al. 2009), and the SED. We computed all combinations by running the model for six to ten steps per parameter and then chose the areas with the smallest value of $\chi^2_{\rm red}$ to obtain a finer mesh. We took into account only wavelengths with $\lambda < 20\mu$m. The errors in the best-fit model parameters are 1-σ errors.

The model assumes a stellar point source with the parameters $T_* = 4800$ K, $L_* = 2.3 L_\odot$, distance = 130 pc, and $A_{\rm v} = 2.8$ (see references for the stellar parameters in Table 2.1). The model parameters of all derived models (disk plus star, disk plus star plus halo, as well as several two-component disks) are listed in Table 2.3.

2.4.2.1 One-component temperature-gradient disk models

The simplest temperature-gradient model A (see Table 2.3) consists of only one single disk component plus the star. It cannot reproduce the SED as well as the MIR and NIR visibilities simultaneously ($\chi^2_{\rm red}$ $\approx$17).

For the star-disk-halo model B, we added a fully resolved halo ($V = 0$) to the star-disk model A. This halo intensity distribution is assumed to represent the stellar light scattered off the large-scale circumstellar material and to have approximately the same SED as the star itself (cf. Akeson et al. 2005b). Nevertheless, the improvement achieved was very small since the χ^2_{red} became only 11.5 (see Table 2.3). We also computed 20 star-disk-halo models with resolved halos of different widths in the range from 0.05 AU to 100 AU, but the χ^2_{red} did not significantly improve since it remained larger than ≈11.5 in all cases. As in the case of model A without a halo, it was only possible to fit either the SED and the AMBER measurements or the SED and the MIDI measurements. This suggests that a more complicated disk structure should be considered. Therefore, we introduced a second disk component in the following, but – as we preferred to adopt a two-disk modeling with a minimum number of free parameters – we omitted the weak halo.

2.4.2.2 Two-component temperature-gradient disk models

Model C is the result of our attempt to find a two-disk component model with the least number of parameters (Table 2.3). We therefore introduced constraints on the inner and outer radii and temperatures of disks 1 and 2, of $T_{\mathrm{out},1} = T_{\mathrm{in},2}$ and $r_{\mathrm{out},1} = r_{\mathrm{in},2}$. We obtained $\chi^2_{\mathrm{red}} = 3.2$ (the power-law index q_1 is determined from the temperature slope between $r_{\mathrm{in},1}$ and $r_{\mathrm{out},1}$ and is therefore no longer a free parameter).

We also tested models with more parameters: In model D, $r_{\mathrm{out},1} = r_{\mathrm{in},2}$ is the only constraint and $\chi^2_{\mathrm{red}} = 3.0$. For model E, there are no constraints, but we still get a similar χ^2_{red} (3.0). Table 2.3 shows that only models C to E have a χ^2_{red} from 3.0 to 3.2 and among those, model C has the advantage that it has the smallest number of parameters.

Figure 2.4 and Fig. 2.5 show the results of model C for the AMBER and MIDI visibilities of S CrA N, Fig. 2.6 displays the SED, and Fig. 2.7 shows the intensity distribution. An extended ring is located between 0.14 AU and 26 AU, whereas the inner ring extends radially from 0.11 AU to 0.14 AU and has a temperature of 1690 K at the inner ring edge (see parameters in Table 2.3).

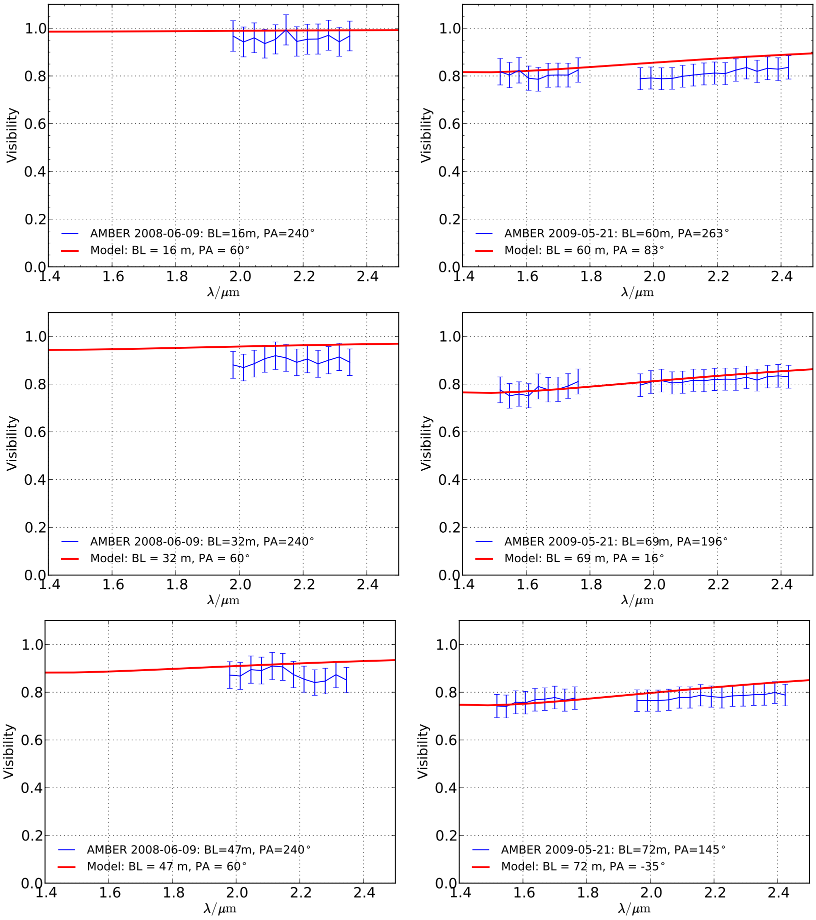

Figure 2.4: Temperature-gradient model C of S CrA N – NIR visibility. The model that fits visibility and SED simultaneously (model C in Table 2.3) is indicated with the solid red lines. The six figures show the modeling of the data sets I (left) and II (right), described in Table 2.2.

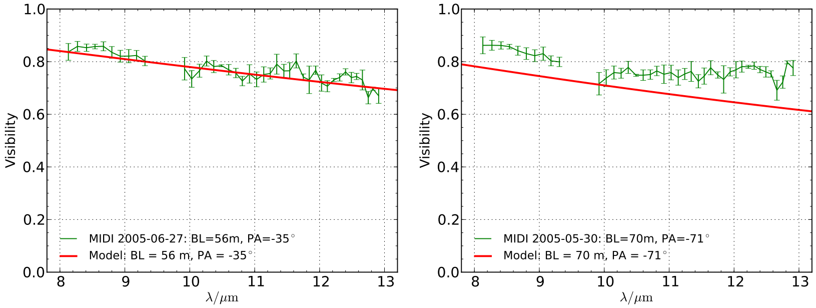

Figure 2.5: MIDI visibility. The two figures show the comparison between our model (red line) and MIR data adopted from Schegerer et al. (2009).

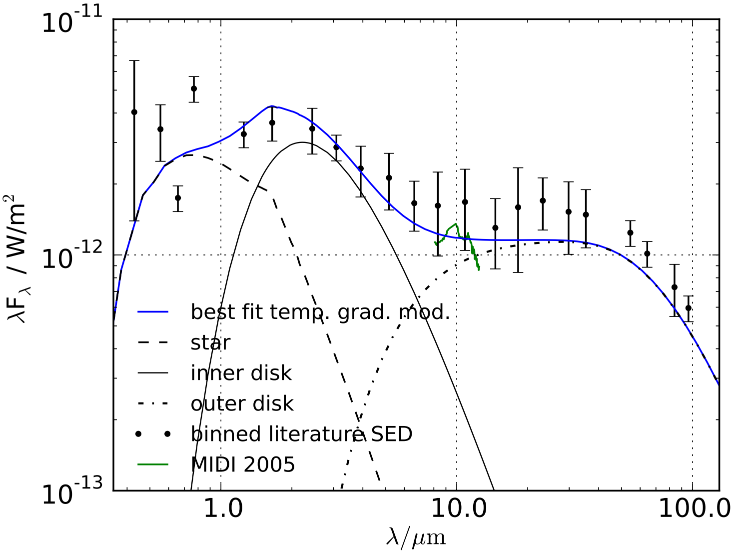

Figure 2.6: Temperature-gradient model C of S CrA N – *Left:* Spectral energy distribution. To model the SED of S CrA N, we collected values from the literature and binned them (black dots are the dereddened SED points, see Appendix 2.7.1). The green line represents the MIDI spectrum of Schegerer et al. (2009). The SED of model C is indicated with the blue line. It consists of the stellar contribution (Kurucz model, black dashed line) plus the contribution of two additional ring-like structures (black solid and dash-dotted line).

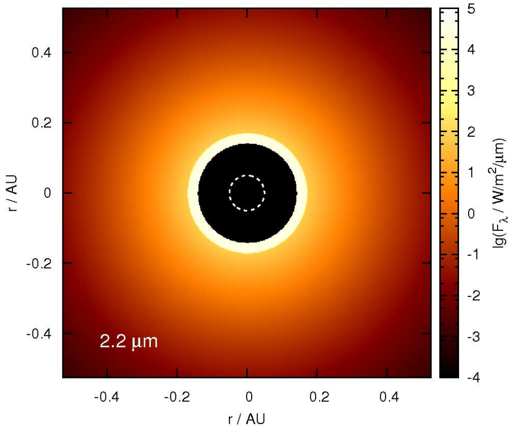

Figure 2.7: Intensity distribution of the temperature-gradient disk of model C. The dashed white ring indicates the expected dust sublimation radius of 0.05 AU predicted by the size-luminosity-relation (see Sect. 2.5).

2.5 Discussion

For comparison with other pre-main sequence stars, we plot the geometric *K*-band ring-fit radii, where $r_{\mathrm{ring,in}} \approx 0.13$ AU for the geometric model without a halo and ≈0.11 AU for the model with a halo; Sect. 2.4.1, of S CrA N in the size-luminosity diagram that shows the *K*-band ring-fit radius as a function of the stellar luminosity L_* (Monnier & Millan-Gabet 2002, Fig. 2.8). The figure shows a sample of Herbig Ae stars (filled squares, Monnier et al. 2005), for which this correlation has been originally found. Additionally, we plot a sample of TTS (open squares, Pinte et al. 2008).

Figure 2.8 shows that our measurements of the *K*-band ring-fit radius of S CrA N of ≈0.11–0.13 AU, radii derived with the geometric ring-star and ring-star-halo models, is approximately 2.4 times larger than the dust sublimation radius of ≈0.05 AU predicted for the silicate dust sublimation temperature of 1500 K and gray dust opacities (Monnier & Millan-Gabet 2002). However, several effects can influence the inner model radius, such as the chemistry and grain size of the dust (e.g. Monnier & Millan-Gabet 2002) or magnetospherical disk truncation (Eisner et al. 2007b). Schegerer et al. (2009) modeled their mid-infrared MIDI data and the SED of S CrA N using the Monte Carlo code MC3D (Wolf et al. 1999; Schegerer et al. 2008). They found that an assumed sublimation radius of 0.05 AU agrees with their observations.

Furthermore, we compared our ring-fit radii of ≈0.11–0.13 AU derived from the geometric star-disk and star-disk-halo models and the inner disk radii of our temperature-gradient models (0.11–0.14 AU) with the predictions of a model that accounts for both backwarming and accretion luminosity (Millan-Gabet et al. 2007; Dullemond & Monnier 2010). This model suggests an inner disk radius of 0.12 AU for a stellar luminosity of 2.3 $L_{\odot}$ and an accretion luminosity of 0.6 $L_{\odot}$ (derived from Prato et al. 2003; Muzerolle et al. 1998), which agrees with our measured inner radius of ≈0.11–0.13 AU.

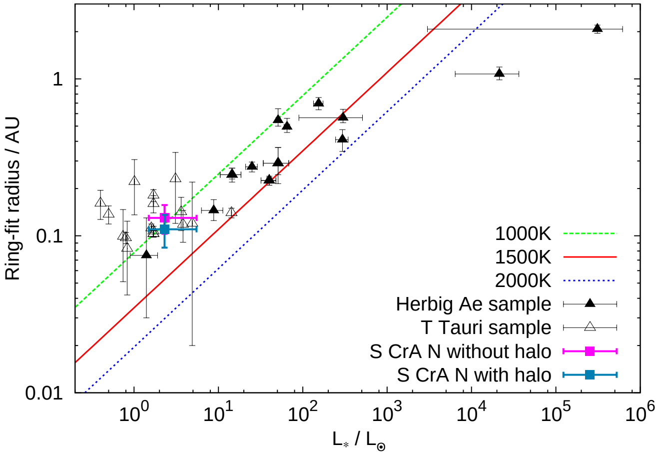

Figure 2.8: Location of S CrA N in the size-luminosity diagram: K-band ring-fit radii derived with a geometric ring-star model (pink square, ≈0.13 AU) and a ring-star-halo model (blue square, ≈0.11 AU); see Tables 2.4 and 2.1 for the stellar parameters used. The lines indicate the predicted theoretical dependence of the K-band radius on the luminosity (Monnier & Millan-Gabet 2002). Predictions of models including backwarming are discussed in Sect. 2.5. The filled black squares are a sample of Herbig Ae stars (Monnier et al. 2005). The open black squares represent a sample of TTS (Pinte et al. 2008).

2.6 Conclusions

We have observed the T Tauri star S CrA N with AMBER in the *H* and *K* bands. We have fitted the geometric star-disk and star-disk-halo models to our visibility data and derived a radius $r_{\mathrm{ring,in}}$ of approximately 0.11–0.13 AU in the *K* band (0.095–0.12 AU in the *H* band). We compared the position of S CrA N in the size-luminosity diagram with the position of other YSO, and found that it is above the line expected for a dust sublimation temperature of 1500 K and gray dust, but within the region of other TTS. The radius predicted by this size-luminosity relation is ≈0.05 AU, whereas the derived ring-fit radius is ≈0.11–0.13 AU (Table 2.4). However, models including backwarming (Millan-Gabet et al. 2007; Dullemond & Monnier 2010) suggest a larger inner disk radius of ≈0.12 AU, which agrees with our derived ring-fit radiii of ≈0.11–0.13 AU.

We tested several temperature-gradient models (one- and two-component disk models, with or without halo). We found that the near- and mid-IR visibilities, as well as the SED, can approximately be reproduced by a temperature-gradient model consisting of a two-component ring-shaped disk and an unresolved star. The favored temperature-gradient model C (see Table 2.3) has a temperature of ≈1700 K at the inner disk radius of 0.11 AU. The temperature power-law index q_1 of the inner narrow temperature-gradient disk is approximately 0.2, and the index q_2 of the extended outer disk is approximately 0.5, which suggests a flared irradiated disk structure (Chiang & Goldreich 1997). However, q_1 is not well-constrained because of the narrow width of the inner component of only ≈0.03 AU. The inner temperature-gradient disk radius of 0.11 AU is similar to the four geometric ring-fit radii of approximately 0.10 AU to 0.13 AU and to the prediction of models including backwarming (0.12 AU). Unfortunately, we cannot place any constraints on the gas within the inner disk radius of ≈0.11 AU since the disk is only partially resolved (all NIR visibilities are > 0.77) and the visibility errors are large. Interestingly, the inner disk components of all three best-fit temperature-gradient models consist of a very narrow, hot ring ($T_{\mathrm{in},1} \approx$ 1500–1700 K; ring width only ≈0.03–0.04 AU) surrounded by a colder (<600 K) disk component with an extension of several AU. This size and temperature structure is similar to the structure of more sophisticated radiative transfer models including a hot PUIR (e.g., Natta et al. 2001; Dullemond et al. 2001). This suggests that the derived narrow, inner disk component in the temperature-gradient models is caused by a hot, perhaps PUIR, in S CrA N. This rim may explain the steep temperature jump from 1500 to 600 K.

2.7 Appendix

2.7.1 SED references

To simplify the fitting process, we did not use the pile of original data (Table 2.5), but instead binned them to form a smaller number of data points. Figure 2.9 shows both the original data (blue crosses) and the binned data (red dots). The measurements were not recorded contemporaneously (see Table 2.5) and therefore variability is one of the error sources. Other SED error sources are the different aperture sizes and the small number of observations in the visible and NIR.

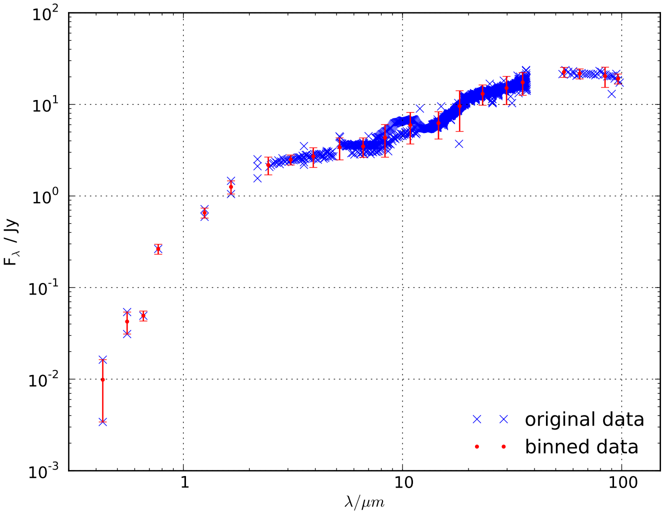

Figure 2.9: SED of S CrA N – original data according to the sources in Table 2.5 (blue crosses) and the binned data (red dots).

Table 2.5: Measurements from the literature that were used to produce the binned SED of S CrA N. A beam width of 10” or larger most probably also includes the light from the secondary S CrA S (separation 1.4”).

Wavelength range	Reference	Beam
2.47-11.62	ISO spectrum	
3.5-170	ISO	
53.6-106	Spitzer MIPS	2.7 x 0.34′
5.13-36.9	Spitzer IRS	55x81”
12-100	IRAS	10”
450-1100	JCMT (upper limit)	10”
12-100	Gezari catalog	10”
0.768	Denis 2005	0.5”
0.429, 0.554	Tycho catalog	10”
0.657, 0.429	USNO	10”
0.554	WDS	0.5”
1.25-3.55	Prato 2003	0.5”
2.18-18.1	McCabe 2005	0.5”
1.25-3.55	Morel 1978	10”

3 The inner circumstellar disk of the UX Ori star V1026 Sco

This chapter is based on the publication Vural et al. (2014b) and made use of observations carried out with ESO telescopes at the La Silla Paranal Observatory under programme IDs 083.D-0224(C), 083.C-0236(A), 087.C-0013(A) and 073.A-9014(A).

3.1 Abstract

The UX Ori type variables (named after the prototype of their class) are intermediate-mass pre-main sequence objects. One of the most likely causes of their variability is the obscuration of the central star by orbiting dust clouds.

We investigate the structure of the circumstellar environment of the UX Ori star V1026 Sco (HD 142666) and test whether the disk inclination is large enough to explain the UX Ori variability.

We observed the object in the low-resolution mode of the near-infrared interferometric VLTI/AMBER instrument and derived *H*- and *K*-band visibilities and closure phases. We modeled our AMBER observations, published Keck Interferometer observations, archival MIDI/VLTI visibilities, and the spectral energy distribution using geometric and temperature-gradient models.

Employing a geometric inclined-ring disk model, we find a ring radius of 0.15 ± 0.06 AU in the *H* band and 0.18 ± 0.06 AU in the *K* band. The best-fit temperature-gradient model consists of a star and two concentric, ring-shaped disks. The inner disk has a temperature of 1257^{+133}_{-53} K at the inner rim and extends from 0.19 ± 0.01 AU to 0.23 ± 0.02 AU. The outer disk begins at $1.35^{+0.19}_{-0.20}$ AU and has an inner temperature of 334^{+35}_{-17} K. The derived inclination of $48.6^{+2.9}_{-3.6}{}^{\circ}$ approximately agrees with the inclination derived with the geometric model ($49 \pm 5^{\circ}$ in the *K* band and $50 \pm 11^{\circ}$ in the *H* band). The position angle of the fitted geometric and temperature-gradient models are $163 \pm 9^{\circ}$ (*K* band; 179 ± 17° in the *H* band) and $169.3^{+4.2}_{-6.7}{}^{\circ}$, respectively.

The narrow width of the inner ring-shaped model disk and the disk gap might

be an indication for a puffed-up inner rim shadowing outer parts of the disk. The intermediate inclination of ~50° is consistent with models of UX Ori objects where dust clouds in the inclined disk obscure the central star.

3.2 Introduction

The UX Ori (UXOr) phenomenon of Herbig Ae/Be stars (HAeBes) is attributed to obscuration by circumstellar dust in an inclined disk (Grinin et al. 1994; Natta et al. 1997; Grinin et al. 2001; Dullemond et al. 2003) or unsteady accretion (Herbst & Shevchenko 1999). The Herbig Ae star V1026 Sco (HD 142666) has a spectral type of A8Ve (Dominik et al. 2003) and is classified as a UX Ori object (Meeus et al. 1998). The UX Ori variability has been confirmed by Zwintz et al. (2009). Dominik et al. (2003) and van Boekel et al. (2005b) report distances of 116 pc and 145 ± 43 pc, respectively. We adopt the Hipparcos-based measurement of 116 pc and the associated parameters for our work. The object V1026 Sco shows large, non-periodic (Lecavelier des Etangs et al. 2005) brightness variations (>1.2 mag) and a pulsational variability on the milli-magnitude level (Zwintz et al. 2009). It reddens with decreasing apparent magnitude (Meeus et al. 1998). These authors suggest that dense dust clouds in an inclined disk cause the stellar reddening. Alecian et al. (2013a) report on the magnetic properties of V1026 Sco (and several other Herbig Ae/Be stars). The object V1026 Sco belongs to the Meeus group IIa (Juhász et al. 2010) and might, therefore, have a self-shadowed disk. The stellar parameters (Dominik et al. 2003) of V1026 Sco are listed in Table 3.1. By modeling the spectral energy distribution (SED), Dominik et al. (2003) found that the circumstellar disk of V1026 Sco has an inclination of approximately 55°. Monnier et al. (2005) have performed Keck Interferometer (KI) measurements of V1026 Sco and found an inner disk diameter of 2.52 mas (0.29 AU at 116 pc). In a recent publication, Schegerer et al. (2013) have reported mid- and near-infrared interferometric observations (archival MIDI/VLTI & IOTA data), and performed radiative transfer modeling of V1026 Sco, and derived a disk structure with a gap from 0.35 AU to 0.80 AU.

In this paper, we analyze the circumstellar environment around V1026 Sco by taking new interferometric near-infrared (NIR) VLTI/AMBER and archival mid-infrared (MIR) VLTI/MIDI measurements into account. We describe our observations and the data reduction in Sect. 3.3. The modeling is presented in

Sect. 3.4, and our results are discussed in Sect. 3.5.

Table 3.1: The adopted stellar parameters of HD142666.

Parameter	Value
spectral type	A8Ve $^{(a)}$
age [Myr]	6.0 ± 1.5 $^{(b)}$
distance [pc]	116
$M_*[M_\odot]$	1.8
$L_*[L_\odot]$	11
T_*[K]	8500
$log(\dot{M}[M_\odot \mathrm{yr}^{-1}])$	-6.73 ± 0.26 $^{(c)}$

Notes. The values are taken from Dominik et al. (2003) unless otherwise noted. The error bars are shown where available. Dominik et al. (2003) estimate the uncertainty of the luminosity to be ±50% (due to the Hipparcos distance error) and the mass uncertainty to be 5 – 10%. Other authors find slightly different parameters for the alternative distance of 145 ± 20 pc. For example Alecian et al. (2013a) derived $5.0^{+1.6}_{-1.1}$ Myr, $2.15^{+0.20}_{-0.19} M_\odot$, $27.5^{+7.9}_{-7.1} L_\odot$, and 7900 ± 200 K. Other references: $^{(a)}$Meeus et al. (1998), $^{(b)}$Folsom et al. (2012), $^{(c)}$Mendigutía et al. (2011).

3.3 Observation and data reduction

We observed V1026 Sco on three different nights with the NIR three-beam VLTI/AMBER instrument (Petrov et al. 2007). The observations were performed in low-resolution mode (spectral resolution $R = 30$). Table 3.2 lists the observational parameters. The uv coverage of our 2009 and 2011 AMBER observations with the published KI and archival MIDI observations of V1026 Sco used in this study are shown in Figure 3.1.

We reduced the AMBER data with *amdlib-3.0.2*[*] (Tatulli et al. 2007; Chelli et al. 2009). To improve the calibrated visibility, we processed only 20% of the frames (object and calibrator) with the best fringe signal-to-noise ratio (Tatulli et al. 2007). In addition, we equalized the histograms of the optical path differences (OPD) of the calibrator and the object data, because different histograms (due to OPD drifts caused, for example, by errors of the OPD model) can lead

---

[*] `http://www.jmmc.fr/data_processing_amber.htm`

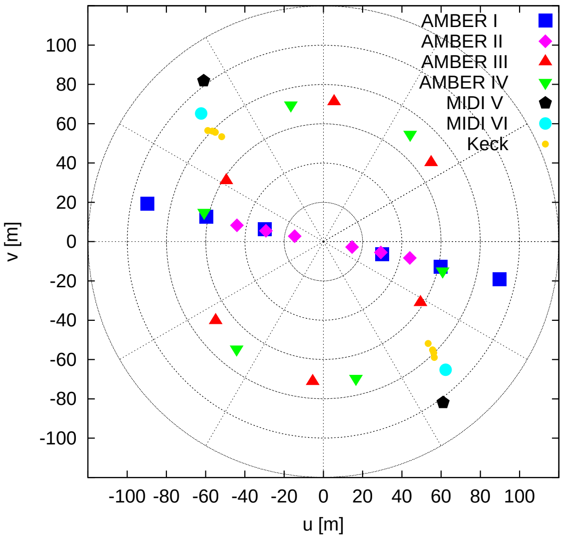

Figure 3.1: The uv coverage of all interferometric measurements used (AMBER, MIDI, Keck; see Table 3.2).

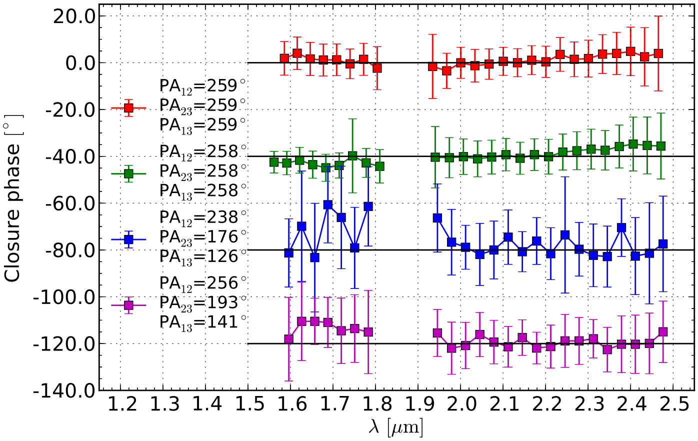

Figure 3.2: Wavelength dependence of the closure phases of all AMBER measurements from Table 3.2. The curves are offset from each other by 40°. The respective zero line is indicated as a solid horizontal line.

Table 3.2: Observation log.

#	Night	Instrument	B_{proj} [m]	PA [°]	Seeing [″]	DIT [ms]	Calibrator	Calibrator diameter [mas]
I	2009-04-17	AMBER	15/30/45	259/259/259	0.55	200	HD142669	0.256 ± 0.018 [a]
II	2009-05-22	AMBER	31/61/91	258/258/258	0.8	150	HD142669	0.256 ± 0.018 [a]
III	2011-04-30	AMBER	59/68/71	238/126/176	1.0	300	HD138472	1.07 ± 0.02 [b]
IV	2011-04-30	AMBER	63/70/72	256/141/193	0.8	300	HD138472	1.07 ± 0.02 [b]
V	2004-06-07	MIDI	102	37	0.9	14	HD146791	3.00 ± 0.033 [c]
VI	2004-06-07	MIDI	90	44	1.1	18	HD169916	4.24 ± 0.047 [c]

Notes. B_{proj} denotes the lengths of the projected interferometer baselines during the observations, PA the baseline position angles, and DIT the detector integration time for recording individual interferograms. The resulting uv coverage is shown in Fig. 3.1. References: [a]Lafrasse et al. (2010), [b]Richichi et al. (2005), [c]Bordé et al. (2002).

Table 3.3: Scanned range of the parameters of the computed temperature-gradient models (A, B_1, B_2 and B_3).

Parameter	Range (A)	N(A)	Range (B_1)	N(B_1)	Range (B_2)	N(B_2)	Range (B_3)	N(B_3)
$r_{\text{in},1}$ [AU]	0.01 – 1.0	30	0.05 – 1.0	8	0.1 – 0.3	8	0.15 – 0.25	10
$\Delta r_{\text{in},1}$ [AU]	0.01 – 10	30	0.01 – 2.0	8	0.01 – 0.15	8	0.02 – 0.07	8
$r_{\text{in},2}$ [AU]	...	...	0.05 – 3.0	8	0.4 – 2.0	8	1.0 – 1.7	8
$\Delta r_{\text{in},2}$ [AU]	...	...	0.01 – 10	8	0.5 – 10	8	1.0 – 6.0	4
$T_{\text{in},1}$ [K]	200 – 2000	30	800 – 2000	8	1000 – 1500	8	1200 – 1400	8
$T_{\text{in},2}$ [K]	...	...	150 – 1000	8	100 – 400	8	300 – 380	8
q_1	0.2, 0.5, 0.75, 1.0	4	0.2, 0.5, 0.75, 1.0	4	0.2, 0.5, 0.75, 1.0	4	0.2, 0.5, 0.75, 1.0	4
q_2	...	...	0.2, 0.5, 0.75, 1.0	4	0.2, 0.5, 0.75, 1.0	4	0.2, 0.5, 0.75, 1.0	4
i [°]	0 – 90	30	0 – 80	6	10 – 60	6	40 – 60	8
ϑ [°]	0 – 170	30	0 – 160	6	130 – 180	6	150 – 180	8

Notes. The free model parameters for the inner ($j = 1$) and, if included, outer ($j = 2$) ring-shaped disk are as follows: the inner ring radius $r_{\text{in,j}}$, the ring width $\Delta r_{\text{in,j}}$, the temperature at the inner radius $T_{\text{in,j}}$, the power-law index q_j, the inclination i, and the position angle of the semi-major axis ϑ. The number of steps computed per parameter is given by N. The step spacing is logarithmic for $r_{\text{in},1}$, $\Delta r_{\text{in},1}$, and $r_{\text{in},2}$, and is linear for the rest of the parameters except q_1 and q_2, for which the individual values used are given directly.

to visibility errors. Histogram equalization can reduce these visibility errors. This method is described in detail in Kreplin et al. (2012).

We were able to extract H and K band visibilities (cf. Fig. 3.4). Within the error bars, the obtained closure phase is zero for all nights (Fig. 3.2), which is consistent with a centro-symmetric brightness distribution.

We also used archival low-resolution data obtained with the MIR two-beam combiner MIDI (Leinert et al. 2003; Schegerer et al. 2013). The data (see Table 3.2) were reduced using our own IDL codes (see Appendix A of Kishimoto et al. 2011 for details), which utilize a part of the standard software EWS† and also implement an average over a relatively large number of frames to determine the group-delay and phase-offset tracks with a good signal-to-noise ratio. This is important when dealing with sub-Jy sources, such as our target here. The MIDI visibilities are shown in Fig. 3.5 (right).

3.4 Analysis

3.4.1 Geometric modeling

To estimate the characteristic size of the NIR emission region, we fit geometric models to the visibilities. The model for the NIR data consists of an unresolved stellar contribution and an inclined ring with a width of 20% of its inner radius $r_{\mathrm{ring,in}}$ (,which is equal to the semi-major axis in the model). We averaged the different visibility measurements (shown in Fig. 3.4) of the spectral channels within the H and K bands to obtain wavelength-averaged H- and K-band visibilities (Fig. 3.3). The resulting visibilities within each band were fit with the model visibilities of the two-dimensional, inclined star-ring model.

In the K band, we included literature data from the Keck interferometer (Monnier et al. 2005, see Fig. 3.1) in the fit. Because of the almost constant projected baseline length and position angle of the five KI measurements, the data points were averaged.

To fit the visibilities, we derived the NIR flux contribution of the star (f_{star}) from our SED fit (Fig. 3.6 left) and obtained approximately 0.33 (Monnier et al. 2005 report 0.39) in the K band and 0.53 in the H band. For the total visibility, we obtain

$$|V| = |(1 - f_{\mathrm{star}})V_{\mathrm{disk}} + f_{\mathrm{star}}V_{\mathrm{star}}| \,, \tag{3.1}$$

---

† `http://www.strw.leidenuniv.nl/~nevec/MIDI/index.html`

where $f_{\rm star} + f_{\rm disk} = 1$ and the unresolved star has $V_{\rm star} = 1$.

We found a semi-major axis ($r_{\rm ring,in}$) of 1.30 ± 0.14 mas (or 0.15 ± 0.06 AU for a distance of 116 pc) in the *H* band and 1.57 ± 0.09 mas (or 0.18 ± 0.06 AU) in the *K* band (Fig. 3.3). All fitted parameters are listed in Table 3.4. In the *H* band, the inclination angle i (angle between the system axis and the viewing direction) is $50 \pm 11°$, and the position angle ϑ of the semi-major axis of the disk is $179 \pm 17°$. In the *K* band, we derived $i = 49 \pm 5°$ and $\vartheta = 163 \pm 9°$, respectively.

Table 3.4: Parameters of the best-fit geometric model.

Band	$r_{\rm ring,in}$ [AU]	i °	ϑ °	$f_{\rm star}$	$f_{\rm disk}$
H	0.15 ± 0.06	50 ± 11	179 ± 17	0.53 ± 0.10	0.47 ± 0.10
K	0.18 ± 0.06	49 ± 5	163 ± 9	0.33 ± 0.27	0.67 ± 0.27

Notes. The radius $r_{\rm ring,in}$ represents the inner semi-major axis of the inclined model ring; the position angle ϑ denotes the position angle of the semi-major axis; i is the inclination of the system axis to the line of sight, $f_{\rm star}$ the flux contribution from the star, and $f_{\rm disk}$ the flux contribution from the disk to the total flux (see text in Sect. 3.4.1). The errors of the radii include the distance error (116 ± 30 pc).

3.4.2 Temperature-gradient model

To fit all available wavelength-dependent visibilities (AMBER, MIDI, and KI, see Figs. 3.4, 3.5) and the SED (Fig. 3.6) simultaneously, we used a temperature-gradient model. This model consists of many thin rings emitting blackbody radiation at a local temperature $T(r) = T_0 \cdot (r/r_0)^{-q}$, where r_0 denotes the inner disk radius, T_0 the effective temperature at r_0, and q the power-law index. Other free parameters are the inclination i and the position angle ϑ of the semi-major axis of the disk. A more detailed description of our modeling of temperature-gradient disks can be found, for example, in Vural et al. (2012) or Kreplin et al. (2012).

We computed models for all mathematical combinations of the parameter values listed in Table 3.3. We chose the model with the lowest $\chi^2_{\rm red}$ value as the best-fit model. The given error bars are 3σ errors.

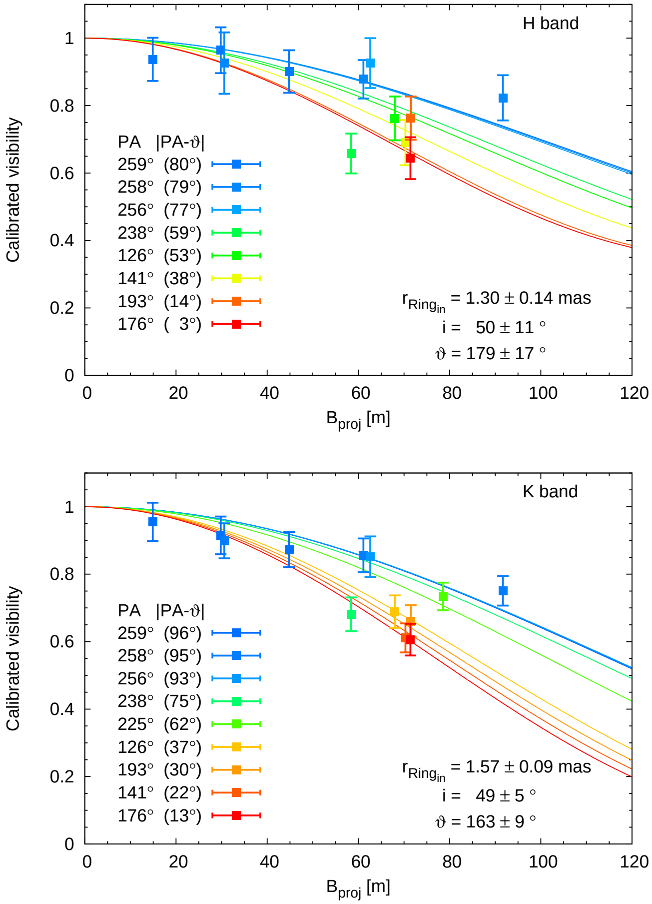

Figure 3.3: Geometric inclined ring-fit models (ring width = 20% of $r_{\text{ring,in}}$) of the H- (top) and K-band (bottom) visibilities. The right plot contains our AMBER data and the KI measurements. The wavelengths are averaged over the whole respective spectral band. The model consists of the unresolved stellar contribution and an inclined ring (see Sect. 3.4.1). We simultaneously fit all visibilities with a two-dimensional visibility model. The model curves are plotted for all position angles for which visibilities were measured. The color sequence (blue to red) describes the decreasing difference between the PA of the measurement and the disk's fitted semi-major axis ϑ.

We first attempted to fit the data with a model consisting of a stellar point source (distance, L_*, and T_* from Table 3.1) and a temperature-gradient disk (model A in Table 3.3). The model has six free parameters: the inner ring radius $r_{\mathrm{in},1}$, the width of the ring $\Delta r_{\mathrm{in},1} = r_{\mathrm{out},1} - r_{\mathrm{in},1}$, the temperature at the inner radius $T_{\mathrm{in},1}$, the power-law index q_1, the inclination i, and the position angle of the semi-major axis of the disk-like object ϑ. The best-fit parameters are listed in Table 3.5. However, no successful fit could be found that is able to reproduce all observations simultaneously ($\chi^2_{\mathrm{red}} = 6.2$).

Therefore, we adopted a two-component model consisting of the star (same parameters as above) and two inclined concentric ring-shaped disks (model B, see Table 3.3 and 3.5). There are ten free model parameters: four for the inner disk ($r_{\mathrm{in},1}$, $\Delta r_{\mathrm{in},1}$, $T_{\mathrm{in},1}$, q_1), four for the outer disk ($r_{\mathrm{in},2}$, $\Delta r_{\mathrm{in},2}$, $T_{\mathrm{in},2}$, q_2), and two for the whole disk system (i, ϑ). We computed all combinations of these parameters within the parameter ranges (and for the described N step values) defined in Table 3.3. We first calculated the models with a rough grid (model B$_1$) and then with finer grids (model B$_2$ and B$_3$) around the χ^2_{red}-minimum of the previous run. In total (for all models described in Table 3.3), we computed ~700 million models.

In our best-fitting model B$_3$ ($\chi^2_{\mathrm{red}} = 2.7$, see Figs. 3.4, 3.5, and 3.6), the inner disk spans from 0.19 ± 0.01 AU to 0.23 ± 0.02 AU (with a temperature of 1257^{+133}_{-53} K at the inner radius $r_{\mathrm{in},1}$) and the outer disk between $1.35^{+0.19}_{-0.20}$ AU and > 4.3 AU (334^{+35}_{-17} K at $r_{\mathrm{in},2}$) with a gap between both components. The very narrow disk width of 0.04 AU makes the inner disk region appear rather ring-like in the NIR (see Fig. 3.6, right). We cannot constrain the temperature gradient q_1 because the inner narrow ring-shaped component is basically emitting only at one uniform temperature $T_{\mathrm{in},1}$. The inclination (angle between the system axis and the viewing direction) is $48.6^{+2.9}_{-3.6}{}^\circ$ and the position angle of the disk is $169.3^{+4.2}_{-6.7}{}^\circ$, which is approximately consistent with our geometric model in Sect. 3.4.1. We emphasize that the structure of the outer disk is a result of the longer wavelength data – that is, the MIDI data and the the MIR/far-infrared (FIR) SED. The inclination and position angle of the system are mainly determined by the NIR interferometric data but consistent with the MIDI data. In the case of temperature-gradient models with more than one component, please note that simultaneous modeling of the visibilities and the SED is able to constrain the inner temperatures ($T_{\mathrm{in},1}$, $T_{\mathrm{in},2}$) of the single components rather than the exact shape of the single temperature gradients (q_1, q_2).

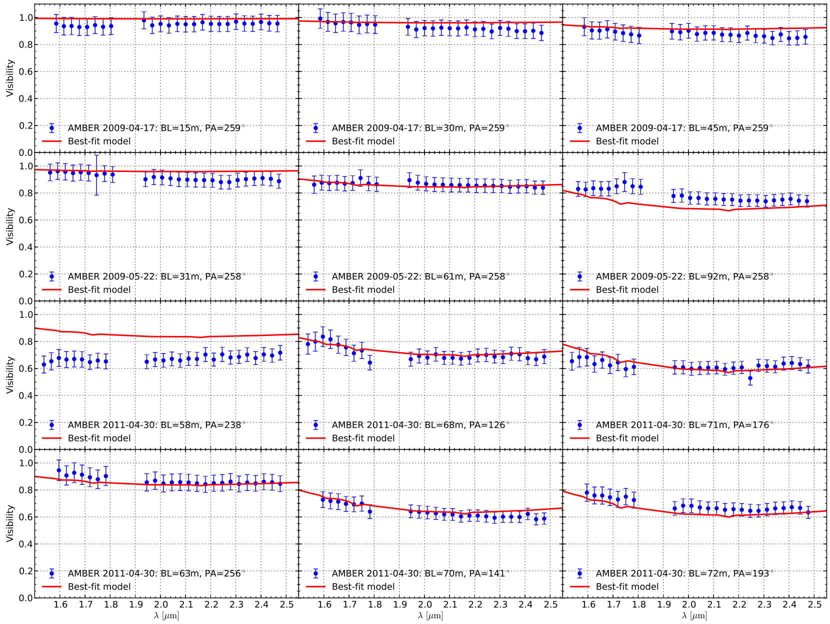

Figure 3.4: AMBER visibilities (see Table 3.2) and temperature-gradient model B_3: The panels show the wavelength-dependent *H* and *K* band visibilities of our AMBER observations. Each panel displays one of the three baselines of each measurement (nights I-IV, cf. Tab. 3.2). The red line indicates the corresponding best-fit temperature-gradient model curves (model B_3 in Table 3.5) in all plots.

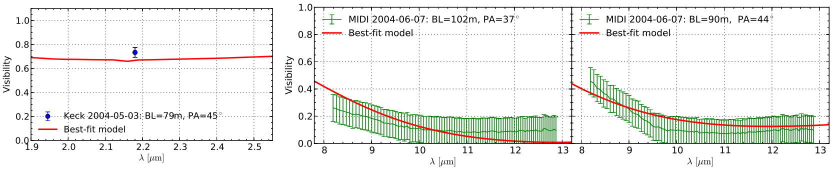

Figure 3.5: Keck and MIDI observations and temperature-gradient model B_3. *Left:* Keck visibility. *Right:* MIDI visibilities.

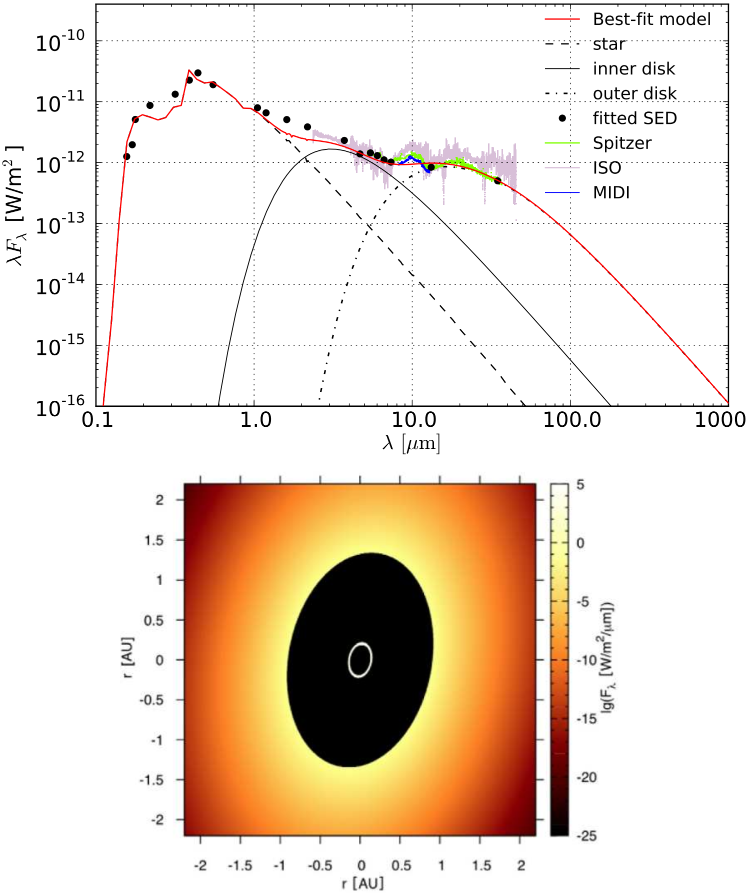

Figure 3.6: *Top:* SED and temperature-gradient model B_3: The SED of V1026 Sco was constructed using published SED observations (black dots). Some of the points represent binned observations; the size of the error bars is on the order of the size of the dots. The resulting fit curve (red) consists of the stellar contribution (Kurucz model, black dashed line), the inner ring (black solid line), and the outer ring model SED (black dash-dotted line). *Bottom:* Two-dimensional intensity distribution of our best-fit model (B_3) at 2 μm. The narrow bright ring is the inner ring-shaped disk in the model. The central star is not shown here. Please note that the intensity scale is logarithmic; the outer disk contributes only insignificantly to the NIR flux. The actual geometry of the outer disk remains poorly constrained because only two MIDI uv points exist.

Table 3.5: Parameters of best-fit temperature-gradient models A & B_3.

Parameter	Best-fit parameters (A)	Best-fit parameters (B_3)
$r_{\mathrm{in},1}$ [AU]	0.06 ± 0.01	0.19 ± 0.01
$r_{\mathrm{out},1}$ [AU]	$4.6^{+1.1}_{-1.6}$	0.23 ± 0.02
$r_{\mathrm{in},2}$ [AU]	...	$1.35^{+0.19}_{-0.20}$
$r_{\mathrm{out},2}$ [AU]	...	> 4.3
$T_{\mathrm{in},1}$ [K]	1937^{+25}_{-61}	1257^{+133}_{-53}
$T_{\mathrm{in},2}$ [K]	...	334^{+35}_{-17}
q_1	0.5	0.5
q_2	...	1.0
i [°]	$86.9^{+0.2}_{-1.7}$	$48.6^{+2.9}_{-3.6}$
ϑ [°]	$139.0^{+0.2}_{-1.7}$	$169.3^{+4.2}_{-6.7}$
χ^2_{red}	6.2	2.7

Notes. The listed parameters for the inner ($j = 1$) and, if included, outer ($j = 2$) ring-shaped disk are as follows: the inner ring radius $r_{\mathrm{in,j}}$, the outer ring radius $r_{\mathrm{out,j}} = r_{\mathrm{in,j}} + \Delta r_{\mathrm{in,j}}$, the temperature at the inner radius $T_{\mathrm{in,j}}$, the power-law index q_j, the inclination i, and the position angle of the semi-major axis ϑ. Parameters without error bars cannot be constrained (see discussion in Sect. 3.5).

3.5 Discussion

To compare the disk size of V1026 Sco with other young stellar objects, we plot the K-band radius (0.18 ± 0.06 AU, see Table 3.4) obtained with a geometric inclined-ring fit into the size-luminosiy diagram (Fig. 3.7). The derived radius is $\sim$1.5 times larger than expected for a dust sublimation temperature of 1500 K and is located approximately on the 1200 K line. Within the error bars, it still agrees with a dust sublimation temperature of 1500 K expected for dust consisting mostly of silicates (Natta et al. 2001; Dullemond et al. 2001; Monnier & Millan-Gabet 2002).

The derived best-fit temperature-gradient model B_3 consists of a two-component disk model; all parameters are listed in Table 3.5. The inner component is a ring-shaped disk with an inner radius of 0.19 ± 0.01 AU and an inner temperature of 1257^{+133}_{-53} K. The outer ring-shaped disk extends from $1.35^{+0.19}_{-0.20}$ AU to > 4.3 AU with 334^{+35}_{-17} K at the inner edge. Between the hot inner and cool outer components, our best-fit model shows an approximately

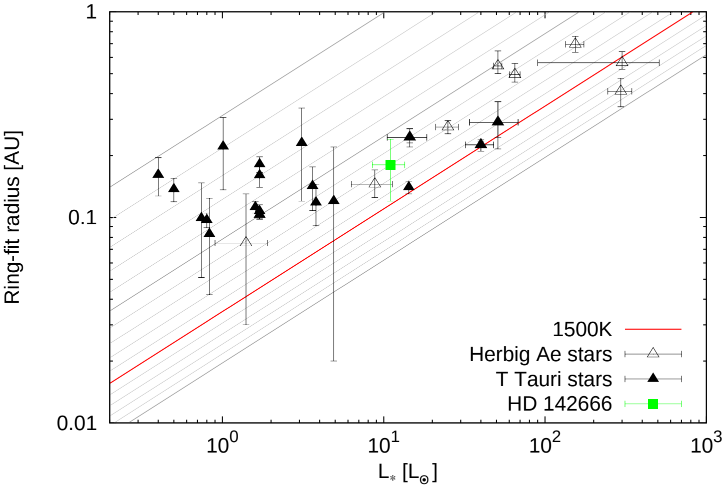

Figure 3.7: Size-luminosity diagram. The K-band ring-fit radius of V1026 Sco (semi-major axis derived with an inclined ring fit in Sect. 3.4.1) is plotted as a green filled square. For comparison, we also plot a sample of Herbig Ae stars (unfilled black triangles, Monnier et al. 2005) and a sample of TTS (filled black triangles, Pinte et al. 2008). The theoretical relation between the ring radius in the NIR and the luminosity (Monnier & Millan-Gabet 2002) is shown for different temperatures. The 1500 K line is plotted in red; the gray lines indicate curves for temperatures between 500 K (highest line) and 2000 K (lowest line) in 100 K steps.

1.1 AU-wide gap. The inclination of $48.6^{+2.9\circ}_{-3.6}$ is similar to the inclination derived with our geometric model in Sect. 3.4.1 (~49°and ~50°) and to the value of 55° found by Dominik et al. (2003). Neither of the power-law indices could be constrained. In the inner component, the ring width is too small to allow us to constrain q_1. In the outer component, there seems to be a degeneracy between q_2 and $r_{\mathrm{out},2}$. The parameters of the inner disk (Table 3.5) are similar to the ones obtained with the geometric fit of the near-infrared visibilities (Table 3.4) and the size-luminosity diagram (Fig. 3.7). A possible explanation for the lack of FIR emission in the SED of some HAeBes and the apparent disk gap is self-shadowing by the puffed-up inner rim (Dullemond & Dominik

2004).

The stellar rotation of V1026 Sco is $v \sin i = 65.3 \pm 3.1$ km s^{-1} (Alecian et al. 2013a), leading to a maximum rotational velocity of ~86 km s^{-1} if the inclination of the star is comparable to the disk inclination. This is similar (Boehm & Catala 1995) or slightly lower (Alecian et al. 2013b) than the average velocity of low-mass Herbig Ae/Be stars but higher than measurements of T Tauri stars (Weise et al. 2010).

Magnetic braking can reduce the rotational velocity as observed in T Tauri stars (Koenigl 1991; Weise et al. 2010; Johnstone et al. 2013). In Herbig stars, strong magnetic braking is less likely than in T Tauri stars because the observed magnetic fields are weaker. In V1026 Sco, a magnetic field has not been detected (Alecian et al. 2013a), which could mean that it is weak, as expected for Herbig Ae stars (Weise et al. 2010). Even if a magnetic field exists, but could not be detected, the high value of the stellar rotation velocity of V1026 Sco suggests that rotational braking via disk locking (Koenigl 1991; Stępień 2000) is much weaker than in T Tauri stars.

Our findings can be described with the standard disk theories for Herbig Ae stars, which postulate passive circumstellar disks with inner holes and puffed-up inner rims (Natta et al. 2001; Dullemond et al. 2001). In addition, the derived inclination might be large enough to explain the UXOr variability of V1026 Sco in the context of current proposed theories, as we discuss in the following. Theories about partial obscuration of the stellar light by hydrodynamic fluctuations of the inner rim need high inclination angles for explaining the UXOr variability (Dullemond et al. 2003). With the measured intermediate inclination of V1026 Sco, the rim fluctuations would have to be twice as high as the theoretical fluctuation height. Therefore, this model is less suitable in our case and also for several other UXOrs (e.g. Pontoppidan et al. 2007). The unsteady accretion model by Herbst & Shevchenko (1999) is inclination independent and cannot be disproven with our measurements. For intermediate to high disk inclinations, orbiting dust clouds might intercept the line of sight toward the star (Grinin et al. 1994; Natta et al. 1997). For this case, the derived inclination of V1026 Sco is still within the range predicted for UXOrs (45°–68°) by Natta & Whitney (2000). Dust clouds in centrifugally-driven disk winds (Vinković & Jurkić 2007; Bans & Königl 2012) can also explain the UX Ori type variability of V1026 Sco, as they also are consistent with intermediate to high disk inclinations.

3.6 Conclusion

We observed the UX Ori star V1026 Sco with VLTI/AMBER in the *H* and *K* bands. With a geometric ring-shaped model consisting of the star and an inclined ring, we found a radius of $r_{\text{ring,in}} = 0.18 \pm 0.06$ AU in the *K* band. In the context of the size-luminosity diagram, this radius is found to be consistent with the theory of a passive circumstellar disk with an inner hole and a rim at the dust sublimation radius. We further derived an inclination of $50 \pm 11°$ and $49 \pm 5°$ and a PA of the semi-major axis of the inclined disk of $179 \pm 17°$ and $163 \pm 9°$ in the *H* and *K* bands, respectively.

We found a two-component-disk temperature-gradient model that is able to reproduce all visibilities and the SED. The inner radius of the inner disk is 0.19 ± 0.01 AU and similar to the one found with a geometric ring fit. The two disk components are separated by a gap, which may be explained by a shadow cast by a puffed-up inner rim and agrees with the type II classification of the object. The derived inclination of $48.6^{+2.9}_{-3.6}{}^{\circ}$ and the PA of $169.3^{+4.2}_{-6.7}{}^{\circ}$ are consistent with the values found by geometric modeling. Our inclination of $\sim 49°$ is probably not consistent with a model where rim fluctuations cause the UXOr variability, because the expected rim height is not high enough, as discussed above. The unsteady accretion theory cannot be excluded with our measurements, because the model is inclination-independent. Finally, the measured intermediate disk inclination is within the range predicted from UXOr models with orbiting dust clouds in the disk or in centrifugally-driven disk winds.

4 Study of the sub-AU disk of the Herbig B[e] star HD 85567 with near-infrared interferometry

This chapter is based on the publication Vural et al. (2014a), which used observations made with ESO telescopes at the La Silla Paranal Observatory under programme IDs 080.C-0541(C), 082.C-0893(A), 084.C-0848(B).

4.1 Abstract

The structure of the inner disk of Herbig Be stars is not well understood. The continuum disks of several Herbig Be stars have inner radii that are smaller than predicted by models of irradiated disks with optically thin holes.

We study the size of the inner disk of the Herbig B[e] star HD 85567 and compare the model radii with the radius suggested by the size-luminosity relation.

The object was observed with the AMBER instrument of the Very Large Telescope Interferometer. We obtained K-band visibilities and closure phases. These measurements are interpreted with geometric models and temperature-gradient models.

Using several types of geometric star-disk and star-disk-halo models, we derived inner ring-fit radii in the K band that are in the range of 0.8–1.6 AU. Additional temperature-gradient modeling resulted in an extended disk with an inner radius of $0.67^{+0.51}_{-0.21}$ AU, a high inner temperature of 2200^{+750}_{-350} K, and a disk inclination of $53^{+15}_{-11}{}^\circ$.

The derived geometric ring-fit radii are approximately 3–5 times smaller than that predicted by the size-luminosity relation. The small geometric and temperature-gradient radii suggest optically thick gaseous material that absorbs stellar radiation inside the dust disk.

4.2 Introduction

Infrared interferometric observations suggest that the circumstellar environment of Herbig Be (HBe) and Herbig Ae (HAe) stars are significantly different. In contrast to the lower-mass HAe stars, the K-band continuum radii of several HBe stars are significantly smaller than predicted by the size-luminosity relation (Monnier et al. 2005; Eisner et al. 2004; Kraus et al. 2008b; Weigelt et al. 2011; Kreplin et al. 2012). These smaller radii can be explained by the presence of an optically thick gas inside the dust disk. This optically thick gas can absorb the stellar ultraviolet (UV) radiation and allows dust to exist closer to the star (Monnier & Millan-Gabet 2002).

The object HD 85567 (V596 Car, Hen 3-331) is a B-type star at a distance of 1.5 ± 0.5 kpc (see stellar parameters in Table 4.1). The evolutionary status of HD 85567 is not yet well-established. Miroshnichenko et al. (2001) suggested the object to be a main-sequence B[e] star. Other studies reported that HD 85567 is a young stellar object (Lamers et al. 1998; Malfait et al. 1998; Verhoeff et al. 2012; Wheelwright et al. 2013). Miroshnichenko et al. (2001) proposed the existence of a close binary companion that can interact with the circumstellar disk of HD 85567. Binarity is believed to be a key property in B[e] stars (Miroshnichenko 2007). Baines et al. (2006) detected a binary companion with a separation of $\gtrsim 500$ mas.

We use our near-infrared (NIR) interferometric observations to investigate the inner disk structure of HD 85567. The paper is organized as follows. We describe the observations and the data reduction in Sect. 4.3. The modeling is presented in Sect. 4.4 and the results are discussed in Sect. 4.5.

4.3 Observation and data reduction

The observations of HD 85567 were carried out using the near-infrared three-beam combiner VLTI/AMBER (Petrov et al. 2007) in three different nights. We obtained a total of six measurements in the low spectral resolution mode ($R = 30$: Fig. 4.1, Table 4.2). The data were reduced with *amdlib 3.0.5*[*] (Tatulli et al. 2007; Chelli et al. 2009). We applied a signal-to-noise frame selection (20% of the highest fringe signal-to-noise ratio (SNR); Tatulli et al. 2007) to

---

[*] `http://www.jmmc.fr/data_processing_amber.htm`

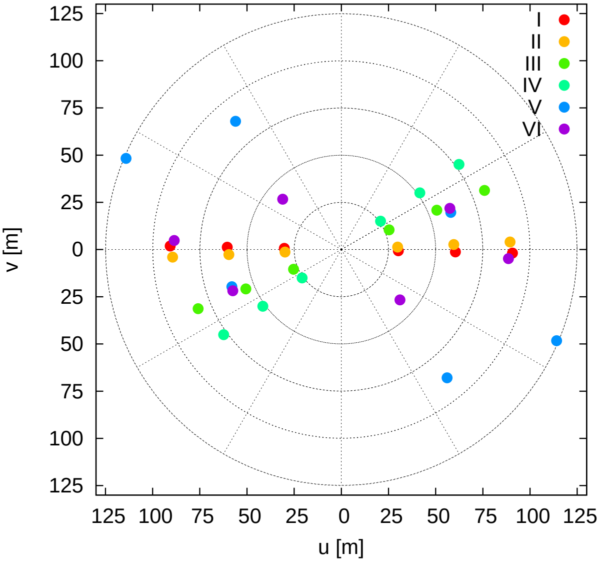

Figure 4.1: The *uv* coverage of our AMBER measurements of HD 85567 (see Table 4.2).

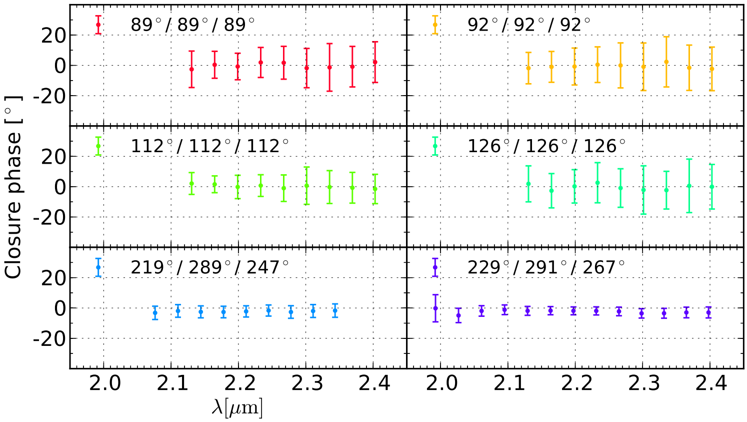

Figure 4.2: Derived closure phases. The color coding is the same as in Fig. 4.1.

Table 4.1: Stellar parameters of HD 85567.

Parameter	Value
spectral type	B2V $^{(a)}$
distance [kpc]	1.5 ± 0.5 $^{(a)}$
$M_*[M_\odot]$	12 ± 2 $^{(b)}$
$\log(T_*[\mathrm{K}])$	4.32 ± 0.08 $^{(b)}$
$\log(L_*[L_\odot])$	4.17 ± 0.16 $^{(b)}$
$R_*[R_\odot]$	9 ± 2 $^{(b)}$
A_V	1.1 ± 0.1 $^{(b)}$
$\dot{M}[10^{-6} M_\odot \mathrm{yr}^{-1}]$	6.3^{+4}_{-2} $^{(c)}$

Notes. References: (a)Miroshnichenko et al. (2001), (b)Verhoeff et al. (2012), (b)Ilee (2013).

the raw files of object and calibrator to obtain an improved visibility calibration. An additional improvement of the visibility calibration was achieved by equalizing the optical path difference (OPD) histograms of the object and calibrator (Kreplin et al. 2012) to account for atmospheric OPD drifts.

We derived K-band closure phases (Fig. 4.2) and visibilities (Fig. 4.5). The closure phases are zero within the error bars, indicating that the brightness distribution of our source is centrosymmetric. Except in measurement VI, *amdlib 3.0.5* did not compute visibilities and closure phases for wavelengths in the range of approximately 2.0 – 2.1 μm because of low SNR. The SNR of the H-band data was also too low to derive H-band visibilities and closure phases.

The spectral energy distribution (SED; see Fig. 4.3) was reconstructed from dereddened values found in the literature (Verhoeff et al. 2012) and data from the Spitzer Space Telescope (IRS, program ID: 3470).

4.4 Modeling

4.4.1 Geometric modeling

The NIR emission of Herbig stars is believed to originate mainly in a ring-like region at the inner edge of the disk, which is often associated with a puffed-up inner rim (Natta et al. 2001; Dullemond et al. 2001). Thus, the size of the NIR emission region is often approximated with a geometric ring model, and

Table 4.2: AMBER observation log.

#	Night	Configuration	B_{proj} [m]	PA [°]	Seeing [″]	DIT [ms]	Calibrator	Calibrator diameter [mas]
I	2008-02-22	A0-D0-H0	60/91/30	89/89/89	0.65	21	HD 50281	1.0 ± 0.1 [(a)]
II	2008-02-22	A0-D0-H0	60/91/30	92/92/92	0.72	100	HD 85313	0.451 ± 0.045 [(b)]
III	2008-02-22	A0-D0-H0	55/82/27	112/112/112	0.69	100	HD 85313	0.451 ± 0.045 [(b)]
IV	2008-02-22	A0-D0-H0	51/77/26	126/126/126	0.57	100	HD 85313	0.451 ± 0.045 [(b)]
V	2008-12-14	U1-U3-U4	88/61/124	219/289/247	-	26	HD 50277	0.356 ± 0.036 [(b)]
VI	2009-12-31	U2-U3-U4	41/62/89	229/291/267	1.1	21	HD 85313	0.451 ± 0.045 [(b)]

Notes. The resulting *uv* coverage is shown in Fig. 4.1. B_{proj} describes the projected baseline length, PA the position angles of the baselines, and DIT the detector integration time. References: [(a)]Pasinetti Fracassini et al. (2001), [(b)]Lafrasse et al. (2010). We assumed the calibrator diameter error to be 10%.

Table 4.3: Overview of the geometric models.

Model	R_{in} [AU]	R_{min} [AU]	i °	ϑ °	f_{halo}	χ^2_{red}
Ring	1.08 ± 0.38	1.08 ± 0.38	...	...	...	2.69
Ring + extended halo	0.78 ± 0.31	0.78 ± 0.31	...	...	0.09 ± 0.01	0.39
Elongated ring	1.55 ± 0.53	0.53 ± 0.20	70.0 ± 0.01	155.7 ± 2.1	...	1.88
Elong. ring + extended halo	1.07 ± 0.43	0.60 ± 0.32	55.8 ± 0.09	162.2 ± 5.5	0.09 ± 0.01	0.74

Notes. All models consist of the above ring-like disks, halos, and an unresolved stellar source. The distance uncertainty (Table 4.1) is taken into account in the above uncertainties for the radii. The radii R_{in} and R_{min} are the semi-major and the semi-minor axis of the ring models, respectively. The variable ϑ is the position angle of the semi-major axis.

the ring-fit radius can be compared to theoretical predictions (Millan-Gabet et al. 2001; Monnier & Millan-Gabet 2002; Eisner et al. 2003; Dullemond & Monnier 2010).

Here, we apply several different ring models, all containing an unresolved stellar component and a ring with a width of 20% of the inner ring radius (Monnier et al. 2005). We also investigate inclination effects (i.e., elongated rings) and the influence of an extended halo (see Table 4.3).

The variables of the two-dimensional total visibility $|V| = |V(PA, \nu_{uv})|$ are the position angle (PA) of the measurement and the spatial frequency $\nu_{uv} = B_{proj}/\lambda$ (see Table 4.2). It can be described by

$$|V| = |(1 - f_* - f_{halo})V_{ring} + f_* V_* + f_{halo} V_{halo}| \; , \tag{4.1}$$

where $V_* = 1$ is the visibility of the star, V_{ring} is the visibility of the ring-shaped disk, V_{halo} is the visibility of the halo, f_{halo} is the flux contribution of the halo, and $1 - f_* - f_{halo}$ is the flux contribution of the ring-like disk. The wavelength-dependent relative flux contribution f_* of the stellar component to the total emission was derived from the SED (Fig. 4.3). The model parameters are the inner ring radius R_{in} (semi-major axis in the elongated case) of the extended ring, the inclination i, the position angle ϑ of the semi-major axis of the elongated ring, and f_{halo}. An overview of our fit models, their parameters, and the resulting χ^2_{red} are presented in Table 4.3. We obtain inner radii between 0.78 AU (~0.5 mas) and 1.55 AU (~1.0 mas) and inclination angles in the range of ~56° to ~70°. The large error bars of the NIR visibilities do not allow us to make a definite decision on the elongation and the orientation of the disk as models without elongation fit the data as well (see Table 4.3).

4.4.2 Temperature-gradient model

To interpret our data, we model our visibility measurements and the literature SED of HD 85567 with a temperature-gradient model. This kind of modeling has already been used for modeling AMBER data from young stars of different types by, for example, Malbet et al. (2005), Kraus et al. (2010, 2012), Kreplin et al. (2012), Chen et al. (2012), and Vural et al. (2014b).

The temperature distribution $T(r)$ of a circumstellar disk is assumed to be: $T(r) = T_{in} \cdot (r/r_{in})^{-q}$, where r is the radius, q is the temperature power-law index, and T_{in} the temperature at the inner disk radius r_{in}. The disk is modeled as the sum of a large number of narrow rings; each has a temperature $T(r)$. We integrate the blackbody spectra of the rings and the intensity distribution of these rings to obtain the total energy distribution and the visibilities. We allow the model disk to be inclined, thus introducing the inclination i ($i = 0°$ if the disk is face-on) and the position angle ϑ (measured east of north) of the semi-major axis of the model disk as additional parameters.

Our model includes a stellar component with the parameters from Table 4.1 (distance, T_*, R_*, and L_*) and a surrounding circumstellar temperature-gradient disk extending to an outer radius of $r_{\text{out}} = r_{\text{in}} + \Delta r$. Each computed model contains the visibilities for all baseline-position angle combinations in our measurements. We calculated the models for all combinations of the parameter values as described in Table 4.4, where each parameter was varied in 4 to 40 steps within the described scan ranges. This method required the calculation of approximately 170 million models.

To find the best-fit temperature-gradient model, we calculated the χ^2_{red} (using $\chi^2 = \chi^2_{\text{SED}} + \chi^2_{\text{Vis}}$) of each model and obtained a best-fit model with $\chi^2_{\text{red}} \sim 1.0$ (see Fig. 4.7 in the Appendix). The parameters of the best-fit model are listed in Table 4.4 and will be discussed in the following section. The uncertainties are 3σ errors. The model curves are shown in Figs. 4.3 and 4.5.

Table 4.4: Scanned parameter space and best-fit temperature-gradient model described in Sect. 4.4.2.

Parameter	Scan range	N_{val}	Best-fit value
r_{in} [AU]	0.04 – 10	40	$0.67^{+0.51}_{-0.15}$
Δr [AU]	0.01 – 50	30	$24.8^{+20.5}_{-8.8}$
T_{in} [K]	200 – 8000	40	2200^{+752}_{-341}
q	0.2, 0.5, 0.75, 1.0	4	0.75
i [°]	0 – 90	30	$52.6^{+14.7}_{-11.0}$
ϑ [°]	0 – 170	30	$121.4^{30.6+}_{-46.8}$

Notes. N_{val} is the number of parameter values used. The spacing between the single parameter values is linear or as indicated, except for r_{in}, where the spacing is logarithmic. For example, the parameter values for r_{in} are 0.10 AU, 0.11 AU, 0.13 AU, ..., 10 AU.

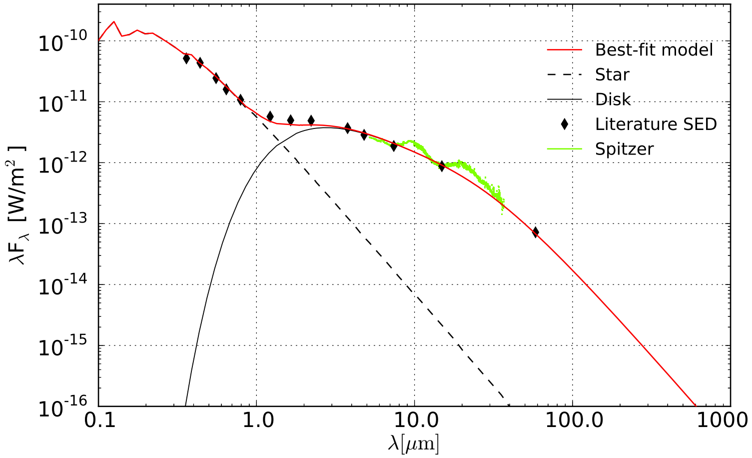

Figure 4.3: Observed SED (black diamonds) and SED of the best-fit temperature-gradient model (Table 4.4). The total SED (red line) consists of the stellar flux (Kurucz model, black dashed line) and the flux of the temperature-gradient disk (black solid line).

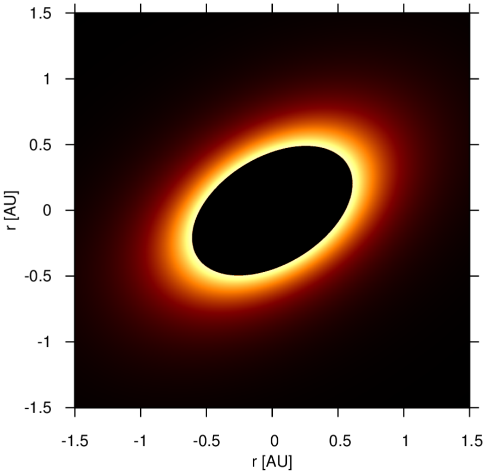

Figure 4.4: Two-dimensional intensity distribution of the best-fit model at 2 μm. The color-scaling is linear in arbitrary units. The star is not displayed.

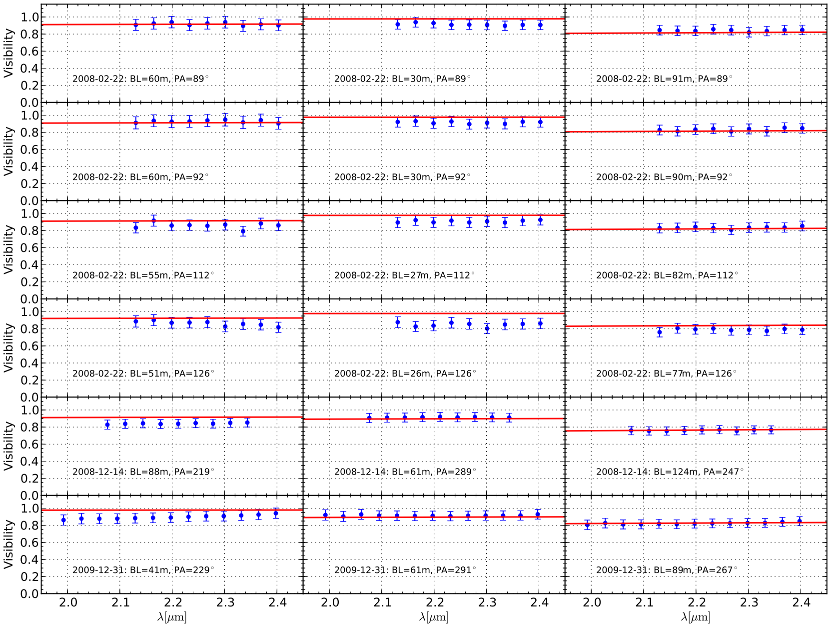

Figure 4.5: Comparison of the visibilities of the best-fit temperature-gradient model (red line; see Table 4.4) with the wavelength-dependent AMBER visibilities (blue dots). The wavelength range of the visibilities is different for all measurements because of different data quality as explained in Sect. 4.3.

4.5 Discussion

From our geometric modeling, we obtained different ring-fit radii for different star-disk and star-disk-halo models (see Table 4.3). We achieve significantly better χ^2_{red} if the model has a halo component. The χ^2_{red} closest to one was obtained for the geometric ring model of an elongated ring and a halo. The inner ring radius of this model is $R_{\mathrm{in}} \sim 1.1 \pm 0.4$ AU. Wheelwright et al. (2013) estimated the ring radius with a symmetric star-ring model including resolved background emission to 0.8 ± 0.3 AU. This value is consistent with most of our derived ring-fit radii (Table 4.3). The high visibility values and small closures phases (which are approximately zero; see Fig. 4.2) of our observations and of the observations reported by Wheelwright et al. (2013) do not allow us to detect any binary signature. Binarity is believed to be a key property in B[e] stars (Miroshnichenko 2007).

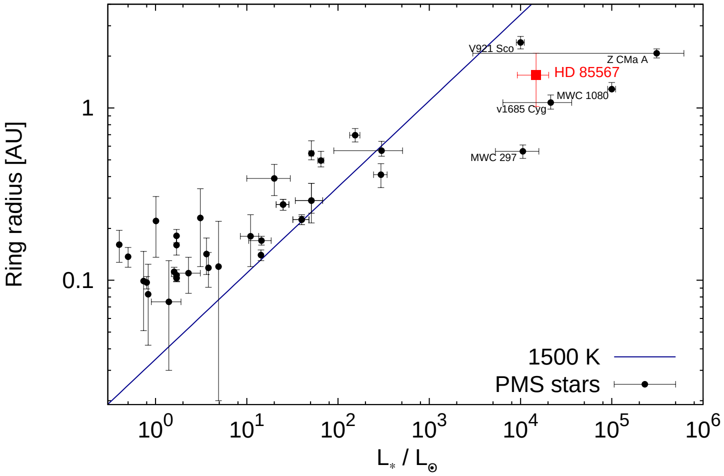

Figure 4.6: The position of HD 85567 (red square) in the size-luminosity diagram of T Tauri stars, Herbig Ae, and Herbig Be stars. The data are taken from the literature (Eisner et al. 2004; Monnier et al. 2005; Kraus et al. 2008a; Pinte et al. 2008; Weigelt et al. 2011; Chen et al. 2012; Kreplin et al. 2012; Vural et al. 2012; Wang et al. 2012; Kreplin et al. 2013; Vural et al. 2014b). The solid line shows the theoretical dependence of the inner ring radius on the luminosity for an optically thin disk hole and a dust sublimation temperature of 1500 K (Monnier et al. 2005).

Our geometric ring-fit radii (~0.8 – 1.6 AU) are approximately 3 – 5 times smaller than the radii predicted by the size-luminosity relation (~4.2 AU; Fig. 4.6). The predicted radii of the size-luminosity relation (Monnier et al. 2005) are based on the assumption that the dust sublimates at a temperature of 1500 K and the inner cavity is dust-free and optically thin. These assumptions are approximately valid for HAe stars. However, several interferometric observations suggest that some of the more massive HBe stars harbor a gaseous, optically thick disk inside the dust disk. This gas disk can partially shield the stellar radiation, thereby letting dust survive closer to the star (Monnier & Millan-Gabet 2002; Monnier et al. 2005; Millan-Gabet et al. 2007; Weigelt et al. 2011).

Our best-fit temperature-gradient model (Table 4.4, Figs. 4.3, 4.4, 4.5) consists of the stellar point source and an extended disk with an inner radius of $r_{\mathrm{in}} = 0.67^{+0.51}_{-0.21}$ AU. This inner radius is approximately 1.6 to 2.3 times smaller than the elongated ring-fit radii derived with geometric modeling (Table 4.3) but also corresponds to a higher temperature. We derived a disk inclination of $i = 52.6^{+14.7\circ}_{-11.0}$ and a position angle of the disk semi-major axis of $\vartheta = 121.4^{30.6+\circ}_{-46.8}$, which are similar to the values derived with geometric modeling, but not very well constrained due to the large error bars of the NIR visibilities (cf. Fig. 4.7 in the Appendix). The derived inner temperature $T_{\mathrm{in}} = 2200^{+752}_{-341}$ K is too hot for the standard dust composition consisting mainly of silicates, but the existence of refractory dust grains (e.g., iron, graphite, corundum; Benisty et al. 2010) may explain this high temperature. Gas emission inside the dust disk can also contribute to the K-band visibility and make the average NIR radius appear smaller (e.g., Kraus et al. 2008b). A size estimate based on the accretion rate supports the presence of an optically thick inner disk (Wheelwright et al. 2013). By modeling the CO bandhead emission, these authors found that a compact (inner radius approximately 0.2–1 AU), optically thick gas disk can reproduce their measurements. This agrees with the hypothesis of shielded stellar radiation, which leads to small dust sublimation radii, which agrees with our observations.

4.6 Conclusion

We used geometric and temperature-gradient models to interpret our VLTI/AMBER data and the SED of the Herbig B[e] star HD 85567. We derived geometric ring models with inner radii of 0.8–1.6 AU, which are approximately 3–5 times smaller than that predicted by the size-luminosity relation. Using temperature-gradient modeling, we found a hot ($T_{\mathrm{in}} \sim 2200$ K) inner disk rim with a small ($r_{\mathrm{in}} \sim 0.67$ AU) inner radius. The undersized inner disk radius obtained with both geometric and temperature-gradient modeling agrees with measurements of several other HBe stars and with previous measurements of this object. The small inner radius provides further support to the existence of an optically thick gaseous inner disk shielding the stellar radiation in Herbig Be stars.

4.7 Appendix

4.7.1 χ^2-maps

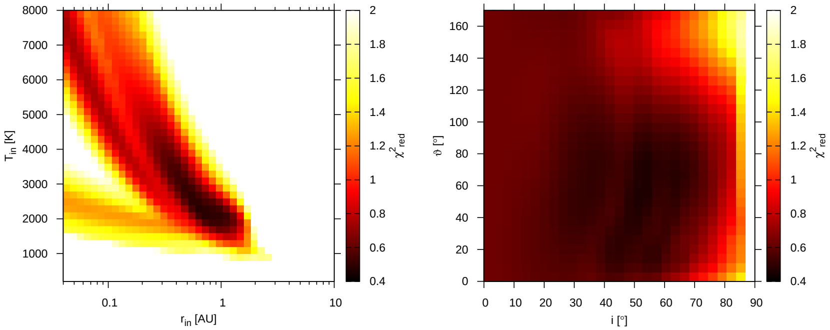

Figure 4.7: Two-dimensional χ^2_{red} distributions of selected parameters of the temperature-gradient model.

5 Thesis summary and outlook

5.1 Summary

In this thesis, I studied the inner circumstellar disks of three pre-main sequence stars of different spectral types and masses. The focus lay on determining the size and the shape of the near-infrared emitting region in circumstellar disks, which is often associated to the dust-sublimation radius.

The bulk of the data used in this work was taken with the Very Large Telescope Interferometer, hereby using the near-infrared three-beam combiner VLTI/AMBER and the mid-infrared two-beam combiner VLTI/MIDI. In addition, literature data for reconstructing the spectral energy distribution was gathered.

In Chapter 2, a study of the T Tauri star S CrA N has been presented. The star was observed in two nights with VLTI/AMBER. In addition, archival VLTI/MIDI data (two configurations) was taken into account. The circumstellar disk can be described by a face-on two-component disk. The inner component is a thin ring with an inner temperature that is close to the dust sublimation temperature. We therefore suspect this component to be created by a hot, maybe even puffed-up, inner rim like proposed for Herbig Ae/Be stars. The geometric ring radius was found to be larger than expected. Nevertheless, models including disk backwarming predict the inner radius of the dust disk to be approximately as large as the geometric models indicate.

The Herbig Ae star V1026 Sco (Chapter 3) is suspected to be a member of the UX Ori class. We analyzed measurements of four VLTI/AMBER and two VLTI/MIDI configurations, and in addition, one literature measurement of the Keck Interferometer. The data can be described with a two-component model, where the outer, more extended disk is separated by an apparent gap from the inner, very thin ring component. This structure can be interpreted in the context of self-shadowed disk models: Here, the tentative puffed-up inner rim shields the stellar radiation and casts a shadow over part of the outer disk. The found inclination of around 50° supports (among the inclination-dependent models) a picture of UX Ori stars where the line of sight is recurrently intercepted by orbiting dust clouds in the disk itself or in disk winds. The geometric inner disk radius matches the predictions for an inner rim at the dust-sublimation radius with an optically thin inner cavity.

The high-mass Herbig Be star HD 85567 (Chapter 4) was observed with six different configurations of VLTI/AMBER. The circumstellar dust disk of the object was found to have a significantly smaller radius than that predicted for a disk with an optically thin cavity. It can be assumed that the disk region inside of the observed dust-sublimation radius is optically thick and shields part of the stellar radiation, allowing the dust to stay closer to the star before evaporating. The data can be modeled with inclined disk models, but the rather large error bars do not allow a definite decision on the elongation of the object.

The studies of the three pre-main sequence stars show how much the inner circumstellar disk structure depends on the properties of the central star, especially on the luminosity. The general picture of a disk that consists of a dusty and a mostly dust-free region seems to be valid for a large stellar mass range. However, the optical thickness of the innermost dust-free disk, the influence of the inner rim of the dusty disk, and the behaviour of the outer disk regions can cause significant differences between the circumstellar disks of PMS stars of different types.

5.2 Outlook

The studies presented in this work show the practicability of infrared interferometry for spatially resolving the inner regions of circumstellar disks on AU and sub-AU scales. With only a very sparse *uv*-coverage, it was possible to characterize the near- and partially mid-infrared emission regions of three different pre-main sequence stars and set the results into the context of the big picture of the inner disk structure.

Nevertheless, it would be desirable to refine the results for the studied objects by measuring at more points in the *uv* plane and possibly reconstructing images. This can be achieved by combining the light of more telescopes, which is the goal of the next generation of VLTI instruments.

In the near future (2016/2017), the mid-infrared (L, M, N bands) four-beam combiner VLTI/MATISSE (Multi-AperTure mid-Infrared SpectroScopic Experiment; Lopez et al. 2006; Lagarde et al. 2012) will allow to sample a larger part of the *uv* plane than VLTI/MIDI with one measurement (six *uv* points, four closure phases). With model-independent image reconstruction, it will be possible to derive the radial and vertical disk structure in more detail and to find planet signatures. The anticipated spectral resolution will be able to trace dust and gas lines in more detail.

Since shortly, the visitor instrument PIONIER (Precision Integrated-Optics Near-infrared Imaging ExpeRiment; Le Bouquin et al. 2011) can also be used by the community. It is a four-beam combiner as MATISSE, but operates in the near-infrared (H band). It can be operated in low-spectral resolution or broadband and can help to refine the spatial distribution of the inner circumstellar matter.

GRAVITY (General Relativity Analysis via VLT InTerferometrY; Eisenhauer et al. 2005) will be a four-beam combiner in the near-infrared (K band), anticipated for 2015 for the VLTI [*]. It aims at resolving small structures in circumstellar disks and jets with milli-arcsecond resolution.

By combining the results of the above-mentioned instruments for a large number of young stars, it will be possible to characterize the star and planet formation processes in even more detail.

Figure 5.1: Paranal observatory at night. [Credit: ESO/G.Hüdepohl]

---

[*] `http://www.mpe.mpg.de/ir/gravity`

A Units and natural constants

Table A.1: Units and natural constants used in this work.

Name	Symbol	Value	Unit
Astronomical unit	AU	$1.496 \cdot 10^{11}$	m
Milli-arcsecond	mas	$4.848 \cdot 10^{-9}$	rad
Parsec	pc ($\sim \frac{1\mathrm{AU}}{1\mathrm{mas}}$)	$3.086 \cdot 10^{16}$	m
Solar mass	$M_\odot$	$1.988 \cdot 10^{30}$	kg
Solar luminosity	$L_\odot$	$3.845 \cdot 10^{26}$	W
Solar radius	$R_\odot$	$6.963 \cdot 10^{8}$	m
Speed of light	c	$2.998 \cdot 10^{8}$	$\mathrm{m\,s^{-1}}$
Gravitational constant	G	$6.674 \cdot 10^{-11}$	$\mathrm{m^3kg^{-1}s^{-2}}$
Boltzmann constant	k_B	$1.381 \cdot 10^{-23}$	$\mathrm{J\,K^{-1}}$
Stefan-Boltzmann constant	σ	$5.670 \cdot 10^{-8}$	$\mathrm{Wm^{-2}K^{-4}}$

B List of Figures

C List of Tables

D Bibliography

Akeson, R. L., Boden, A. F., Monnier, J. D., Millan-Gabet, R., Beichman, C., Beletic, J., Calvet, N., Hartmann, L., Hillenbrand, L., Koresko, C., Sargent, A., and Tannirkulam, A.: 2005a, *ApJ* **635**, 1173

Akeson, R. L., Walker, C. H., Wood, K., Eisner, J. A., Scire, E., Penprase, B., Ciardi, D. R., van Belle, G. T., Whitney, B., and Bjorkman, J. E.: 2005b, *ApJ* **622**, 440

Alecian, E., Wade, G. A., Catala, C., Grunhut, J. H., Landstreet, J. D., Bagnulo, S., Böhm, T., Folsom, C. P., Marsden, S., and Waite, I.: 2013a, *MNRAS* **429**, 1001

Alecian, E., Wade, G. A., Catala, C., Grunhut, J. H., Landstreet, J. D., Böhm, T., Folsom, C. P., and Marsden, S.: 2013b, *MNRAS* **429**, 1027

Andre, P., Ward-Thompson, D., and Barsony, M.: 1993, *ApJ* **406**, 122

Andre, P., Ward-Thompson, D., and Barsony, M.: 2000, *Protostars and Planets IV* p. 59

Andrews, S. M., Wilner, D. J., Hughes, A. M., Qi, C., and Dullemond, C. P.: 2009, *ApJ* **700**, 1502

Armitage, P. J.: 2011, *ARA&A* **49**, 195

Baines, D., Oudmaijer, R. D., Porter, J. M., and Pozzo, M.: 2006, *MNRAS* **367**, 737

Bans, A. and Königl, A.: 2012, *ApJ* **758**, 100

Benisty, M., Natta, A., Isella, A., Berger, J.-P., Massi, F., Le Bouquin, J.-B., Mérand, A., Duvert, G., Kraus, S., Malbet, F., Olofsson, J., Robbe-Dubois, S., Testi, L., Vannier, M., and Weigelt, G.: 2010, *A&A* **511**, A74

Berger, J. P. and Segransan, D.: 2007, *New Astronomy Review* **51**, 576

Boehm, T. and Catala, C.: 1995, *A&A* **301**, 155

Bonsack, W. K.: 1961, *ApJ* **133**, 340

Bordé, P., Coudé du Foresto, V., Chagnon, G., and Perrin, G.: 2002, *A&A* **393**, 183

Born, M. and Wolf, E.: 1999, *Principles of optics : electromagnetic theory of propagation, interference and diffraction of light*

Bouvier, J., Alencar, S. H. P., Harries, T. J., Johns-Krull, C. M., and Romanova, M. M.: 2007, *Protostars and Planets V* pp 479–494

Calvet, N., Hartmann, L., Kenyon, S. J., and Whitney, B. A.: 1994, *ApJ* **434**, 330

Carmona, A., van den Ancker, M. E., and Henning, T.: 2007, *A&A* **464**, 687

Chelli, A., Utrera, O. H., and Duvert, G.: 2009, *A&A* **502**, 705

Chen, L., Kreplin, A., Wang, Y., Weigelt, G., Hofmann, K.-H., Kraus, S., Schertl, D., Lagarde, S., Natta, A., Petrov, R., Robbe-Dubois, S., and Tatulli, E.: 2012, *A&A* **541**, A104

Chiang, E. I. and Goldreich, P.: 1997, *ApJ* **490**, 368

Cieza, L. A., Kessler-Silacci, J. E., Jaffe, D. T., Harvey, P. M., and Evans, II, N. J.: 2005, *ApJ* **635**, 422

Cieza, L. A., Padgett, D. L., Allen, L. E., McCabe, C. E., Brooke, T. Y., Carey, S. J., Chapman, N. L., Fukagawa, M., Huard, T. L., Noriga-Crespo, A., Peterson, D. E., and Rebull, L. M.: 2009, *ApJ* **696**, L84

Clarke, C. J., Gendrin, A., and Sotomayor, M.: 2001, *MNRAS* **328**, 485

Dominik, C., Dullemond, C. P., Waters, L. B. F. M., and Walch, S.: 2003, *A&A* **398**, 607

Dullemond, C. P. and Dominik, C.: 2004, *A&A* **417**, 159

Dullemond, C. P. and Dominik, C.: 2005, *A&A* **434**, 971

Dullemond, C. P. and Dominik, C.: 2008, *A&A* **487**, 205

Dullemond, C. P., Dominik, C., and Natta, A.: 2001, *ApJ* **560**, 957

Dullemond, C. P. and Monnier, J. D.: 2010, *ARA&A* **48**, 205

Dullemond, C. P., van den Ancker, M. E., Acke, B., and van Boekel, R.: 2003, *ApJ* **594**, L47

Eisenhauer, F., Perrin, G., Rabien, S., Eckart, A., Lena, P., Genzel, R., Abuter, R., and Paumard, T.: 2005, *Astronomische Nachrichten* **326**, 561

Eisner, J. A., Chiang, E. I., Lane, B. F., and Akeson, R. L.: 2007a, *ApJ* **657**, 347

Eisner, J. A., Hillenbrand, L. A., White, R. J., Bloom, J. S., Akeson, R. L., and Blake, C. H.: 2007b, *ApJ* **669**, 1072

Eisner, J. A., Lane, B. F., Akeson, R. L., Hillenbrand, L. A., and Sargent, A. I.: 2003, *ApJ* **588**, 360

Eisner, J. A., Lane, B. F., Hillenbrand, L. A., Akeson, R. L., and Sargent, A. I.: 2004, *ApJ* **613**, 1049

Evans, II, N. J., Dunham, M. M., Jørgensen, J. K., Enoch, M. L., Merín, B., van Dishoeck, E. F., Alcalá, J. M., Myers, P. C., Stapelfeldt, K. R., Huard, T. L., Allen, L. E., Harvey, P. M., van Kempen, T., Blake, G. A., Koerner, D. W., Mundy, L. G., Padgett, D. L., and Sargent, A. I.: 2009, *ApJS* **181**, 321

Folsom, C. P., Bagnulo, S., Wade, G. A., Alecian, E., Landstreet, J. D., Marsden, S. C., and Waite, I. A.: 2012, *MNRAS* **422**, 2072

Ghez, A. M., McCarthy, D. W., Patience, J. L., and Beck, T. L.: 1997, *ApJ* **481**, 378

Glindemann, A.: 2011, *Principles of Stellar Interferometry*

Glindemann, A., Albertsen, M., Andolfato, L., Avila, G., Ballester, P., Bauvir, B., Delplancke, F., Derie, F., Dimmler, M., Duhoux, P., di Folco, E., Frahm, R., Galliano, E., Gilli, B., Giordano, P. N., Gitton, P. B., Guisard, S., Housen, N., Hummel, C. A., Huxley, A., Karban, R., Kervella, P., Kiekebusch, M., Koehler, B., Leveque, S. A., Licha, T., Longinotti, A., McKay,

D. J., Menardi, S., Monnet, G. J., Morel, S., Paresce, F., Percheron, I., Petr-Gotzens, M., Phan Duc, T., Pott, J.-U., Puech, F., Rantakyro, F. T., Richichi, A., Sabet, C., Scales, K. L., Schoeller, M., Schuhler, N., van den Ancker, M., Vannier, M., Wallander, A., Wittkowski, M., and Wilhelm, R. C.: 2004, in W. A. Traub (ed.), *New Frontiers in Stellar Interferometry*, Vol. 5491 of *Society of Photo-Optical Instrumentation Engineers (SPIE) Conference Series*, p. 447

Goodman, J. W.: 2000, *Statistical Optics*

Graham, J. A.: 1992, *PASP* **104**, 479

Greene, T. P., Wilking, B. A., Andre, P., Young, E. T., and Lada, C. J.: 1994, *ApJ* **434**, 614

Grellmann, R., Ratzka, T., Kraus, S., Linz, H., Preibisch, T., and Weigelt, G.: 2011, *A&A* **532**, A109

Grinin, V. P., Kozlova, O. V., Natta, A., Ilyin, I., Tuominen, I., Rostopchina, A. N., and Shakhovskoy, D. N.: 2001, *A&A* **379**, 482

Grinin, V. P., The, P. S., de Winter, D., Giampapa, M., Rostopchina, A. N., Tambovtseva, L. V., and van den Ancker, M. E.: 1994, *A&A* **292**, 165

Haisch, Jr., K. E., Lada, E. A., and Lada, C. J.: 2001, *ApJ* **553**, L153

Hartmann, L., Calvet, N., Gullbring, E., and D'Alessio, P.: 1998, *ApJ* **495**, 385

Hecht, E. and Zajac, A.: 1974, *Optics*

Henning, T. and Meeus, G.: 2009, *ArXiv e-prints*

Herbig, G. H.: 1960, *ApJS* **4**, 337

Herbig, G. H. and Bell, K. R.: 1988, *Third Catalog of Emission-Line Stars of the Orion Population : 3 : 1988*

Herbst, W. and Shevchenko, V. S.: 1999, *AJ* **118**, 1043

Hillenbrand, L. A., Strom, S. E., Vrba, F. J., and Keene, J.: 1992, *ApJ* **397**, 613

Hueso, R. and Guillot, T.: 2005, *A&A* **442**, 703

Ilee, J. D.: 2013, *Ph.D. thesis*, University of Leeds

Isella, A. and Natta, A.: 2005, *A&A* **438**, 899

Isella, A., Tatulli, E., Natta, A., and Testi, L.: 2008, *A&A* **483**, L13

Jennison, R. C.: 1958, *MNRAS* **118**, 276

Johnstone, C. P., Jardine, M., Gregory, S. G., Donati, J.-F., and Hussain, G.: 2013, *MNRAS*

Joy, A. H.: 1945, *Contributions from the Mount Wilson Observatory / Carnegie Institution of Washington* **709**, 1

Juhász, A., Bouwman, J., Henning, T., Acke, B., van den Ancker, M. E., Meeus, G., Dominik, C., Min, M., Tielens, A. G. G. M., and Waters, L. B. F. M.: 2010, *ApJ* **721**, 431

Juhász, A., Prusti, T., Ábrahám, P., and Dullemond, C. P.: 2007, *MNRAS* **374**, 1242

Kama, M., Min, M., and Dominik, C.: 2009, *A&A* **506**, 1199

Kenyon, S. J. and Hartmann, L.: 1987, *ApJ* **323**, 714

Kharchenko, N. V. and Roeser, S.: 2009, *VizieR Online Data Catalog* **1280**, 0

Kishimoto, M., Hönig, S. F., Antonucci, R., Millour, F., Tristram, K. R. W., and Weigelt, G.: 2011, *A&A* **536**, A78

Koehler, B.: 2001, in *VLTI Tutorial; Garching, Germany*

Koenigl, A.: 1991, *ApJ* **370**, L39

Köhler, R. and Jaffe, W.: 2008, in A. Richichi, F. Delplancke, F. Paresce, and A. Chelli (eds.), *The Power of Optical/IR Interferometry: Recent Scientific Results and 2nd Generation*, p. 569

Kraus, S.: 2007, *Ph.D. thesis*, Max-Planck-Institut für Radioastronomie, Auf dem Hügel 69, Bonn, Germany

Kraus, S., Calvet, N., Hartmann, L., Hofmann, K.-H., Kreplin, A., Monnier, J. D., and Weigelt, G.: 2012, *ApJ* **752**, 11

Kraus, S., Hofmann, K.-H., Benisty, M., Berger, J.-P., Chesneau, O., Isella, A., Malbet, F., Meilland, A., Nardetto, N., Natta, A., Preibisch, T., Schertl, D., Smith, M., Stee, P., Tatulli, E., Testi, L., and Weigelt, G.: 2008a, *A&A* **489**, 1157

Kraus, S., Hofmann, K.-H., Menten, K. M., Schertl, D., Weigelt, G., Wyrowski, F., Meilland, A., Perraut, K., Petrov, R., Robbe-Dubois, S., Schilke, P., and Testi, L.: 2010, *Nature* **466**, 339

Kraus, S., Preibisch, T., and Ohnaka, K.: 2008b, *ApJ* **676**, 490

Kreplin, A., Kraus, S., Hofmann, K.-H., Schertl, D., Weigelt, G., and Driebe, T.: 2012, *A&A* **537**, A103

Kreplin, A., Weigelt, G., Kraus, S., Grinin, V., Hofmann, K.-H., Kishimoto, M., Schertl, D., Tambovtseva, L., Clausse, J.-M., Massi, F., Perraut, K., and Stee, P.: 2013, *A&A* **551**, A21

Lachaume, R., Malbet, F., and Monin, J.-L.: 2003, *A&A* **400**, 185

Lada, C. J.: 1987, in M. Peimbert and J. Jugaku (eds.), *Star Forming Regions*, Vol. 115 of *IAU Symposium*, pp 1–17

Lada, C. J. and Wilking, B. A.: 1984, *ApJ* **287**, 610

Lafrasse, S., Mella, G., Bonneau, D., Duvert, G., Delfosse, X., and Chelli, A.: 2010, *VizieR Online Data Catalog* **2300**, 0

Lagarde, S., Robbe-Dubois, S., Petrov, R. G., Lopez, B., Jaffe, W. J., Venema, L., Berio, P., Antonelli, P., Beckmann, U., Bettonvil, F. C., Graser, U., Navarro, R., and Matter, A.: 2012, in *Society of Photo-Optical Instrumentation Engineers (SPIE) Conference Series*, Vol. 8445 of *Society of Photo-Optical Instrumentation Engineers (SPIE) Conference Series*

Lamers, H. J. G. L. M., Zickgraf, F.-J., de Winter, D., Houziaux, L., and Zorec, J.: 1998, *A&A* **340**, 117

Larson, R. B.: 2010, *Reports on Progress in Physics* **73(1)**, 014901

Le Bouquin, J.-B., Berger, J.-P., Lazareff, B., Zins, G., Haguenauer, P., Jocou, L., Kern, P., Millan-Gabet, R., Traub, W., Absil, O., Augereau, J.-C., Benisty, M., Blind, N., Bonfils, X., Bourget, P., Delboulbe, A., Feautrier, P., Germain, M., Gitton, P., Gillier, D., Kiekebusch, M., Kluska, J., Knudstrup, J., Labeye, P., Lizon, J.-L., Monin, J.-L., Magnard, Y., Malbet, F., Maurel, D., Ménard, F., Micallef, M., Michaud, L., Montagnier, G., Morel, S., Moulin, T., Perraut, K., Popovic, D., Rabou, P., Rochat, S., Rojas, C., Roussel, F., Roux, A., Stadler, E., Stefl, S., Tatulli, E., and Ventura, N.: 2011, *A&A* **535**, A67

Lecavelier des Etangs, A., Nitschelm, C., Olsen, E. H., Vidal-Madjar, A., and Ferlet, R.: 2005, *A&A* **439**, 571

Leinert, C., Graser, U., Przygodda, F., Waters, L. B. F. M., Perrin, G., Jaffe, W., Lopez, B., Bakker, E. J., Böhm, A., Chesneau, O., Cotton, W. D., Damstra, S., de Jong, J., Glazenborg-Kluttig, A. W., Grimm, B., Hanenburg, H., Laun, W., Lenzen, R., Ligori, S., Mathar, R. J., Meisner, J., Morel, S., Morr, W., Neumann, U., Pel, J.-W., Schuller, P., Rohloff, R.-R., Stecklum, B., Storz, C., von der Lühe, O., and Wagner, K.: 2003, *Ap&SS* **286**, 73

Lopez, B., Wolf, S., Lagarde, S., Abraham, P., Antonelli, P., Augereau, J. C., Beckman, U., Behrend, J., Berruyer, N., Bresson, Y., Chesneau, O., Clausse, J. M., Connot, C., Demyk, K., Danchi, W. C., Dugué, M., Flament, S., Glazenborg, A., Graser, U., Henning, T., Hofmann, K. H., Heininger, M., Hugues, Y., Jaffe, W., Jankov, S., Kraus, S., Laun, W., Leinert, C., Linz, H., Mathias, P., Meisenheimer, K., Matter, A., Menut, J. L., Millour, F., Neumann, U., Nussbaum, E., Niedzielski, A., Mosonic, L., Petrov, R., Ratzka, T., Robbe-Dubois, S., Roussel, A., Schertl, D., Schmider, F.-X., Stecklum, B., Thiebaut, E., Vakili, F., Wagner, K., Waters, L. B. F. M., and Weigelt, G.: 2006, in *Society of Photo-Optical Instrumentation Engineers (SPIE) Conference Series*, Vol. 6268 of *Society of Photo-Optical Instrumentation Engineers (SPIE) Conference Series*

Malbet, F., Kern, P., Schanen-Duport, I., Berger, J.-P., Rousselet-Perraut, K., and Benech, P.: 1999, *A&AS* **138**, 135

Malbet, F., Lachaume, R., Berger, J.-P., Colavita, M. M., di Folco, E., Eisner, J. A., Lane, B. F., Millan-Gabet, R., Ségransan, D., and Traub, W. A.: 2005, *A&A* **437**, 627

Malfait, K., Bogaert, E., and Waelkens, C.: 1998, *A&A* **331**, 211

McCabe, C., Ghez, A. M., Prato, L., Duchêne, G., Fisher, R. S., and Telesco, C.: 2006, *ApJ* **636**, 932

McCaughrean, M.: 1997, in D. Soderblom (ed.), *Planets Beyond the Solar System and the Next Generation of Space Missions*, Vol. 119 of *Astronomical Society of the Pacific Conference Series*, p. 53

McCaughrean, M. J., Chen, H., Bally, J., Erickson, E., Thompson, R., Rieke, M., Schneider, G., Stolovy, S., and Young, E.: 1998, *ApJ* **492**, L157

Meeus, G., Waelkens, C., and Malfait, K.: 1998, *A&A* **329**, 131

Meeus, G., Waters, L. B. F. M., Bouwman, J., van den Ancker, M. E., Waelkens, C., and Malfait, K.: 2001, *A&A* **365**, 476

Mendigutía, I., Calvet, N., Montesinos, B., Mora, A., Muzerolle, J., Eiroa, C., Oudmaijer, R. D., and Merín, B.: 2011, *A&A* **535**, A99

Millan-Gabet, R., Malbet, F., Akeson, R., Leinert, C., Monnier, J., and Waters, R.: 2007, *Protostars and Planets V* pp 539–554

Millan-Gabet, R., Schloerb, F. P., and Traub, W. A.: 2001, *ApJ* **546**, 358

Millour, F.: 2008, *New Astron. Rev.* **52**, 177

Miroshnichenko, A. S.: 2007, *ApJ* **667**, 497

Miroshnichenko, A. S., Levato, H., Bjorkman, K. S., and Grosso, M.: 2001, *A&A* **371**, 600

Monnier, J. D.: 2003, *Reports on Progress in Physics* **66**, 789

Monnier, J. D., Berger, J., Millan-Gabet, R., Traub, W. A., Schloerb, F. P., Pedretti, E., Benisty, M., Carleton, N. P., Haguenauer, P., Kern, P., Labeye, P., Lacasse, M. G., Malbet, F., Perraut, K., Pearlman, M., and Zhao, M.: 2006, *ApJ* **647**, 444

Monnier, J. D. and Millan-Gabet, R.: 2002, *ApJ* **579**, 694

Monnier, J. D., Millan-Gabet, R., Billmeier, R., Akeson, R. L., Wallace, D., Berger, J., Calvet, N., D'Alessio, P., Danchi, W. C., Hartmann, L., Hillenbrand, L. A., Kuchner, M., Rajagopal, J., Traub, W. A., Tuthill, P. G., Boden, A., Booth, A., Colavita, M., Gathright, J., Hrynevych, M., Le Mignant, D., Ligon, R., Neyman, C., Swain, M., Thompson, R., Vasisht, G., Wizinowich, P., Beichman, C., Beletic, J., Creech-Eakman, M., Koresko, C., Sargent, A., Shao, M., and van Belle, G.: 2005, *ApJ* **624**, 832

Muzerolle, J., Calvet, N., Hartmann, L., and D'Alessio, P.: 2003, *ApJ* **597**, L149

Muzerolle, J., D'Alessio, P., Calvet, N., and Hartmann, L.: 2004, *ApJ* **617**, 406

Muzerolle, J., Hartmann, L., and Calvet, N.: 1998, *AJ* **116**, 2965

Natta, A., Grinin, V. P., Mannings, V., and Ungerechts, H.: 1997, *ApJ* **491**, 885

Natta, A., Prusti, T., Neri, R., Wooden, D., Grinin, V. P., and Mannings, V.: 2001, *A&A* **371**, 186

Natta, A. and Whitney, B. A.: 2000, *A&A* **364**, 633

Neuhäuser, R. and Forbrich, J.: 2008, *The Corona Australis Star Forming Region*, pp 735–+

O'Dell, C. R. and Wen, Z.: 1994, *ApJ* **436**, 194

Ortiz, J. L., Sugerman, B. E. K., de La Cueva, I., Santos-Sanz, P., Duffard, R., Gil-Hutton, R., Melita, M., and Morales, N.: 2010, *A&A* **519**, A7+

Padgett, D. L., Brandner, W., Stapelfeldt, K. R., Strom, S. E., Terebey, S., and Koerner, D.: 1999, *AJ* **117**, 1490

Pasinetti Fracassini, L. E., Pastori, L., Covino, S., and Pozzi, A.: 2001, *A&A* **367**, 521

Patten, B. M.: 1998, in R. A. Donahue and J. A. Bookbinder (eds.), *Cool Stars, Stellar Systems, and the Sun*, Vol. 154 of *Astronomical Society of the Pacific Conference Series*, pp 1755–+

Pearson, K.: 1900, *Philosophical Magazine Series 5* **50(302)**, 157

Petrov, R. G., Malbet, F., Weigelt, G., Antonelli, P., Beckmann, U., Bresson, Y., Chelli, A., Dugué, M., Duvert, G., Gennari, S., Glück, L., Kern, P., Lagarde, S., Le Coarer, E., Lisi, F., Millour, F., Perraut, K., Puget, P., Rantakyrö, F., Robbe-Dubois, S., Roussel, A., Salinari, P., Tatulli, E., Zins, G., Accardo, M., Acke, B., Agabi, K., Altariba, E., Arezki, B., Aristidi, E., Baffa, C., Behrend, J., Blöcker, T., Bonhomme, S., Busoni, S., Cassaing, F., Clausse, J.-M., Colin, J., Connot, C., Delboulbé, A., Domiciano de Souza, A., Driebe, T., Feautrier, P., Ferruzzi, D., Forveille, T., Fossat, E., Foy, R., Fraix-Burnet, D., Gallardo, A., Giani, E., Gil, C., Glentzlin, A., Heiden, M., Heininger, M., Hernandez Utrera, O., Hofmann, K.-H., Kamm, D., Kiekebusch, M., Kraus, S., Le Contel, D., Le Contel, J.-M., Lesourd, T., Lopez, B., Lopez, M., Magnard, Y., Marconi, A., Mars, G., Martinot-Lagarde, G., Mathias, P., Mège, P., Monin, J.-L., Mouillet, D., Mourard, D., Nussbaum, E., Ohnaka, K., Pacheco, J., Perrier, C., Rabbia, Y., Rebattu, S., Reynaud, F., Richichi, A., Robini, A., Sacchettini, M., Schertl, D., Schöller, M., Solscheid, W., Spang, A., Stee, P., Stefanini, P., Tallon, M., Tallon-Bosc, I., Tasso, D., Testi, L., Vakili, F., von der Lühe, O., Valtier, J.-C., Vannier, M., and Ventura, N.: 2007, *A&A* **464**, 1

Petrov, R. G., Millour, F., Lagarde, S., Vannier, M., Rakshit, S., Marconi, A., and weigelt, G.: 2012, in *Society of Photo-Optical Instrumentation Engineers (SPIE) Conference Series*, Vol. 8445 of *Society of Photo-Optical Instrumentation Engineers (SPIE) Conference Series*

Pinte, C., Ménard, F., Berger, J. P., Benisty, M., and Malbet, F.: 2008, *ApJ* **673**, L63

Pontoppidan, K. M., Dullemond, C. P., Blake, G. A., Boogert, A. C. A., van Dishoeck, E. F., Evans, II, N. J., Kessler-Silacci, J., and Lahuis, F.: 2007, *ApJ* **656**, 980

Prato, L., Greene, T. P., and Simon, M.: 2003, *ApJ* **584**, 853

Preibisch, T., Ratzka, T., Gehring, T., Ohlendorf, H., Zinnecker, H., King, R. R., McCaughrean, M. J., and Lewis, J. R.: 2011, *A&A* **530**, A40

Reipurth, B. and Graham, J. A.: 1988, *A&A* **202**, 219

Reipurth, B. and Zinnecker, H.: 1993, *A&A* **278**, 81

Richichi, A., Percheron, I., and Khristoforova, M.: 2005, *A&A* **431**, 773

Schegerer, A. A., Ratzka, T., Schuller, P. A., Wolf, S., Mosoni, L., and Leinert, C.: 2013, *A&A* **555**, A103

Schegerer, A. A., Wolf, S., Hummel, C. A., Quanz, S. P., and Richichi, A.: 2009, *A&A* **502**, 367

Schegerer, A. A., Wolf, S., Ratzka, T., and Leinert, C.: 2008, *A&A* **478**, 779

Sitko, M. L., Carpenter, W. J., Kimes, R. L., Wilde, J. L., Lynch, D. K., Russell, R. W., Rudy, R. J., Mazuk, S. M., Venturini, C. C., Puetter, R. C., Grady, C. A., Polomski, E. F., Wisnewski, J. P., Brafford, S. M., Hammel, H. B., and Perry, R. B.: 2008, *ApJ* **678**, 1070

Stępień, K.: 2000, *A&A* **353**, 227

Tannirkulam, A., Harries, T. J., and Monnier, J. D.: 2007, *ApJ* **661**, 374

Tannirkulam, A., Monnier, J. D., Harries, T. J., Millan-Gabet, R., Zhu, Z., Pedretti, E., Ireland, M., Tuthill, P., ten Brummelaar, T., McAlister, H., Farrington, C., Goldfinger, P. J., Sturmann, J., Sturmann, L., and Turner, N.: 2008, *ApJ* **689**, 513

Tatulli, E., Millour, F., Chelli, A., Duvert, G., Acke, B., Hernandez Utrera, O., Hofmann, K., Kraus, S., Malbet, F., Mège, P., Petrov, R. G., Vannier, M., Zins, G., Antonelli, P., Beckmann, U., Bresson, Y., Dugué, M., Gennari, S., Glück, L., Kern, P., Lagarde, S., Le Coarer, E., Lisi, F., Perraut, K., Puget, P., Rantakyrö, F., Robbe-Dubois, S., Roussel, A., Weigelt, G., Accardo, M., Agabi, K., Altariba, E., Arezki, B., Aristidi, E., Baffa, C., Behrend, J., Blöcker, T., Bonhomme, S., Busoni, S., Cassaing, F., Clausse, J., Colin, J., Connot, C., Delboulbé, A., Domiciano de Souza, A., Driebe, T., Feautrier, P., Ferruzzi, D., Forveille, T., Fossat, E., Foy, R., Fraix-Burnet, D., Gallardo, A., Giani, E., Gil, C., Glentzlin, A., Heiden, M., Heininger, M., Kamm, D., Kiekebusch, M., Le Contel, D., Le Contel, J., Lesourd, T., Lopez, B., Lopez, M., Magnard, Y., Marconi, A., Mars, G., Martinot-Lagarde, G., Mathias, P., Monin, J., Mouillet, D., Mourard, D., Nussbaum, E., Ohnaka, K., Pacheco, J., Perrier, C., Rabbia, Y., Rebattu, S., Reynaud, F., Richichi, A., Robini, A., Sacchettini, M., Schertl, D., Schöller, M., Solscheid, W., Spang, A., Stee, P., Stefanini, P., Tallon, M., Tallon-Bosc, I., Tasso, D., Testi, L., Vakili, F., von der Lühe, O., Valtier, J., and Ventura, N.: 2007, *A&A* **464**, 29

Tristram, K. R. W.: 2007, *Ph.D. thesis*, Max-Planck-Institut für Astronomie, Königstuhl 17, 69117 Heidelberg, Germany

Tuthill, P. G., Monnier, J. D., and Danchi, W. C.: 2001, *Nature* **409**, 1012

van Boekel, R., Dullemond, C. P., and Dominik, C.: 2005a, *A&A* **441**, 563

van Boekel, R., Min, M., Waters, L. B. F. M., de Koter, A., Dominik, C., van den Ancker, M. E., and Bouwman, J.: 2005b, *A&A* **437**, 189

van Cittert, P. H.: 1934, *Physica* **1**, 201

Verhoeff, A. P., Waters, L. B. F. M., van den Ancker, M. E., Min, M., Stap, F. A., Pantin, E., van Boekel, R., Acke, B., Tielens, A. G. G. M., and de Koter, A.: 2012, *A&A* **538**, A101

Vicente, S. M. and Alves, J.: 2005, *A&A* **441**, 195

Vinković, D.: 2006, *ApJ* **651**, 906

Vinković, D. and Jurkić, T.: 2007, *ApJ* **658**, 462

Vural, J., Kraus, S., Kreplin, A., Weigelt, G., Fossat, E., Massi, F., Perraut, K., and Vakili, F.: 2014a, *A&A* **569**, A25

Vural, J., Kreplin, A., Kishimoto, M., Weigelt, G., Hofmann, K.-H., Kraus, S., Schertl, D., Dugué, M., Duvert, G., Lagarde, S., and Massi, F.: 2014b, *A&A* **564**, A118

Vural, J., Kreplin, A., Kraus, S., Weigelt, G., Driebe, T., Benisty, M., Dugué, M., Massi, F., Monin, J.-L., and Vannier, M.: 2012, *A&A* **543**, A162

Walter, F. M. and Miner, J.: 2005, in F. Favata, G. A. J. Hussain, & B. Battrick (ed.), *13th Cambridge Workshop on Cool Stars, Stellar Systems and the Sun*, Vol. 560 of *ESA Special Publication*, pp 1021–+

Wang, H., Mundt, R., Henning, T., and Apai, D.: 2004, *ApJ* **617**, 1191

Wang, Y., Weigelt, G., Kreplin, A., Hofmann, K.-H., Kraus, S., Miroshnichenko, A. S., Schertl, D., Chelli, A., Domiciano de Souza, A., Massi, F., and Robbe-Dubois, S.: 2012, *A&A* **545**, L10

Weigelt, G., Grinin, V. P., Groh, J. H., Hofmann, K.-H., Kraus, S., Miroshnichenko, A. S., Schertl, D., Tambovtseva, L. V., Benisty, M., Driebe, T., Lagarde, S., Malbet, F., Meilland, A., Petrov, R., and Tatulli, E.: 2011, *A&A* **527**, A103

Weise, P., Launhardt, R., Setiawan, J., and Henning, T.: 2010, *A&A* **517**, A88

Wheelwright, H. E., Weigelt, G., Caratti o Garatti, A., and Garcia Lopez, R.: 2013, *A&A* **558**, A116

Williams, J. P. and Cieza, L. A.: 2011, *ARA&A* **49**, 67

Wolf, S., Henning, T., and Stecklum, B.: 1999, *A&A* **349**, 839

Wyatt, M. C.: 2008, *ARA&A* **46**, 339

Zernike, F.: 1938, *Physica* **5**, 785

Zwintz, K., Kallinger, T., Guenther, D. B., Gruberbauer, M., Huber, D., Rowe, J., Kuschnig, R., Weiss, W. W., Matthews, J. M., Moffat, A. F. J., Rucinski, S. M., Sasselov, D., Walker, G. A. H., and Casey, M. P.: 2009, *A&A* **494**, 1031

Acknowledgements

I would like to thank my doctoral advisor Prof. Dr. Gerd Weigelt for the opportunity to work in this field and for providing me with the necessary financial support. I thank Prof. Dr. Pavel Kroupa, Prof. Dr. Ian Brock, and Prof. Dr. Clemens Simmer, who agreed to be members of my examination committee. A special thank you goes to my colleague and office mate Alexander Kreplin with whom I had many productive discussions and who shared a lot of his PhD experience with me. I thank Stefan Kraus who provided me with interferometric data – without that, this thesis would not have been possible. Thank you to Thomas Driebe for introducing me into the field of interferometry and data modeling, and also for sharing many entertaining anecdotes. In addition, many thanks go to Rebekka Grellmann, Alexander Kreplin, Jean-Luc Menut and Dominik Rösner for proofreading this thesis. Thanks to all my colleagues, especially those who enriched my time at the institute and in Bonn in general with stimulating and controverse discussions and diverting board & card games. Finally, I thank my friends and family for the occasional distraction and the support!